THE UNIVERSITY OF CHICAGO

SEARCH FOR THE TOP QUARK DECAYING TO A CHARGED HIGGS BOSON IN $\bar{p}p$ COLLISIONS AT $\sqrt{s} = 1.8$ TEV

A DISSERTATION SUBMITTED TO
THE FACULTY OF THE DIVISION OF THE PHYSICAL SCIENCES
IN CANDIDACY FOR THE DEGREE OF
DOCTOR OF PHILOSOPHY

DEPARTMENT OF PHYSICS

BY
JINSONG WANG

CHICAGO, ILLINOIS
DECEMBER 1994

ACKNOWLEDGEMENTS

The success of the CDF experiment is only possible through the efforts of many people and I wish to thank all the members of the collaboration and Fermilab staff for their vital contributions.

I thank my thesis advisor, Mel Shochet. In the spring of 1990, his course "Introductions to Particle Physics" attracted me so much that I started working on the CDF experiment in that summer. During the past four years, he tried as much as possible to help me to grow and develop although he has a busy schedule serving as the co-spokesperson of the CDF collaboration.

Special thanks are due to Henry Frisch for his advice and encouragement over the past few years. Together with Mel, Henry has provided the group with outstanding scientific and educational environment. I learned from him much about how to identify the most interesting points in an analysis, how to start and finish a project, and how to work as a team player in the collaboration.

I am especially grateful to my friend and colleague Milciades Contreras for his participation in all the projects I worked on and for a great time working together. I thank him for advice and instructions while I was working on luminosity monitors, making datasets, monitoring the data, and trying to find the top in any ways.

I thank Carla Grosso-Pilcher for her help on PAW, without which this thesis will take longer to finish. Her kindness and support made the years at HEP even more enjoyable.

I thank Claudio Campagnari for helping me with my first FORTRAN code. I thank Sarah Eno for teaching me the debugger on VAX and her instruction and patience while I was learning my way around the level 1 trigger. I thank Jim Romano for sharing the pager and for time we spent with Sarah on debugging the level 1 trigger system. I thank Kevin Burkett, for making a nice and sophisticated interface LUMMON_DISPLAY for LUMMON and taking care of the LUMMON package for run 1b. I thank Sacha Kopp for supplying the electron trigger efficiency and the "good-run" list. I thank Xin Wu for stripping the datasets and his contribution in this analysis. I further thank Dave Gerdes, Marshall Miller, Aaron Roodman, David Saltzberg, Greg Sullivan, Peter Wilson for their help and friendship. I thank Steve Hahn, Jim Hylen and Jim Patrick for training me as an "Ace". I thank Marty Dippel for making it possible to do analyses on the UCCDF cluster. I thank Marypat Sharer, who helped me to fight with the problematic T2.

To the many friends who have helped to make my time in Chicago a most enjoyable one, more personal thanks are due. Thanks to my fellow graduate students Xiaoyan Chang, Wenshuo Li, Xiaochun Luo and Yuyao Zha, who shared my experience of the first and most difficult year in the states and for their long term friendship. Thanks to the members of the Blood and GUT's volleyball team — especially Jim and Colin who encouraged me to go back to the court, where we had so much fun. Thanks to my officemate Scott Oser, whose refrigerator saved me from starving during the thesis writing. Special thanks to Shude Mao, my best friend since college, whose enthusiasm

to physics has impressed me most although I still do not understand his dark matter theory.

I wish to thank the University of Chicago for the contingent support and I thank Leon Lederman for his financial support and encouragement when I was not sure whether I would work on particle physics in the summer of 1990.

Finally, I would like to thank my parents and sister for their unfailing love and support. And I dedicate this thesis to my wife, Kun Fang, whose love helped to make everything possible.

TABLE OF CONTENTS

LIST OF TABLES

LIST OF ILLUSTRATIONS

ABSTRACT

This paper presents the results of a search in $\bar{p}p$ collisions at $\sqrt{s}$ = 1.8 TeV for the top quark decaying to a charged Higgs boson ($H^{\pm}$). We search for dilepton final states from the decay chain $t\bar{t} \rightarrow HH$ (or HW, or WW) + $b\bar{b} \rightarrow ll$ + X. In a sample of 19.3 pb^{-1} collected during 1992-93 with the Collider Detector at Fermilab (CDF), we observe 2 events with a background estimation of 3.0±1.0 events. Limits at 95% C.L. in the (M_t, M_H) plane are presented. We also interpret the results in terms of the parameter tanβ of two-Higgs-doublet models.

Chapter 1

INTRODUCTION

1.1 The Standard Model and the Top Quark

In the Standard Model [1] the constituents of all matter are arranged in three generations of quarks and leptons (see Table 1.1). The top quark (t quark) is predicted as the SU(2)-doublet partner of the bottom (or b) quark. Evidence for the need of the top quark is found in various measurements of b-quark production and decay: (i) the absence of flavor-changing neutral currents in b-quark decay rules out most models without a top quark [2]; (ii) a measurement of the forward-backward charge asymmetry for the process $e^+e^- \rightarrow b\bar{b}$ has verified the Standard Model weak isodoublet couplings for the b quark, implying the existence of an isospin partner, the top quark [3]; and (iii) the level of mixing measured in the B_d^0 system is inconsistent with the b quark being an SU(2) singlet [4].

Within the context of the Standard Model, the top quark decays almost exclusively into a W boson and a b quark. The CDF collaboration has searched for the top quark with this assumption and recently presented

	Quarks				Leptons		
	Name	Charge	Mass [MeV/c^2]	Name	Charge	Mass [MeV/c^2]
1st Generation	u up	$+\frac{2}{3}$	350	e electron	-1	0.511
	d down	$-\frac{1}{3}$	350	ν_e e-neutrino	0	$< 5 \times 10^{-5}$
2nd Generation	c charm	$+\frac{2}{3}$	1800	μ muon	-1	105.7
	s strange	$-\frac{1}{3}$	550	ν_μ μ-neutrino	0	< 0.50
3rd Generation	t top ?	$+\frac{2}{3}$	?	τ tau	-1	1784
	b bottom	$-\frac{1}{3}$	4500	ν_τ τ-neutrino ?	0	< 164

Table 1.1: The three generations of quarks and leptons. The top quark and the tau-neutrino have not definitively been observed. Quark masses are indicative only. Other masses were taken from reference [39].

evidence for an excess of events for which the most natural interpretation is production of top quark pairs with a top mass of 174±16 GeV/c^2 [5]. Although the probability that the observed yield is consistent with the background is estimated to be 0.26%, the statistics are too limited to firmly establish the existence of the top quark. Other searches have placed a 95% confidence level lower limit on the top mass of 131 GeV/c^2 [6], also assuming $t \rightarrow Wb$ only. Without this assumption, the experimental lower limit on the top mass is 62 GeV/c^2 from the W lifetime measurement [7]. Therefore the existence of a light top quark (with a mass lower than W mass) is still possible.

1.2 Extensions to the Standard Model and the Charged Higgs Boson

One of the most fundamental unsolved problems in physics is how the electroweak symmetry is broken and why the symmetry breaking scale is so tiny. The latter question is a modern version of the "large numbers problem" of Dirac, who wondered why the proton mass was so much less than the Planck mass. One of the most attractive frameworks for addressing this question is supersymmetry. The standard model has a fascinating supersymmetric extension which has remained viable over the years while other alternatives such as composite models have encountered difficulties [8]. The supersymmetric standard model resolves the large number problem and is also compatible with our limited experimental constraints on physics at TeV energy scale.

The minimal formulation of the Standard Model of the electroweak interactions [1] uses a single complex Higgs doublet to provide masses for both the gauge bosons and the fermions [9]. In this formulation there is a

single massive scalar, H^0, whose mass is not specified by the theory and which has been excluded in the region $0 < m_{H^0} < 62.4$ GeV/c^2 [10]. However, there is no reason to believe that the Higgs sector has the simplest possible structure. Non-minimal Higgs sectors may play important roles in different phenomena. In supersymmetry, models with two or more doublets are the simplest extensions of the one doublet Standard Model scenario, although more complicated Higgs structures like Higgs triplets are also possible.

A general two-Higgs-doublet model, which is just the Standard Model with an additional Higgs doublet, is particularly attractive since it adds new phenomena (e.g. physical charged Higgs bosons) with the fewest new arbitrary parameters, it automatically satisfies the tree-level relation $\rho = M_W{}^2/(M_Z{}^2\cos^2\theta_W) = 1$, and it allows the absence of tree-level flavor-changing neutral currents (FCNC) if the Higgs-fermion couplings are appropriately chosen. In a two-Higgs-doublet Model, two SU(2) Higgs doublets $\mathbf{\Phi_1} = (\phi_1^{0*}, -\phi_1^-)$ and $\mathbf{\Phi_2} = (\phi_2^+, -\phi_2^0)$ of complex fields provide masses to the charged fermions. Here $\mathbf{\Phi_1}$ designates the doublet which gives mass to the quarks with third component of the weak isospin T_3 = -1/2, the down-type quarks, while the $\mathbf{\Phi_2}$ doublet gives mass to the quarks with $T_3 = 1/2$, the up-type quarks. It is conventional to assume that the charged leptons follow the down quark coupling pattern. The neutral members of the two doublets, ϕ_1^0 and ϕ_2^0, acquire vacuum expectation values, v_1 and v_2, respectively. The values of v_1 and v_2 are not individually predicted, but they are constrained by $(v_1{}^2 + v_2{}^2)^{1/2} = v = 2M_W/g$, where g is the coupling of the electroweak interactions and v is the vacuum expectation value of the Standard Model neutral Higgs doublet.

There are five physical Higgs bosons in a two-Higgs-doublet model: a charged pair ($H^\pm$), two neutral CP-even scalars and a neutral CP-odd pseudoscalar. The masses of the Higgs bosons, as well as the ratio of the

vacuum expectation values, $\tan\beta = v_2/v_1$, are all free parameters of the model. The experimental lower limit on the charged Higgs mass is 45 GeV/c^2 from the direct searches in $Z \rightarrow H^+H^-$ decay at LEP [11].

The Higgs bosons are expected to decay preferentially to the heaviest kinematically allowed fermion pairs since the Yukawa couplings of the Higgs bosons to the fermions are proportional to the fermion masses. In particular, the physical charged Higgs boson fields are linear combinations of the charged components of the two doublets, in the form of $H^{\pm} = \pm v^{-1}(v_1\phi_2^{\pm} - v_2\phi_1^{\pm})$. The Yukawa coupling of the charged Higgs to the down-type quarks and leptons is proportional to $m_f\tan\beta$(m_f is the fermion mass), while the coupling to the up-type quarks is proportional to $m_f\cot\beta$. If the charged Higgs is lighter than the top quark, the predominant decay is $H\rightarrow\tau\nu$ or $H\rightarrow c\bar{s}$. The branching ratio $BR(H\rightarrow\tau\nu)$ is a function of $\tan\beta$ [13]; for $\tan\beta > 1$ the τ decay mode dominates (see Figure 1.1).

1.3 Signatures for the Top Quark Decays in a Charged Higgs Scenario

The existence of charged Higgs bosons, predicted by supersymmetry [14] and other models, provides one way of generating non-standard top decays. In a charged Higgs scenario, the top quark not only can decay into a W boson and a b quark, it can also decay into a charged Higgs boson and a b quark (see Figure 1.2).

In this work, we consider the case that the charged Higgs boson is lighter than $M_t - M_b$, so the t-quark can undergo a two-body decay $t\rightarrow Hb$. If $M_t < m_W + m_b$, $t\rightarrow Hb$ is dominant over $t\rightarrow Wb$ since the H^+ is real and

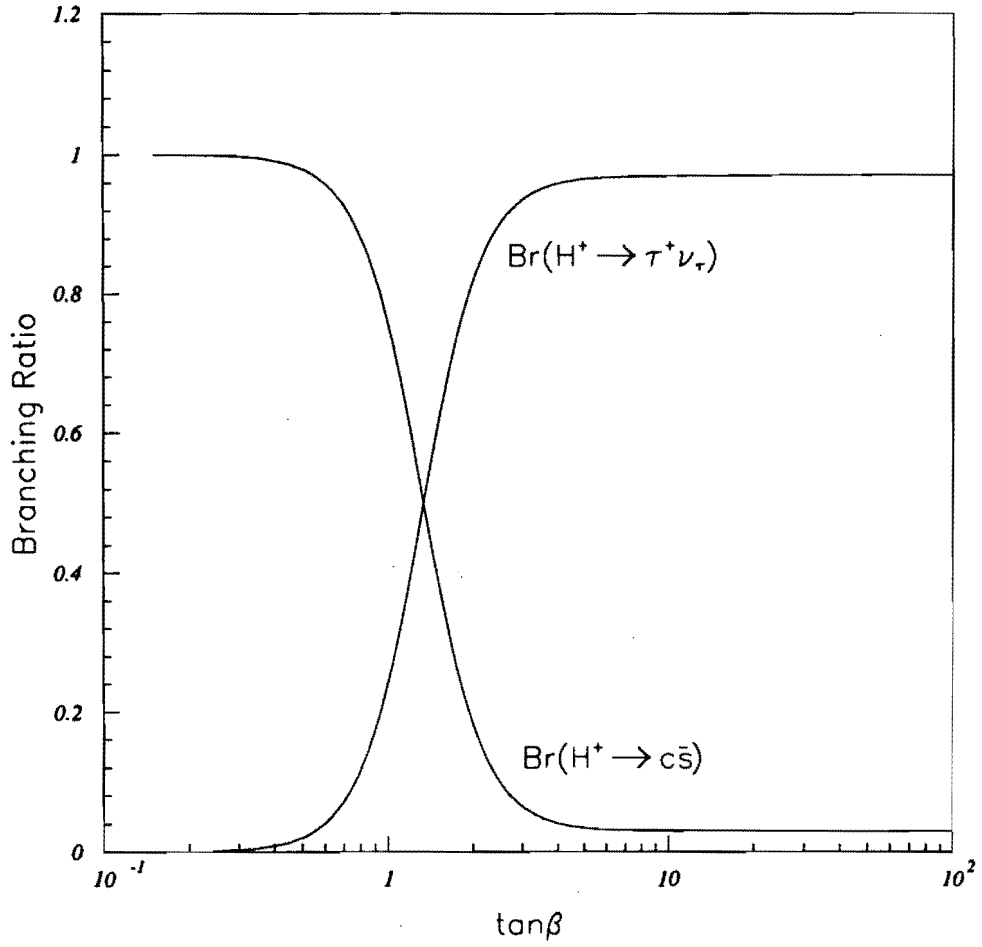

Figure 1.1: Branching ratio of $H \rightarrow \tau\nu$ and $H \rightarrow c\bar{s}$ as a function of $\tan\beta$

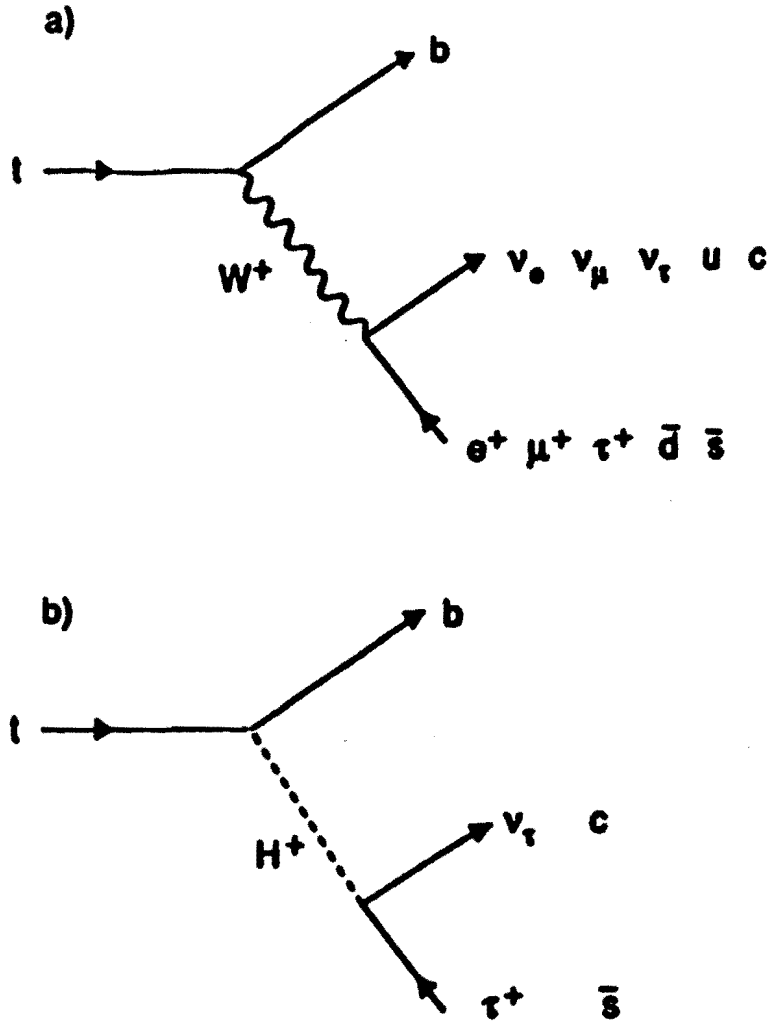

Figure 1.2: The decay of the top quark: (a) into a W and a b quark; (b) into a charged Higgs and a b quark.

W^+ is virtual. If $M_t > m_W + m_b$, the on-shell decays $t \rightarrow Wb$ and $t \rightarrow Hb$ are both allowed. The branching ratio of $t \rightarrow Hb$ in general is a function of the top quark mass, Higgs mass and $\tan\beta$. Figure 1.3 shows the branching ratios $BR(t \rightarrow Hb)$ and $BR(t \rightarrow Wb)$ as a function of $\tan\beta$, for two possible M_t and M_H combinations. At the Tevatron, where top quarks are generated in pairs, we would then have three possible types of top decay modes: 1) $t\bar{t} \rightarrow HbHb$, 2) $t\bar{t} \rightarrow HbWb$ and 3) $t\bar{t} \rightarrow WbWb$.

The requirement of dilepton final states ($e\mu$, ee, $\mu\mu$) provides a clean $t\bar{t}$ signature with small background. Most of the electrons and muons come from $H \rightarrow \tau\nu \rightarrow l\nu\nu\nu$ or $W \rightarrow l\nu$, but leptons from b decay also contribute. The major physics background for the dilepton channel comes from $b\bar{b}$ production with the b quarks decaying into leptons, $Z \rightarrow \tau\tau \rightarrow ll\nu\nu\nu\nu$, Drell-Yan continuum ($q\bar{q} \rightarrow l^+l^-$), W pair production, and W + jet with the W decaying into $l\nu$ and the jet misidentified as a lepton. These backgrounds have distinct topologies and are discussed in detail in Chapter 4.

1.4 Outline of the Thesis

In the period from August 1992 to June 1993, CDF collected approximately 20 pb^{-1} of data produced at the Tevatron proton-antiproton collider at a center of mass energy of 1.8 TeV. The data used in this analysis correspond to 19.3 pb^{-1}. With this data sample, we have conducted a search for the decay $t \rightarrow Hb$, assuming that this and $t \rightarrow Wb$ are allowed decays. We thus search for the two lepton final states from the decay chain $t\bar{t} \rightarrow HH$ (or HW, or WW) + $b\bar{b} \rightarrow ll$ + X.

The thesis will proceed as follows: Chapter 2 describes the Tevatron and the CDF detector. Chapter 3 describes the selection of the data sample.

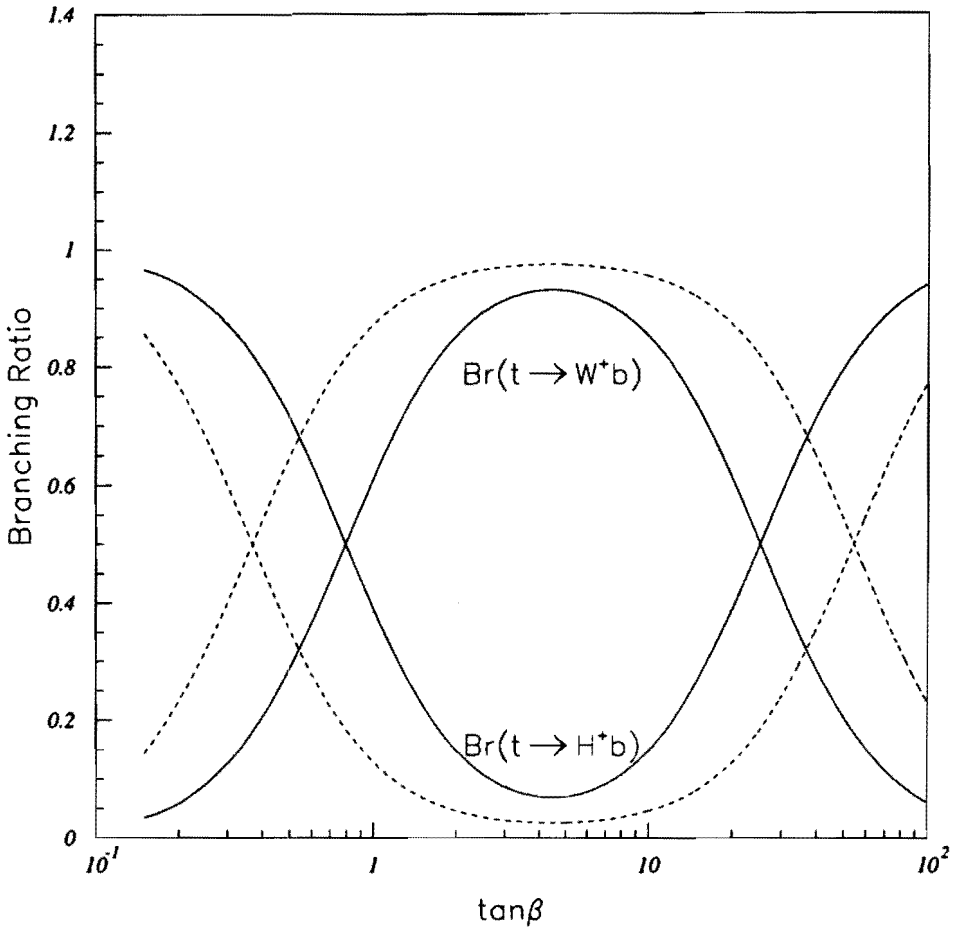

Figure 1.3: $BR(t \to Hb)$ and $BR(t \to Wb)$ as a function of $\tan\beta$, for two possible M_t and M_H combinations. The solid line is for $M_t = 100$ GeV and $M_H = 70$ GeV; the dashed line is for $M_t = 100$ GeV and $M_H = 95$ GeV.

In Chapter 4, the strategy for this search is explained and the top quark signal region is defined and motivated as a result of a comparison of the signal Monte Carlo and a background study. The observed candidate events and the calculated detection efficiency are used in Chapter 5 to derive a 95% C.L. upper limit on the $t\bar{t}$ production cross section as a function of M_t and M_H. Theoretical predictions are then used to convert this cross section limit into a 95% C.L. lower limit on the top and Higgs masses. Chapter 6 contains the summary and conclusion of the analysis. The possibilities for a $t \rightarrow Hb$ search at present and future colliders are discussed.

Chapter 2

The Experiment

2.1 The Tevatron

The Tevatron is a two-kilometer diameter proton-antiproton accelerator, located in the Fermi National Accelerator Laboratory in Batavia, Illinois. It provides the world's highest-energy proton-antiproton collisions. In the 1992-93 collider run, the Tevatron operated with a center-of-mass collision energy of 1800 GeV. An integrated luminosity of 30 pb^{-1} was delivered over the 10-month collider run. The CDF detector recorded about 20 pb^{-1} of data to tape.

The Fermilab accelerator complex is shown in Figure 2.1. Protons are stripped from a hydrogen source in a Cockroft-Walton preaccelerator, and are accelerated to 200 MeV in the Linac. Then they are transferred to the Booster ring and accelerated to 8 GeV. The 8 GeV protons are then injected into the Main Ring and further accelerated. The Main Ring serves for injecting 150 GeV protons and antiprotons into the Tevatron for further acceleration.

The antiprotons are made from the 120 GeV protons in the reaction

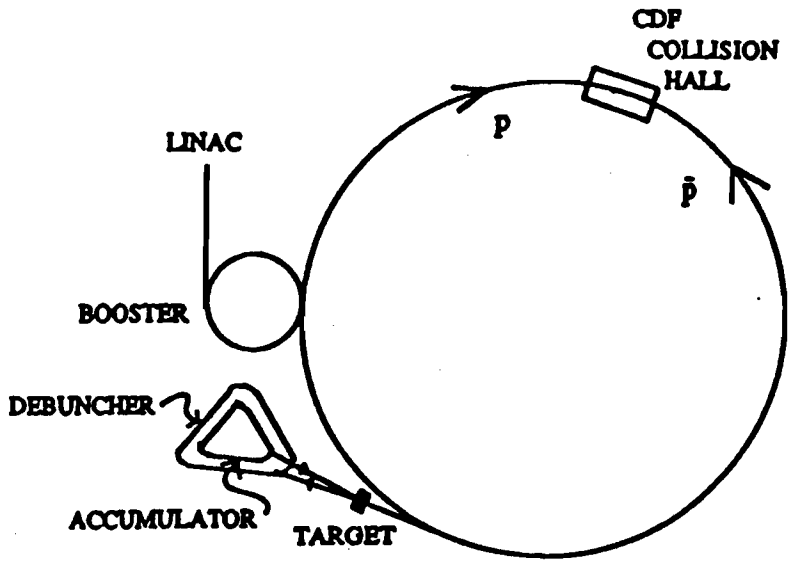

Figure 2.1: The Fermilab accelerator complex.

$pN \rightarrow \bar{p} + X$. The protons, accelerated to 120 GeV in the Main Ring, are extracted and strike a tungsten target to produce antiprotons. Antiprotons with momentum near 8 GeV are selected magnetically and collimated through a lithium lens to enter the Debuncher ring. The Debuncher ring performs a longitudinal phase-space rotation similar to that performed in the transverse direction by the Tevatron's low-beta quadrupoles. The effect is to reduce the beam's momentum spread from 3.5% to 0.2%. The antiproton beam is next transferred to the Antiproton Accumulator, where over a period of up to 24 hours it is stored and "cooled" in all three momentum-space directions so that the stack of antiprotons can eventually be injected into the Main Ring.

When the antiproton stack is sufficiently large (a typical size of 4 $\times 10^{11}$), the process of injection into the Tevatron collider begins. The Tevatron is a superconducting magnet ring located beneath the Main Ring in the same

tunnel. Six bunches of protons are injected at an energy of 150 GeV from the Main Ring to the Tevatron. Antiprotons are transferred from the Accumulator to the Main Ring and accelerated to 150 GeV. Then they are injected (with approximately 60–70% efficiency) into the Tevatron in 6 bunches. With 12 bunches in the Tevatron (6 proton and 6 antiproton), a process of adjusting the interaction points (cogging) takes place so that the crossings are centered in B0 and D0, the places along the ring where the CDF detector and D0 detector are located. Then, the Tevatron is ramped to the full energy, and when the store at 900 GeV becomes stable, a system of quadrupole magnets (the low-beta quads) is energized to focus or squeeze the beams to achieve maximum luminosity. Finally, the beams are scraped to reduce the number of outlying particles that form a "halo" around the center of the beam. At this point, data collection can begin.

2.2 The CDF Detector

The CDF detector was built in the early- and mid-1980's to study a wide range of physics in $\overline{p}p$ collisions. Perspective and cutaway views of the CDF detector are shown in figures 2.2 and 2.3. The approximate dimensions of the detector are 26 m (length) $\times$ 9 m (height) $\times$ 8 m (width) and the detector weighs $\sim$ 5000 tons. The detector's coordinate system has the positive Z axis pointing along the proton direction (east). Cylindrical coordinates (R, θ, ϕ), have R being the perpendicular distance to the beamline, ϕ the azimuthal angle, and θ the polar angle with respect to the Z axis. The pseudorapidity, defined as $\eta = -\ln(\tan(\theta/2))$, is often used instead of the polar angle θ.

The detector has been described in a series of detailed papers [15]. In this section we discuss the components most relevant to this analysis, namely

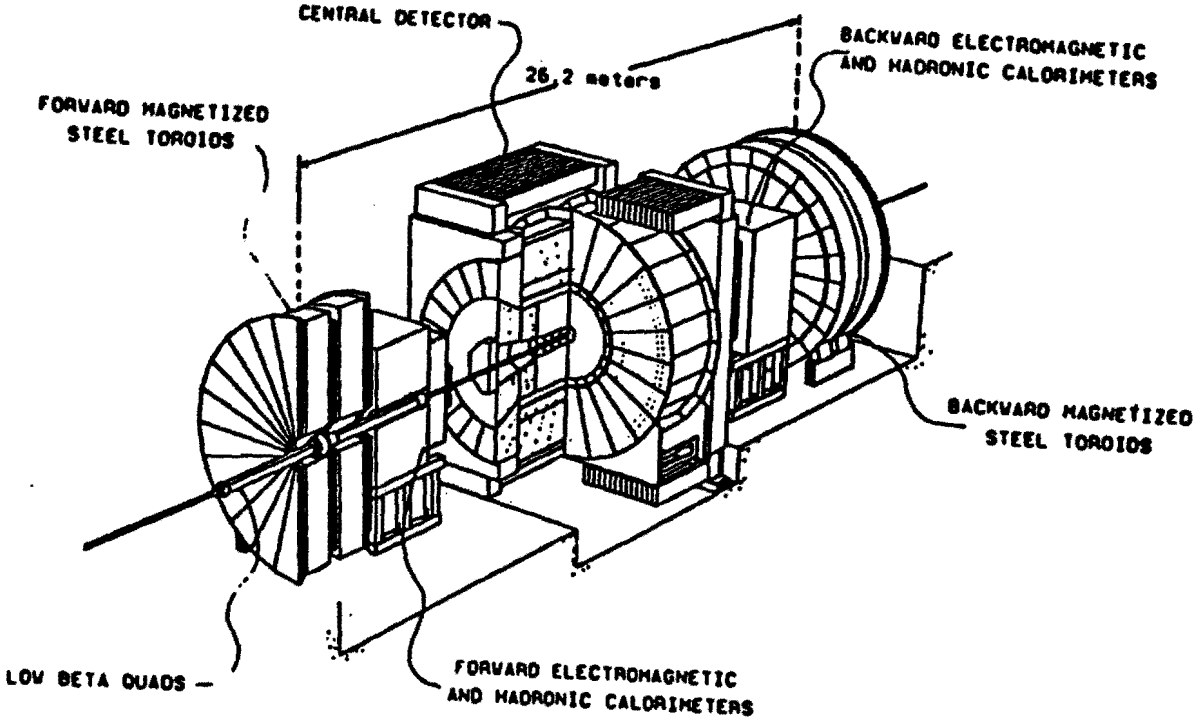

Figure 2.2: Perspective view of the CDF detector.

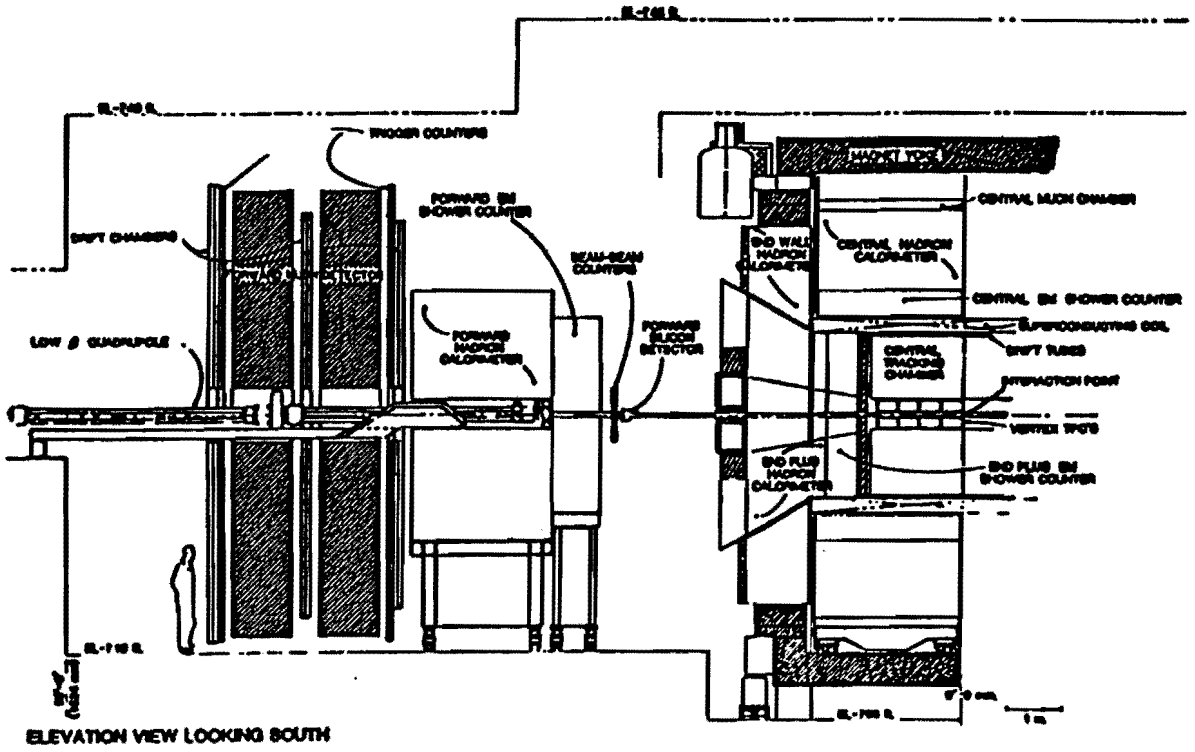

Figure 2.3: Cutaway view of one half of the CDF detector.

the tracking chambers, the calorimeters, the central muon system, and the luminosity monitors.

2.2.1 Tracking Chambers

The momentum of a charged particle is measured from the curvature, azimuthal angle, and polar angle of the track left in the tracking chambers. The CDF detector has three complementary tracking chambers. The inner tracking chamber is the Silicon Vertex Detector (SVX) [16], which is a four-layer silicon microvertex detector with single-sided readout to provide precise $r-\phi$ information for the reconstruction of the track impact parameter. Outside the SVX, the Vertex Tracking Chamber (VTX) [17] provides the necessary tracking information to locate the Z coordinate of the event vertex within 1 mm. (The interaction vertex at the Tevatron has a Gaussian distribution in Z with a sigma of about 30 cm.) The VTX covers the region $|\eta| < 3.25$ (or $8° < \theta < 172°$).

Outside the VTX, the Central Tracking Chamber (CTC) [18] provides precise momentum measurement of charged particles to be used both at the trigger level and in the off-line analysis. The CTC is a 3.2 m long cylindrical drift chamber, with inner radius of 0.28 m and outer radius of 1.38 m, immersed in a 1.412 Tesla solenoidal magnetic field parallel to the beam direction. It has 84 layers of sense wires which are grouped into 9 superlayers as shown in Figure 2.4. Five of these are axial superlayers, each containing 12 layers of wires running parallel to the beam. The axial superlayers are interleaved with 4 stereo superlayers, which consist of six sense wire layers in which the angle with respect to the beam alternates between $\pm 3°$. The combination of axial and stereo layers permits accurate 3-dimensional track

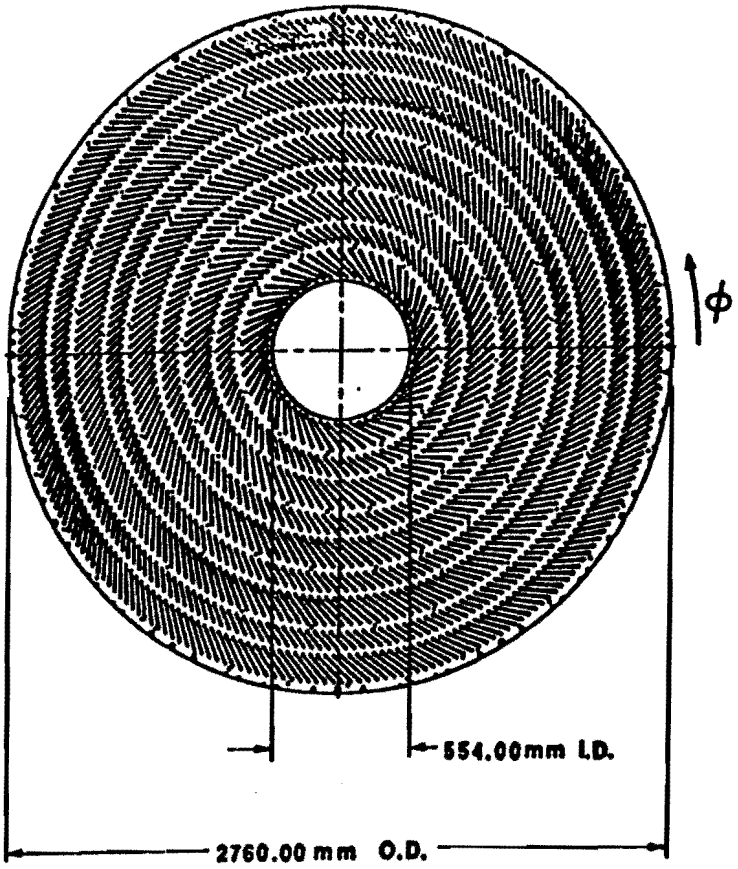

Figure 2.4: End view of the Central Tracking Chamber (CTC), showing the structure of the nine superlayers.

reconstruction. The superlayers are tilted at 45° with respect to the radial direction to account for the Lorentz angle of the electron drift in the magnetic field. The maximum drift distance in the argon-ethane-alcohol medium is less than 40 mm, corresponding to roughly 800 ns of drift-time.

The momentum resolution of the CTC for tracks in the region $|\eta| < 1.0$ (or $40° < \theta < 140°$) is $\Delta P_T/P_T^2 = 0.0017(\ \mathrm{GeV}/c)^{-1}$. This resolution can be improved by imposing the requirement that the tracks emanate from the

beam-line. The beam position may be displaced from the origin by a few hundred microns, and its position is determined for each $\overline{p}p$ store by studying the distribution of the track impact parameter (distance of closest approach of the track to the Z axis) as a function of ϕ. The resolution of the central tracking chamber with a beam-constrained fit is $\Delta P_T/P_T^2 = 0.0011(\ \mathrm{GeV}/c)^{-1}$. The device was calibrated and aligned using a precision magnetic survey, cosmic ray data, and energy/momentum distributions for positively- and negatively-charged electrons [19].

2.2.2 Calorimeters

The calorimeters cover the region $|\eta| < 4.2$ and are organized into systems covering different regions in η : central electromagnetic (CEM) and hadronic (CHA) calorimeters, endwall hadronic calorimeter, plug electromagnetic and hadronic calorimeters, and forward electromagnetic and hadronic calorimeters.

The CEM [20] covers the region $|\eta| < 1.1$, and is segmented into towers of size 0.1 in η by 15° degrees in ϕ that point back to the nominal interaction point $z = 0$. The towers are organized into 4 'arches'. Each arch consists of 12 15° wedges; a schematic view of a wedge is shown in Figure 2.5. Each tower consists of 21 to 31 layers of 5 mm thick SCSN-38 polystyrene scintillator interleaved with $\frac{1}{8}$ inch thick sheets of aluminum-clad lead giving a total of ~ 18 radiation lengths (X_0), including $\sim 1X_0$ from the solenoid magnet coil. Light from the scintillator in each tower is collected on acrylic wavelength shifters and sent through lightguides into two phototubes. The energy resolution of the CEM for electrons is $\Delta E/E \sim 0.14/\sqrt{E}$. The device is calibrated *in situ* using

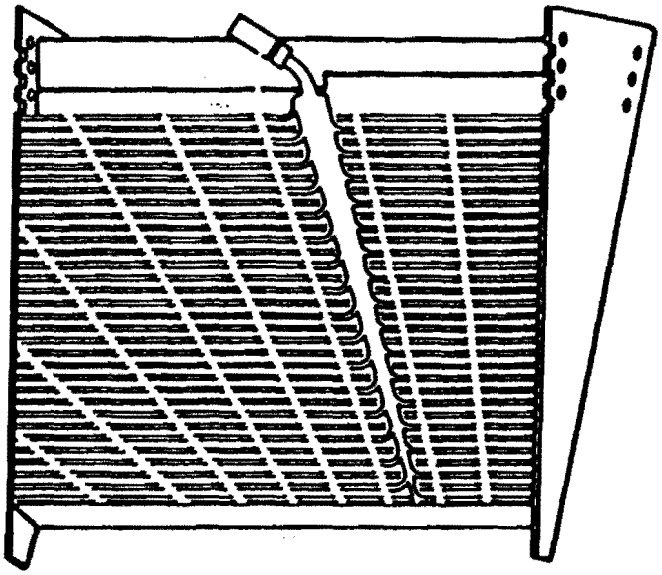

Figure 2.5: A central calorimeter wedge.

LED's, xenon flashers, Cs^{137} sources and energy/momentum distributions for electrons [21].

Inside the CEM, at a depth of 6 X_0 (including the solenoidal coil) corresponding to electromagnetic shower maximum, the Central Strip Chambers (CES) measure the shower profile in both the r-ϕ and z-directions. The strip chambers identify the location of the shower maximum to within $\sim$ 2 mm for 40 GeV test-beam electrons. The matching of the extrapolated track position to a cluster in the strip chambers is a powerful tool in electron analyses. In addition, observed transverse shower profiles can be compared using a χ^2 test to that of testbeam electrons, for additional background rejection.

The central hadron calorimeter (CHA) [22] has the same $\eta - \phi$ segmentation as the central electromagnetic calorimeter, but it only extends to $\eta = 0.9$. The endwall modules extend the coverage of the central hadron

calorimeter out to $\eta = 1.3$; from $\eta = 0.7$ to $\eta = 0.9$, the coverage is shared between the central and endwall calorimeters. The central and endwall calorimeters are 4.7 and 4.5 absorption lengths thick, respectively. The energy resolution of the calorimeters, measured at the testbeam for 50 GeV pions, is 11% and 14% for the central and endwall, respectively [23].

The electromagnetic and hadronic calorimeters in the plug ($1.1 < |\eta| < 2.4$) and forward ($2.2 < |\eta| < 4.2$) regions use gas proportional chambers with cathode pad readout as the active medium. These calorimeters have been described elsewhere [24, 25]. They are used in this analysis to measure the energy in the event coming from particles other than the primary electron or muon; an imbalance in this energy is used to infer the presence of a neutrino.

2.2.3 Central Muon System

The central muon detection system (CMU) [26] consists of four layers of drift chambers located outside the central calorimeters which act as a hadron absorber for the central muon detector. The CMU covers $|\eta| < 0.6$ and is segmented into $\Delta\phi = 12.6°$ wedges that are mounted outside each 15° central calorimeter wedge at a radial distance of 3.5 m from the beam axis. Each CMU wedge is further segmented into three 4.2° modules. And each module consists of four layers of rectangular drift cells of size 63.5 mm in the r-ϕ direction $\times$ 26.8 mm high $\times$ 2261 mm long. A 50 μm sense wire runs down the length of each cell, parallel to the beam axis. The location of the CMU chambers within the central calorimeter is shown in Figure 2.6. The arrangement of the four planes of drift chambers in a module is shown in Figure 2.7.

In 1992, 0.6 m of steel was added behind the CMU for additional hadron absorption, and an additional four layers of drift chambers were added

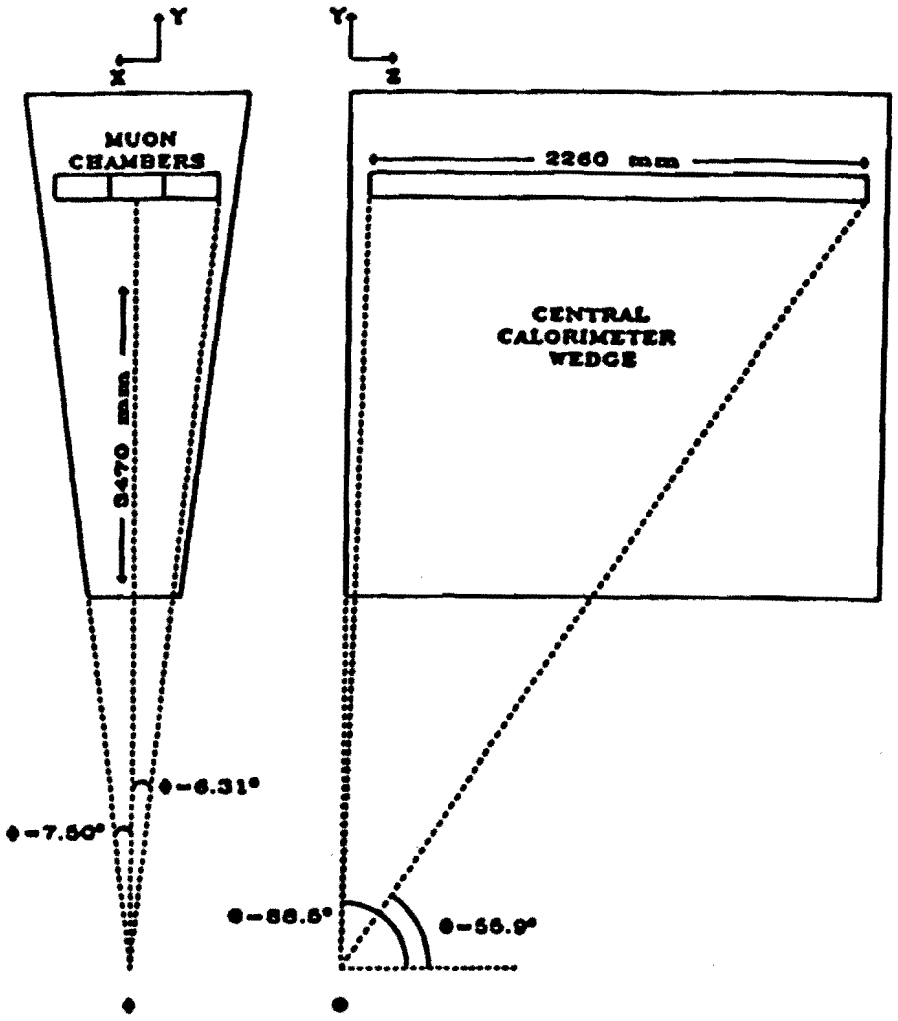

Figure 2.6: View of a central calorimeter wedge, showing the location of the central muon chambers.

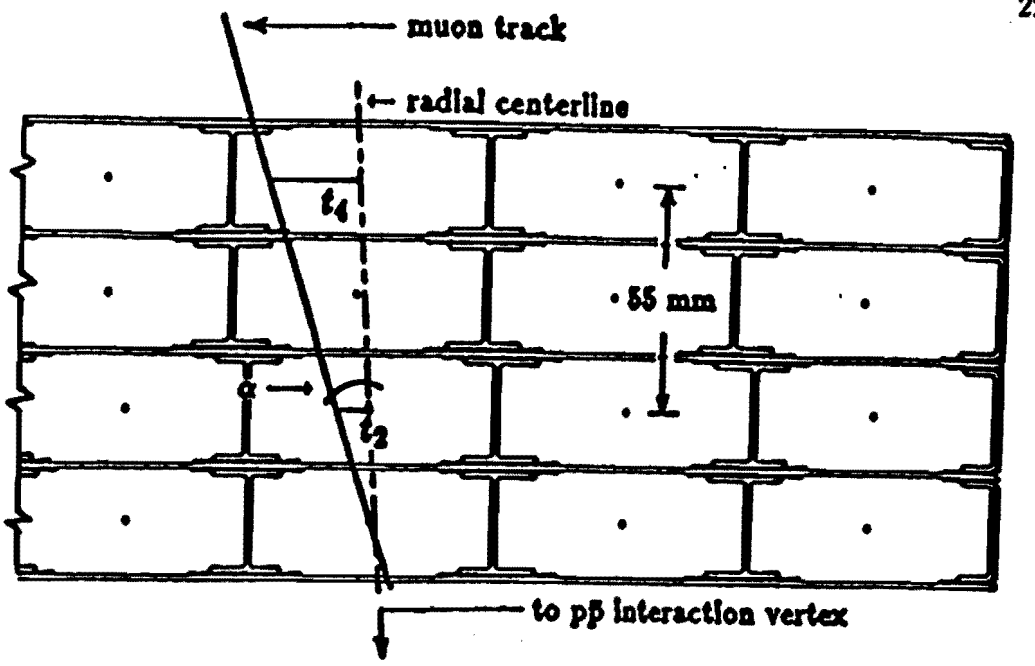

Figure 2.7: View of the four planes of drift chambers in a 15-degree central muon module. The view is along the beam direction.

behind the steel to detect muons. This system is referred to as the central muon upgrade (CMP). Approximately 84% of the solid angle for $|\eta| < 0.6$ is covered by CMU, 63% by CMP and 53% by both. In addition, the coverage of the central muon system has been extended to the pseudorapidity range $0.6 < |\eta| < 1.0$ through the addition of four free-standing conical arches which hold drift chambers for muon detection, sandwiched between scintillator counters for triggering. This system is called the central muon extension (CMX). Approximately 71% of the solid angle for $0.6 < |\eta| < 1.0$ is covered by CMX.

To identify muons, the tracks in either of these chambers are matched to CTC tracks associated with minimum-ionizing energy deposition in the calorimeters.

2.2.4 Luminosity Monitors

An accurate knowledge of the luminosity is important for any cross section measurement. The CDF luminosity is measured using the Beam-Beam Counters (BBC) [27] for detecting inelastic $\bar{p}p$ collisions. The BBC consist of two planes of scintillation counters located perpendicular to the beam-line at a distance of 6 m in Z from the interaction region, covering the angular range of 0.32° to 4.47° with respect to both the proton and antiproton beam directions ($3.24 < |\eta| < 5.88$). Each plane consists of 16 time-of-flight counters which are arranged as shown in figure 2.8. Hits in both counter planes that arrive coincident with the particle bunches crossing through the detector serve as both a minimum-bias trigger and the primary luminosity monitor. The number of coincidences in these counters divided by the effective inelastic cross section covered by the counters is what gives the integrated luminosity.

In previous publications, CDF normalized the BBC cross section ($\sigma_{BBC} = 46.8 \pm 3.2$ mb) to measurements made at $\sqrt{s} = 546$ GeV and extrapolated to $\sqrt{s} = 1800$ GeV [28]. With recent direct measurements of the elastic, diffractive and total cross sections by the CDF collaboration [29], we are able to make a direct measurement of the BBC cross section of $\sigma_{BBC} = 51.2 \pm 1.7$ mb. After accounting for possible backgrounds in the BBC's, we have a total uncertainty of 3.6% on the integrated luminosity for the run.

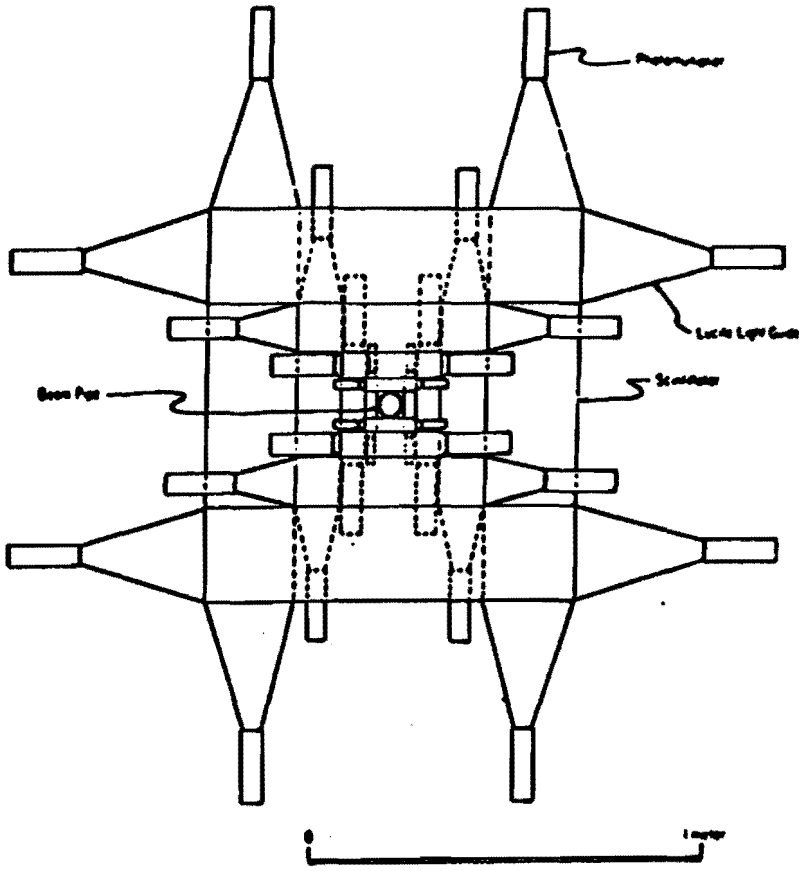

Figure 2.8: Beam's-eye view of one of the beam-beam counters (BBC's).

Chapter 3

Event Selection

3.1 Triggers

In order to observe the most interesting events, a sophisticated trigger system is necessary. The total cross section in the beam-beam counters at $\sqrt{s} = 1.8$ TeV was measured by CDF to be 51.2 mb. The typical instantaneous luminosity during the 1992-93 run was approximately 5×10^{30} cm^{-2} sec^{-1}, which gave an event rate of 250 kHz. The CDF data acquisition system could write only approximately 10 events per second to tape. The solution is a 3-level trigger system [30] designed to obtain the necessary rejection factor. The first two levels are programmable hardware triggers and the third level is a software trigger.

In this analysis, we use the inclusive electron trigger and inclusive muon trigger as the starting point for the event selection.

3.1.1 Inclusive Electron Trigger

The level 1 electron trigger uses sums of energy from the calorimeters to make its decision. Analog signals from the physical calorimeter towers of size 0.1 in η by 5° or 15° in phi are summed into "trigger towers" of size 0.2 in η by 15° in phi. There are a total of 1056 trigger towers: 44×24 to cover the range $-4.4 < \eta < 4.4$ in pseudorapidity and $0° < \phi < 360°$ in azimuthal angle, for both electromagnetic and hadronic calorimeters. The level 1 electron trigger path uses a single-tower threshold of 6 GeV in the central electromagnetic calorimeter. It also requires a coincidence of hits in the east and west BBC arrays in order to signal an inelastic event. As shown in Figure 3.1, the efficiency of this trigger for electrons within the fiducial region of the central calorimeters is 99% for electrons with transverse energy above 9 GeV.

The level 2 electron trigger requires an electromagnetic (EM) trigger tower with transverse energy greater than a threshold of 9 GeV as the seed tower of a calorimeter energy cluster. EM towers adjacent to the seed tower are then added to the cluster if they have $E_T > 7$ GeV. A ratio of hadronic to electromagnetic energy of less than 12.5% is required for the cluster to be an electron candidate. In addition, a hardware track processor ("Central Fast Tracker", or CFT) was used to require a track with $P_T > 9.2$ GeV/c to point at the cluster.

For high E_T ($E_T > 15$ GeV) electrons, the trigger efficiency was measured using $W \rightarrow e\nu$ events to be flat vs. E_T at 93% [31]. Electrons with E_T between 6 and 15 GeV are in the level 2 trigger turn-on region, and thus need to be studied separately. A dielectron data sample is selected from events in which both the level 1 and level 2 inclusive electron triggers fired. We then require that there be two and only two electrons passing the electron

identification cuts described in Table 3.1. At least one of the two electrons has to pass a tight electron identification cut described in Table 3.2 and match a level 2 inclusive electron cluster. This way the other electron in the event can be considered as unbiased by the triggers and can be used to measure the trigger efficiency. The level 2 electron trigger efficiency can be measured by matching the other electron to a level 2 inclusive EM cluster, using the following formula to take into account the cases when both electrons fire the inclusive electron trigger:

$$\epsilon_{trig} = 2N_{tt}/(N_{tt} + N_t)$$

where N_{tt} is the number of events with both electrons passing the trigger and N_t is the total number of events with at least one electron passing the trigger. The efficiency for high E_T electrons is similar to the one measured from the $W \rightarrow e\nu$ sample. The turn on curve of trigger efficiency vs. E_T is shown in Figure 3.1 and used to calculate the total detection efficiency.

In the level 3 electron trigger, the thresholds are sharpened and other cuts are applied. The same electron clustering algorithm used in the off-line analysis (with finer calorimeter segmentation than the Level-2 clustering) is used, and events are required to have a cluster with transverse EM energy $E_T^{EM} > 6$ GeV. A three-dimensional track with $P_T > 4$ GeV/c is required to point to the electron cluster. The ratio of hadronic to electromagnetic energy in the cluster is required to be less than 0.125. After loose electron identification cuts are applied, the average level 3 trigger efficiency for electrons in the fiducial volume is found to be 98.2 $\pm$ 0.1 % [31].

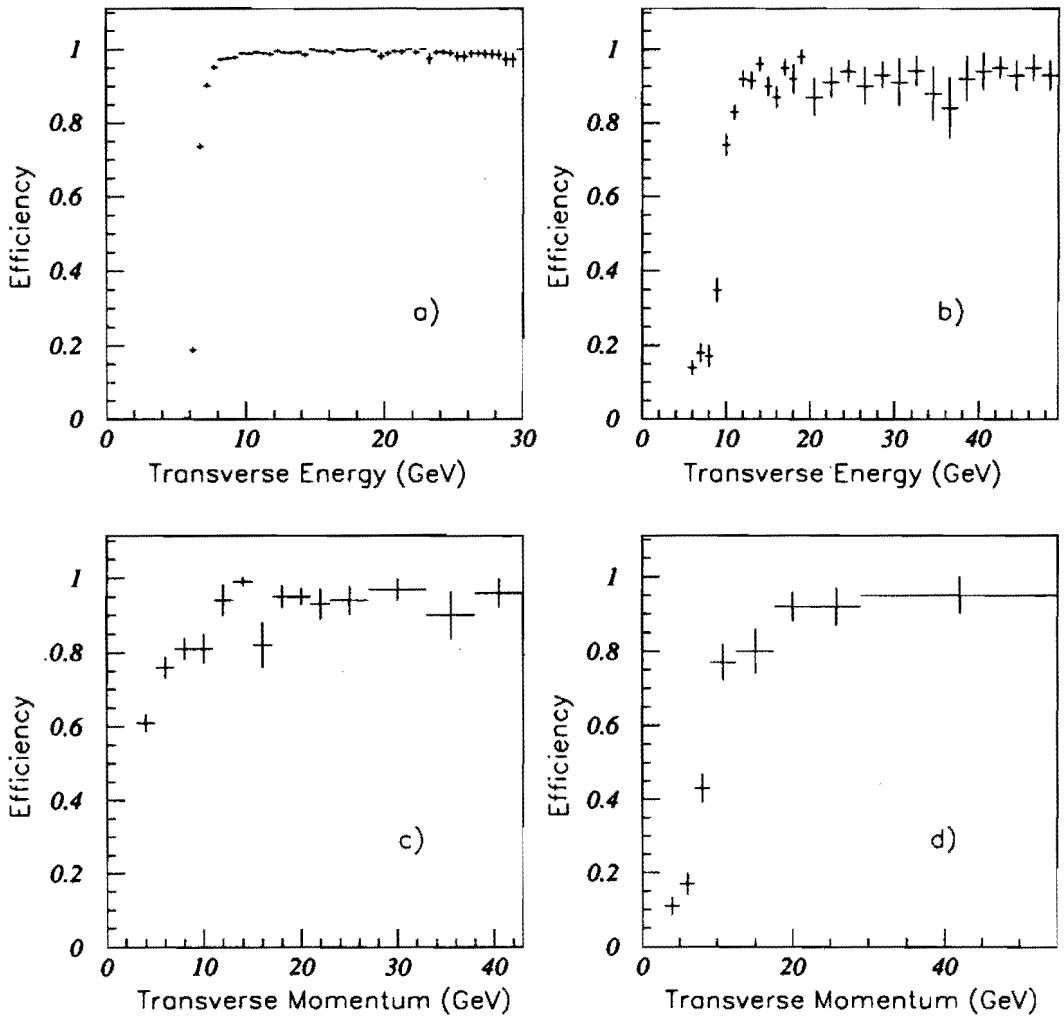

Figure 3.1: Trigger Efficiency vs. the electron E_T in (a) Level 1 and (b) Level 2; Trigger Efficiency vs. the muon P_T in (c) Level 1 and (d) Level 2.

3.1.2 Inclusive Muon Trigger

The level 1 muon trigger [32] requires hits in the central muon chambers ($|\eta| < 1.0$) consistent with a particle originating from the collision region. As can be seen from Figure 2.7, a measurement of the drift time difference between hits in the front and rear pairs of layers of the muon chambers is equivalent to a measurement of the track's azimuthal angle, which in turn is related to the particle's transverse momentum, because of the bending in the central magnetic field and the multiple Coulomb scattering in the calorimeter. The Level-1 muon trigger threshold was 6 GeV/c for the 1992-93 run, and the efficiency curve is shown in Figure 3.1 [33].

Two-dimensional tracks (ϕ and P_T information, but no z information) are found by a hardware processor (CFT) that examines the hits in the axial layers of the CTC. It has a momentum resolution $\Delta P_T/P_T = 3.5\% \times P_T$. The level 2 muon trigger used in this analysis requires a track with $P_T > 9.2$ GeV, whose extrapolated position at the radius of the muon chambers is within 7.5° in azimuth of muon chamber hits that satisfied the level 1 trigger condition. The efficiency of this trigger is 94% for muons with $P_T > 15$ GeV [33]. The turn-on shape of the trigger is shown in Figure 3.1 [33].

The level 3 muon trigger requires a track with $P_T > 7.5$ GeV that extrapolates to a segment of hits in the muon chambers in $|\eta| < 0.6$. It requires a track with $P_T > 10$ GeV in the muon extension chambers in $0.6 < |\eta| < 1.0$. The efficiency of the level 3 muon trigger is 98%.

3.2 Dilepton Data Sample

The data used in this analysis were collected during the Tevatron collider run that took place between August 1992 and June 1993. The total integrated luminosity of the data sample is 19.3 pb^{-1} after excluding 2% from runs which have detector problems (e.g. a large number of dead channels).

A standard offline reconstruction program was applied to all the raw data to convert the direct detector readouts to physics quantities, such as energies, distances and momenta.

Since leptons from $H \rightarrow \tau\nu \rightarrow l\nu\nu\nu$ have much lower energy than those from $W \rightarrow l\nu$, we select dilepton events with low E_T electrons and low P_T muons. We demand at least one lepton with P_T (E_T for electron) > 9 GeV/c and a second lepton with P_T (E_T for electron) > 6 GeV/c. We call it the (9,6) dilepton P_T cut. In Figure 3.2, we plot the P_T distributions of leptons from the decay of τ's and b quarks separately for two possible M_t and M_H combinations. When M_t is very close to M_H, the P_T of leptons from b decay is low, and when $M_t >> M_H$, the P_T of leptons from b decay becomes higher. So our signal dileptons are mainly from $\tau\tau \rightarrow ll$+X, with some contribution from $\tau b \rightarrow ll$+X.

We require the event vertex to be within 60 cm of the center of the detector in order to avoid badly measured calorimeter energy which could produce artificially unbalanced energy transverse to the beam axis, which is called missing E_T ($\not\!\!E_T$). The $\not\!\!E_T$ is defined as the negative of total sum E_T, where the total sum E_T is the vector (directed from the event vertex to the calorimeter tower in the $r - \phi$ plane) sum of the transverse energy in all calorimeter towers in the pseudo-rapidity range $|\eta| < 3.6$. Large $\not\!\!E_T$, not produced by

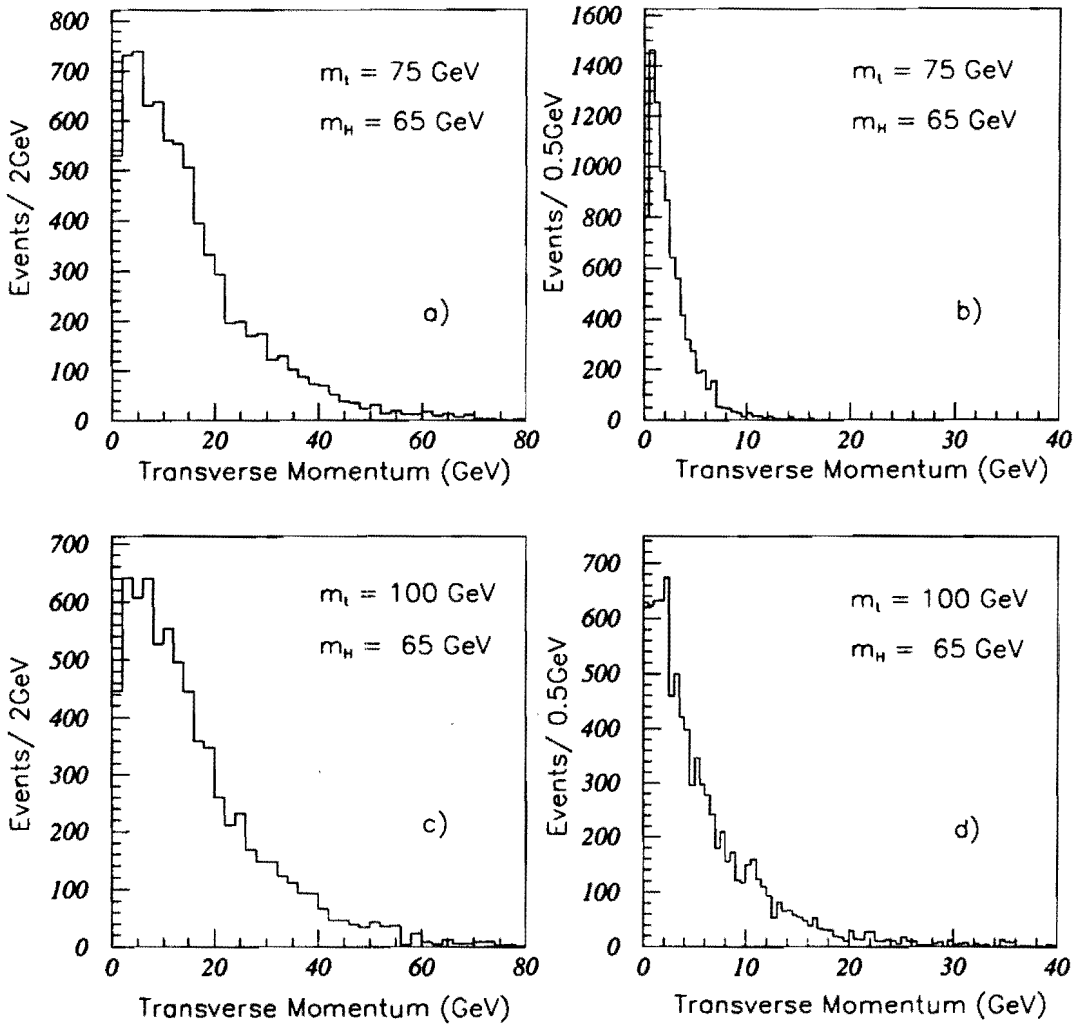

Figure 3.2: The P_T distributions of leptons from the ISAJET Monte Carlo sample. a) P_T of leptons from $H \rightarrow \tau\nu \rightarrow l$+X for M_t = 75 GeV and M_H = 65 GeV. b) P_T of leptons from $b \rightarrow l$+X for M_t = 75 GeV and M_H = 65 GeV. c) P_T of leptons from $H \rightarrow \tau\nu \rightarrow l$+X for M_t = 100 GeV and M_H = 65 GeV. d) P_T of leptons from $b \rightarrow l$+X for M_t = 100 GeV and M_H = 65 GeV.

mismeasurement, indicates that an energetic neutrino was produced in the event.

3.2.1 Electron Identification Cuts

Electromagnetic clusters with an associated track are considered for the electron selection. Electron showers are small relative to the tower dimensions and typically deposit most of their energy in a single calorimeter cell. For electrons sufficiently far from wedge edges to guarantee full calorimeter response, the shower will not cross wedge boundaries. Hence, calorimeter clusters for electron identification are defined with up to three towers adjacent in η. Fiducial cuts are applied on the CEM clusters to avoid cracks between calorimeter modules and to ensure proper energy measurement.

The following variables are used to identify electrons:

(1) *HAD/EM*: The ratio between the hadronic and EM energy in the cluster.

(2) *Lshr*: A measurement of the lateral shower profile of the three-tower cluster. The lateral shower profile is defined as

$$Lshr = \sum_k \frac{E_k^{adj} - E_k^{exp}}{\sqrt{(0.14\sqrt{E})^2 + (\Delta E_k^{exp})^2}} , \qquad (3.1)$$

where the index k of the summation labels the towers adjacent to the seed tower. E_k^{adj} is the measured energy in tower k. E_k^{exp} is the energy expected in tower k. For determining E_k^{exp}, the direction of the electron candidate is calculated by using the event vertex and the position of the shower in the strip chambers. Then, an energy-dependent shower profile obtained from test-beam measurements is used to predict the energy

sharing in the adjacent towers. The normalization of the denominator contains the term ΔE_k^{exp}, which is the error in E_k^{exp} induced by a 1 cm change in the shower position, and the term $0.14\sqrt{E}$, which reflects the statistical fluctuations inherent in the energy measurement of EM showers. The electron energy corresponds to the sum of tower EM energies : $E = \sum E_k$.

(3) E/P: The ratio of the calorimeter cluster energy to the track momentum.

(4) χ^2_{strip}: The χ^2 of the fit of the energy deposited on each of 11 CES strips in the z direction compared to the shower shape of the test-beam electrons. A similar variable χ^2_{wire} tests the observed energy deposition shape on the CES wires in the r-ϕ view.

(5) Δx and Δz: The distance between the extrapolated track position and the strip chamber shower position in the ϕ and z views.

Table 3.1 contains the values of the cuts for the variables used for selecting electrons in this analysis. Figure 3.3 shows distributions of these variables for electrons in $Z \rightarrow ee$ and $J/\psi \rightarrow ee$ events. Electrons from photon conversions are removed by vetoing events containing a second track near the primary track whose charge is opposite and whose invariant mass with the first track is near zero. Very high-P_T conversions may have overlapping, indistinguishable tracks, so we also reject events in which the track left only a small number of hits in the vertex chamber (VTX).

3.2.2 Electron Identification Cut Efficiency

We measure the identification efficiency for electrons using $J/\psi \rightarrow ee$ events (for $E_T < 20$ GeV) and $Z \rightarrow ee$ events (for $E_T > 20$ GeV).

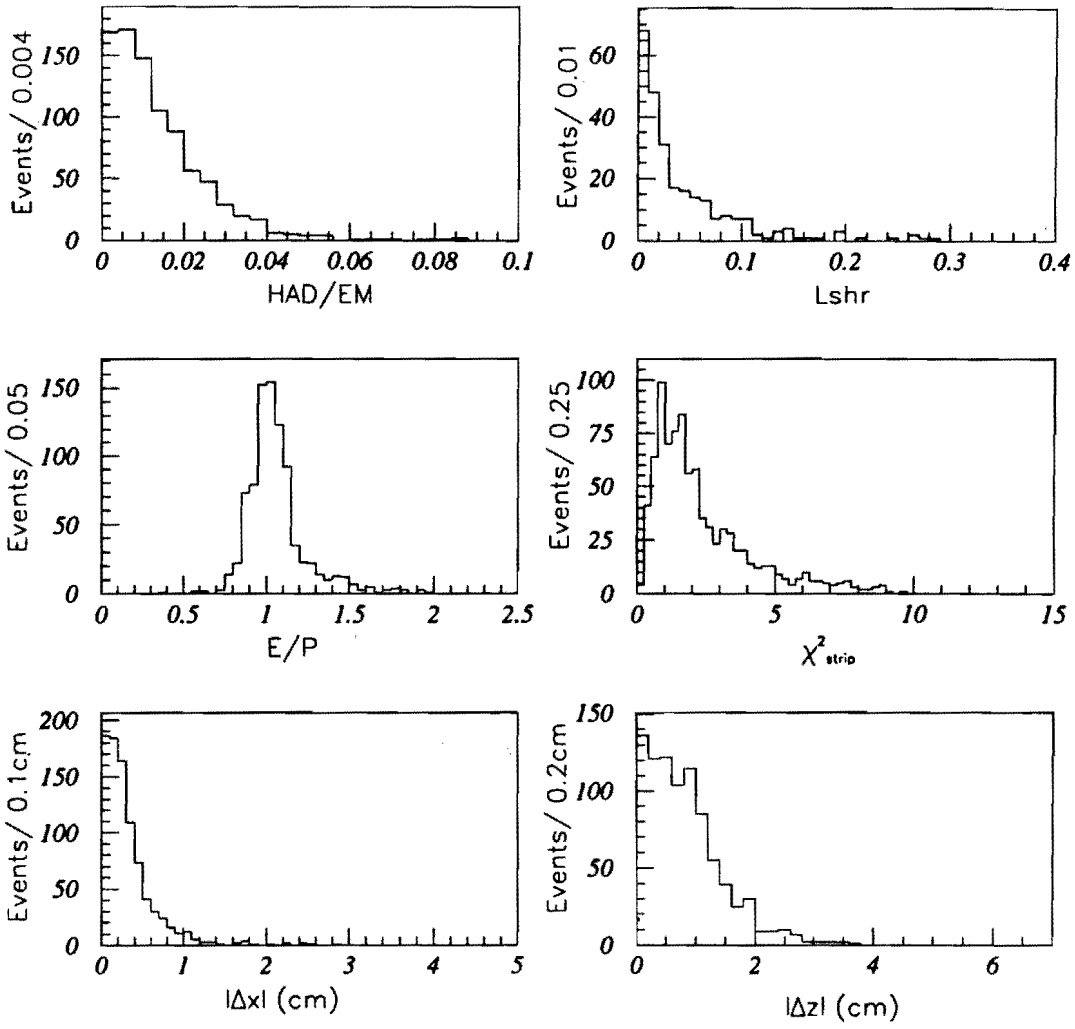

Figure 3.3: Electron identification variables for electrons from the $J/\psi \rightarrow ee$ and $Z \rightarrow ee$ samples.

Variable	Cut
HAD/EM	< 0.05
$Lshr$	< 0.2
E/P	< 1.5
χ^2_{strip}	< 10
Δx	< 3.0 cm
Δz	< 5.0 cm
Efficiency (iso)	(83$\pm$2)%
Efficiency (semi-iso)	(78$\pm$4)%

Table 3.1: Electron selection cuts

First, we select a di-electron sample from events passing the inclusive electron trigger, requiring two electrons (EM clusters) present with at least one passing a set of tight identification cuts with lower E_T and P_T cuts (Table 3.2). We then select $J/\psi \rightarrow ee$ events by reconstructing the invariant mass M_{ee} using the two electron tracks, and requiring 2.95 GeV $< M_{ee} <$ 3.25 GeV. The $Z \rightarrow ee$ events are selected by requiring 83 GeV $< M_{ee} <$ 97 GeV, where M_{ee} is calculated from the electron energies. So the second electron in the J/ψ and Z^0 is unbiased and can be used to measure the efficiency of the identification cuts. The dielectron invariant mass distributions around the two mass regions of the J/ψ and the Z^0 are shown in Figure 3.4 (a) and (b). We find 322 $Z \rightarrow ee$ events and 142 $J/\psi \rightarrow ee$ events after these cuts.

The efficiency of the electron identification cut (labelled i) is then measured by using the following general formula:

$$\varepsilon_i = (N_{tt} + N_{ti})/(N_{tt} + N_t)$$

where N_{tt} is the number of events with both leptons passing the tight identification cuts in Table 3.2, N_{ti} is the number of events with at least one lepton passing the tight cut and the other lepton passing the electron identification

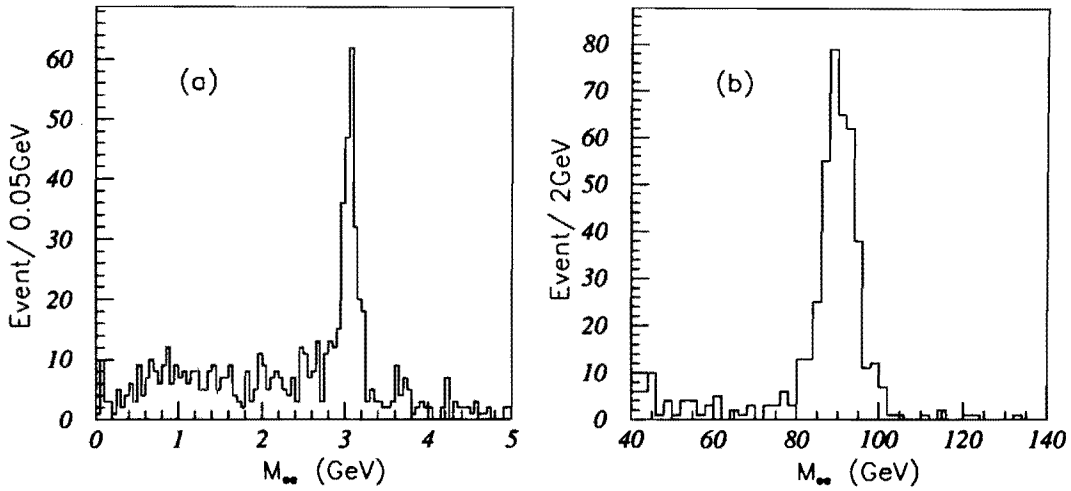

Figure 3.4: Invariant mass distributions of the two electrons near the (a) J/ψ and (b) Z^0 resonant states.

		E_T	>	6 GeV
		P_T	>	4 GeV/c
		HAD/EM	<	0.04
		$Lshr$	<	0.2
0 .75	<	E/P	<	1.5
		χ^2_{strip}	<	10.
		χ^2_{wire}	<	15.
		Δx	<	1.5 cm
		Δz	<	3.0 cm

Table 3.2: Tight electron selection cuts with lower E_T and P_T cuts

cut in Table 3.1, and N_t is the total number of events with at least one lepton passing the tight cut. Within statistics the efficiency is approximately independent of E_T of the electron.

In order to reduce QCD backgrounds, we use a tight-loose isolation cut on the electrons and muons in the top to Higgs analysis, and the isolation cut will be discussed in more detail in Chapter 4. The tight isolation requires the electron candidate to have $E_{iso} < 2$ GeV, where E_{iso} is the energy in a cone of radius 0.4 in η-ϕ space, centered on the electron and excluding the energy in the tower traversed by the electron. The loose isolation requires the electron candidate to have $E_{iso} < 8$ GeV. We calculate the identification efficiency separately for isolated electrons ($E_{iso} < 2$ GeV) and semi-isolated electrons (2 GeV $< E_{iso} <$ 8 GeV). The identification efficiency is found to be (83±2)% for isolated electrons and (78±4)% for semi-isolated electrons (see Table 3.1).

Due to limited statistics of semi-isolated Z^0 events, we use the efficiency of semi-isolated electrons measured from J/ψ events for both $E_T <$ 20 GeV and $E_T >$ 20 GeV. The P_T distribution of semi-isolated leptons for $M_t = 100$ GeV, $M_H = 65$ GeV from the ISAJET Monte Carlo is shown in Figure 3.5. We see that the semi-isolated leptons are mostly low P_T leptons.

3.2.3 Muon Identification Cuts

Muons are selected in the pseudo-rapidity region $|\eta| < 1.0$ by requiring a match between a CTC track and a track segment in the CMU, CMP or CMX muon chambers. These muons are identified by requiring the energy deposition in the calorimeter tower through which a track extrapolates to be consistent with that of a minimum ionizing particle. Cosmic ray backgrounds

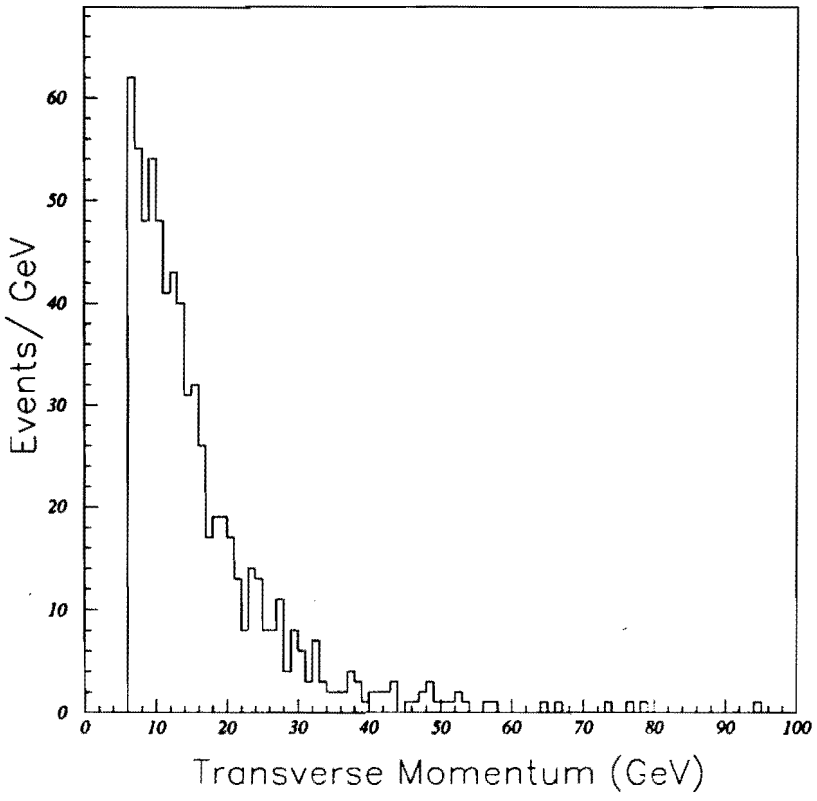

Figure 3.5: P_T distribution of semi-isolated electrons or muons for $M_t = 100$ GeV, $M_H = 65$ GeV from the ISAJET Monte Carlo.

are removed by rejecting back-to-back tracks within 0.5° in azimuth and 0.1 in pseudo-rapidity.

The following requirements are used to select muons:

(1) Minimum ionization requirement: The calorimeter tower to which the CTC track points is required to contain less than 2 GeV of energy in the electromagnetic compartment, less than 5 GeV of energy in the hadronic compartment, but more than 0.1 GeV in the sum of the two compartments.

(2) Impact parameter cut: The CTC track must have an impact parameter (the distance of closest approach of the reconstructed track to the beam line) $d_0 < 0.3$ cm.

(3) z-vertex match: the distance between the interaction vertex and the reconstructed track in the z direction has to be less than 5 cm.

(4) Track-stub match. The matching distance between the extrapolated CTC track and the track segment in the muon chambers, $|\Delta x| = r \cdot \Delta\phi$, must be less than 10 cm for a CMU stub, or less than 15 cm for a CMP or CMX stub.

Table 3.3 contains the values of the cuts for the variables used for selecting muons in this analysis. Figure 3.6 shows distributions of these variables for muons in $Z \rightarrow \mu\mu$ and $J/\psi \rightarrow \mu\mu$ events.

3.2.4 Muon Identification Cuts Efficiency

Similarly to the electron case, the efficiency of the muon selection criteria can be measured for high P_T muons using a sample of $Z \rightarrow \mu\mu$ and for low P_T muons using a sample of $J/\psi \rightarrow \mu\mu$.

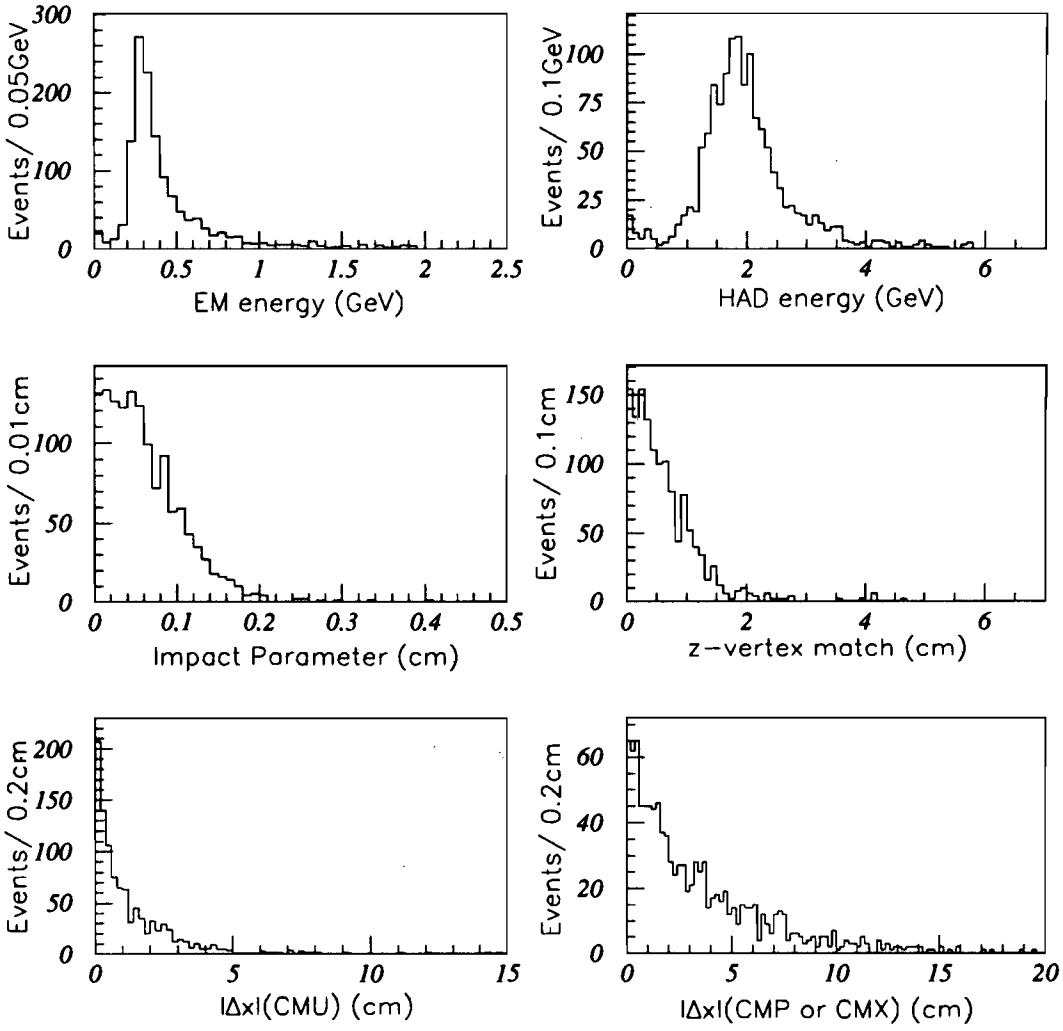

Figure 3.6: Muon identification variables for muons from the $J/\psi \rightarrow \mu\mu$ and $Z \rightarrow \mu\mu$ samples.

Variable	Cut
EM energy	< 2 GeV
HAD energy	< 5 GeV
EM+HAD energy	> 0.1 GeV
Impact parameter	< 3 mm
z-vertex match	< 5 cm
$\|\Delta x\|$	< 10 cm (CMU)
	< 15 cm (CMP, CMX)
Efficiency (iso)	(96.1±1.0)%
Efficiency (semi-iso)	(92.3±1.8)%

Table 3.3: Muon selection cuts

The $Z \rightarrow \mu\mu$ events are selected by requiring at least one muon with $P_T > 20$ GeV passing the muon quality cuts described in Table 3.3 and a second muon with $P_T > 20$ GeV. The reconstructed invariant mass $M_{\mu\mu}$ using the two muon tracks is required to be within 7 GeV of the Z mass. The $J/\psi \rightarrow \mu\mu$ events are selected with lower P_T requirement ($P_T > 6$ GeV) for the two muons. At least one of the muons has to pass the cuts in Table 3.3 and the invariant mass is required to be 2.95 GeV $< M_{\mu\mu} <$ 3.25 GeV. The dimuon invariant mass distributions around the two mass regions of the J/ψ and the Z^0 are shown in Figure 3.7 (a) and (b). The $Z \rightarrow \mu\mu$ sample has 266 events and the $J/\psi \rightarrow \mu\mu$ sample has 389 events.

Most of the J/ψ's produced at CDF result from the decays of particles containing a b quark. These particles are produced in pairs, and the other b in the event often decays hadronically. Thus, J/ψ's are often accompanied by jet activity, which affects the muon isolation. Thus the identification efficiency is studied separately for isolated muons with $E_{iso} < 2$ GeV and semi-isolated muons with 2 GeV $< E_{iso} <$ 8 GeV. The identification efficiency is found to

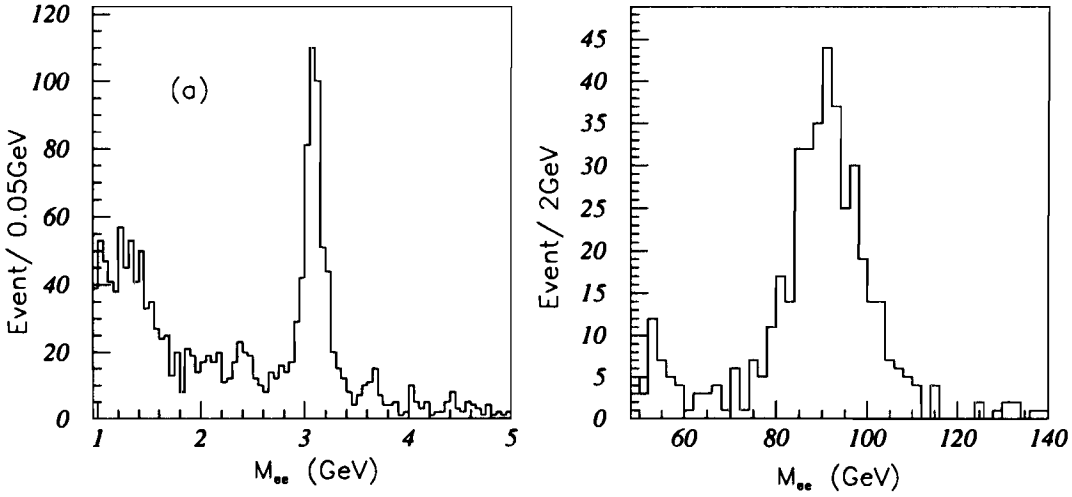

Figure 3.7: Invariant mass distributions of the two muons near the (a) J/ψ and (b) Z^0 resonant states.

be (96.1±1.0)% for isolated muons and (92.3±1.8)% for semi-isolated muons (see Table 3.3).

Chapter 4

Strategy and Results of the Search

4.1 Signal and Backgrounds Samples

We have studied the signal and backgrounds using various data and Monte Carlo samples. For signal, we have used the ISAJET Monte Carlo to generate samples of $t\bar{t}$ events with M_t from 70 to 110 GeV/c^2, the region that this search is sensitive to. For a given M_t and M_H combination, we simulated three processes: $t\bar{t}\rightarrow HbHb$, $t\bar{t}\rightarrow HbWb$ and $t\bar{t}\rightarrow WbWb$. Dilepton backgrounds from QCD production and decay of heavy flavors were simulated with ISALEP [34], the special version of ISAJET that allows generation of bottom and charm pairs by higher order diagrams, including flavor excitation and gluon splitting. For the background from $Z \rightarrow \tau\tau$, we use a $Z \rightarrow ee$ sample from data with the electrons replaced by simulated τ's. For the Drell-Yan continuum, we use the Z^0 sample to study the event topology. For W pair production, we also generate the events with ISAJET Monte Carlo. For the W + jet background,

we use the generic jet data sample to study the probability of a jet being misidentified as an electron or a muon.

With all Monte Carlo samples, the response of the CDF detector to the final state particles is simulated with a full detector simulation to enable the sample of the Monte Carlo events to be subjected to the same cuts as are applied to the data.

4.2 The Definition of the Signal Region

We distinguish our $t\bar{t}$ signal from the dominant backgrounds by exploiting the marked difference in the event topology.

The following topology cuts are used to define the signal region:

(1) Isolation cut: one lepton with $E_{iso} < 2$ GeV and the other lepton with $E_{iso} < 8$ GeV. Most of the leptons from $b\bar{b}$ or $c\bar{c}$ decays, as well as jets misidentified as leptons, are not isolated. On the contrary, leptons from top to charged Higgs to τ decays are usually well isolated. The isolation distributions of leptons from $H \rightarrow \tau\nu$ decays and leptons from $b\bar{b}$ events in the ISAJET Monte Carlo samples are shown in Figure 4.1. The cut $E_{iso} < 2$ GeV is chosen to optimize the efficiency of the leptons from tau decays against the leptons from b decays in the $b\bar{b}$ background. But we also expect some fraction of signal events to have one of the leptons originate from semileptonic b decay. Thus, by comparing the scatter plot of the isolation distribution of the two leptons in the signal Monte Carlo for different M_t and M_H combinations and the $b\bar{b}$ background in Figure 4.2, we choose our isolation cut on the second lepton as $E_{iso} < 8$ GeV. The scatter plot of the isolation distribution of the two leptons

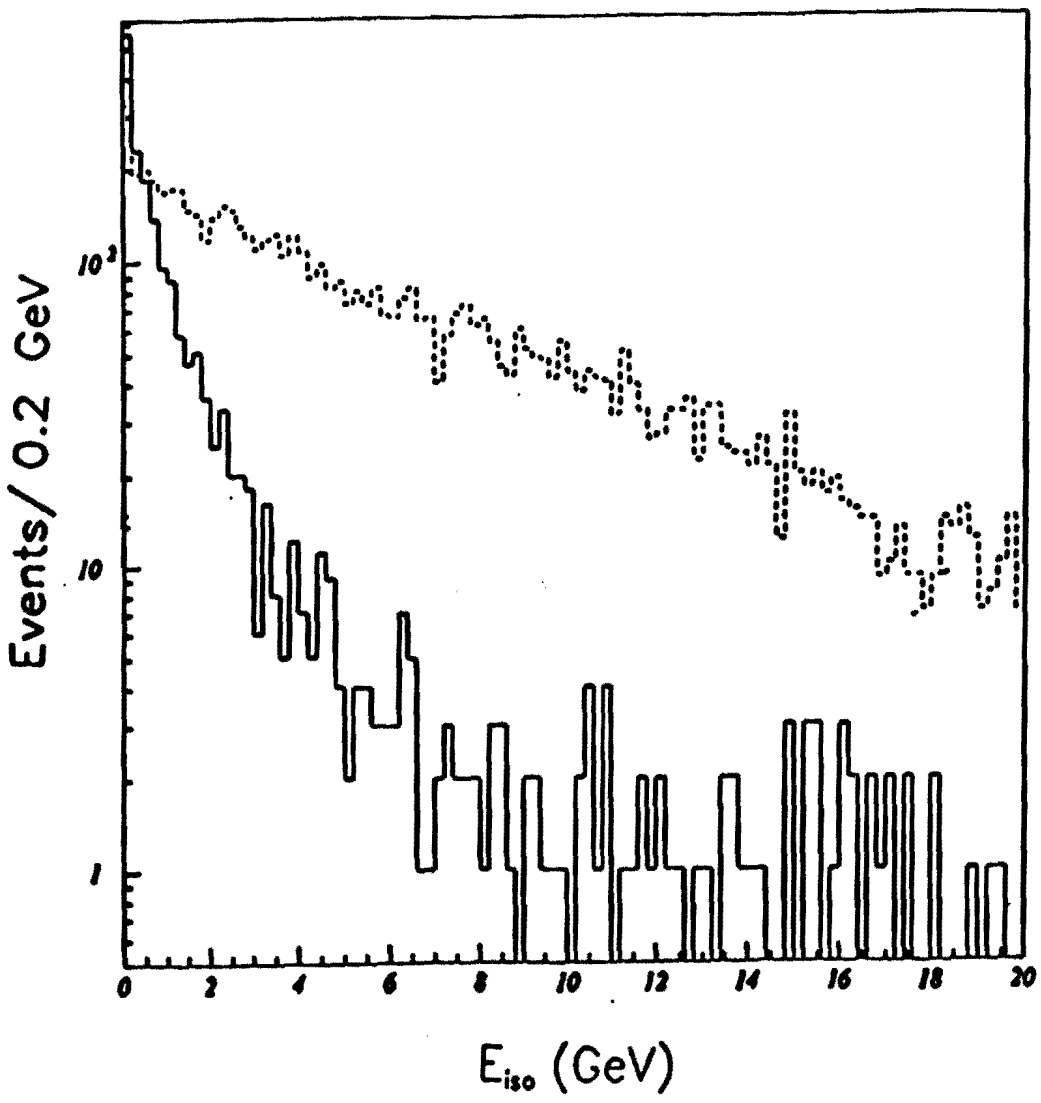

Figure 4.1: Isolation distribution of leptons from the Monte Carlo events of $H \rightarrow \tau\nu \rightarrow l + X$ (solid line) and leptons from the Monte Carlo events of $b\bar{b} \rightarrow l + X$ (dashed line). The luminosities are not normalized.

from the $t\bar{t}\rightarrow WbWb$ Monte Carlo events is also shown in Figure 4.2 (d).

(2) Mass cut: For ee and $\mu\mu$ events, we remove the J/ψ, Υ, low mass Drell-Yan and b sequential decays ($b\rightarrow cl\nu\rightarrow sll\nu\nu$) by requiring $M_{ee,\mu\mu} >$ 12 GeV and remove the Z^0 by cutting out $70 < M_{ee,\mu\mu} < 110$ GeV. For $e\mu$ events, we use a cut of $M_{e\mu} > 10$ GeV to remove b sequential decays. The invariant mass distributions of the two leptons in CDF data events are shown in Figure 4.3. We can see the nice resonant states of Υ and Z^0 in the ee and $\mu\mu$ events. The peak around 20 GeV in the ee, $\mu\mu$ and $e\mu$ events is due to the (9,6) P_T cut.

(3) $\not\!\!E_T > 20$ GeV: The $\not\!\!E_T$ distributions of $t\bar{t}\rightarrow HbHb$ events for $M_t = 100$ GeV, $M_H = 65$, 80, 95 GeV are shown in Figure 4.4, as well as the $\not\!\!E_T$ distribution of $t\bar{t}\rightarrow WbWb$ events for $M_t = 100$ GeV. Figure 4.5 shows the $\not\!\!E_T$ distributions of the $b\bar{b}$, $Z \rightarrow \tau\tau$, $Z \rightarrow ee$ and $Z \rightarrow \mu\mu$, and W pair background samples. We can see that most of the background events have low $\not\!\!E_T$ comparing with the signal events in Figure 4.4, while W pair events have as much $\not\!\!E_T$ as the signal with a much lower production cross section (the production cross section of a 100 GeV top quark is 10 times higher than that for W pair production). The cut $\not\!\!E_T > 20$ GeV is very efficient in rejecting several major backgrounds, while it reduces the signal detection efficiency by about 30%.

(4) $\not\!\!E_T$ significance more than 2.4: The $\not\!\!E_T$ significance, denoted as S, is defined as $\not\!\!E_T$ divided by the square root of the total scalar sum E_T of the event. The energetic neutrinos in $t\bar{t}$ decay produce large S in contrast to some of the dominant backgrounds in which there is not significant $\not\!\!E_T$ (see Figure 4.6). In other electroweak analyses from CDF, minimum-bias

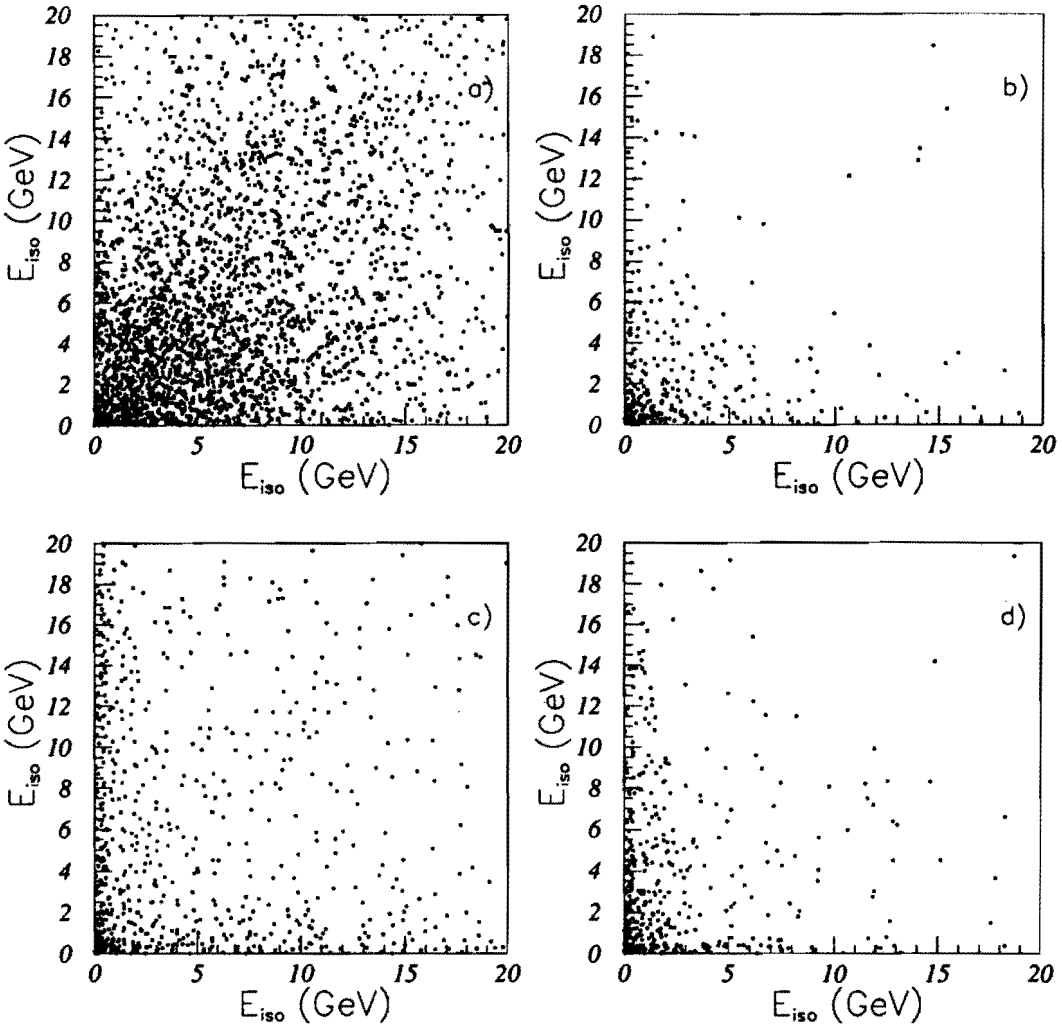

Figure 4.2: Isolation distribution of the two leptons (a) in $b\bar{b}$ events, (b) in $t\bar{t}\rightarrow HbHb$ events with $M_t = 100$ GeV and $M_H = 95$ GeV, (c) in $t\bar{t}\rightarrow HbHb$ events with $M_t = 100$ GeV and $M_H = 65$ GeV, and (d) in $t\bar{t}\rightarrow WbWb$ events with $M_t = 100$ GeV. The luminosities are not normalized in these plots.

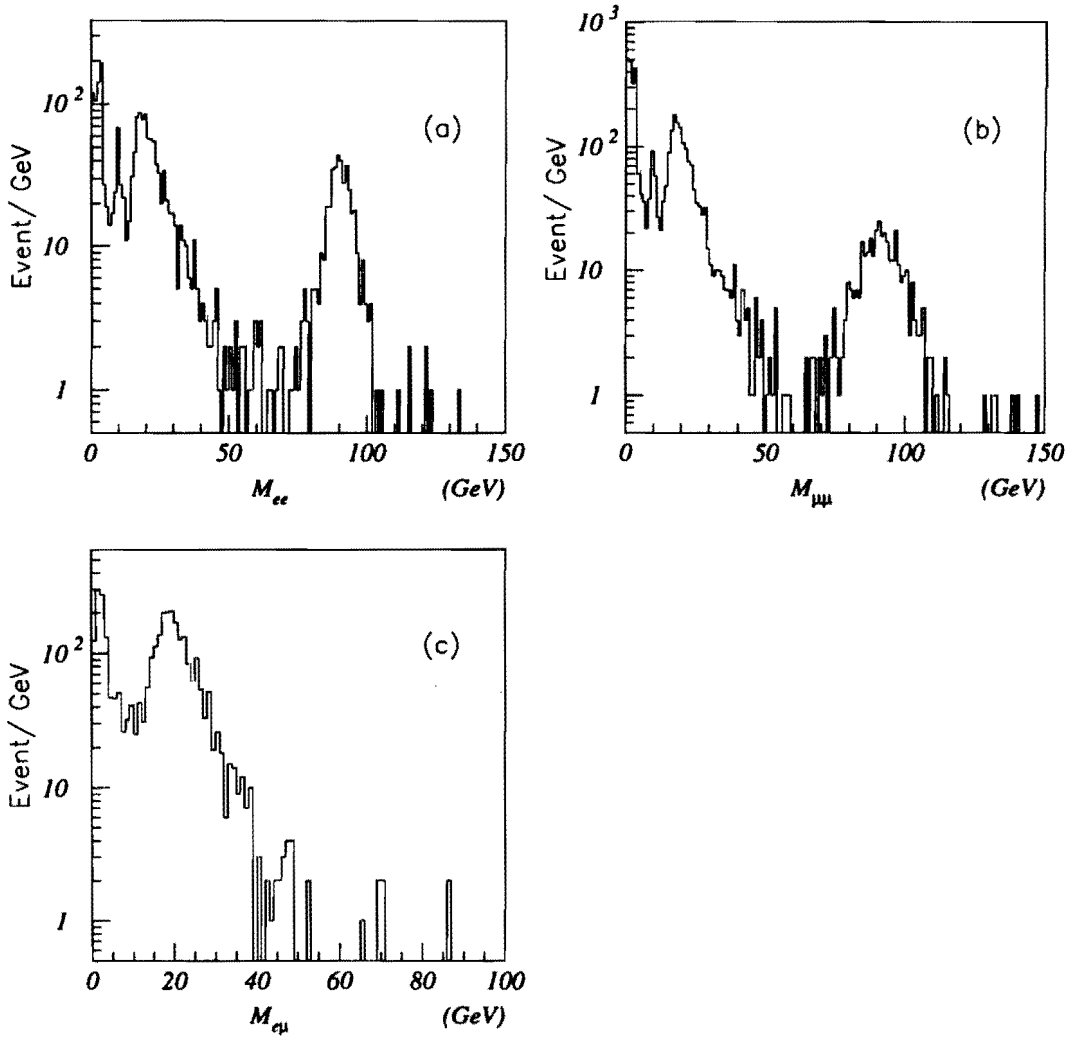

Figure 4.3: Invariant mass distributions of dilepton data events.
a) Invariant mass of ee events, b) Invariant mass of $\mu\mu$ events, c) Invariant mass of $e\mu$ events.

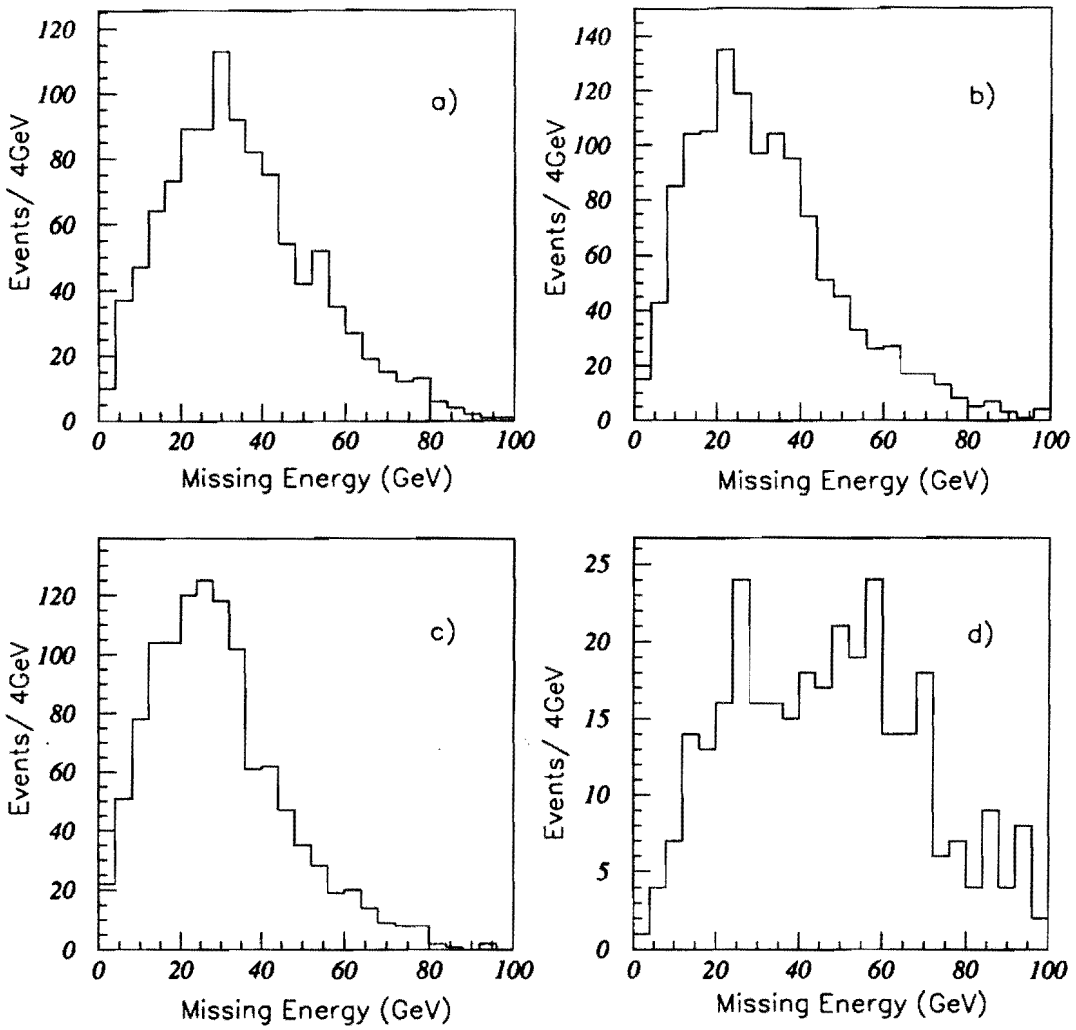

Figure 4.4: Missing transverse energy distributions of signal Monte Carlo events with BR($H \to \tau\nu$)=100%.
a) $t\bar{t} \to HbHb$, M_t= 100 GeV/c^2 and M_H= 95 GeV/c^2,
b) $t\bar{t} \to HbHb$, M_t= 100 GeV/c^2 and M_H= 80 GeV/c^2,
c) $t\bar{t} \to HbHb$, M_t= 100 GeV/c^2 and M_H= 65 GeV/c^2,
d) $t\bar{t} \to WbWb$, M_t= 100 GeV.

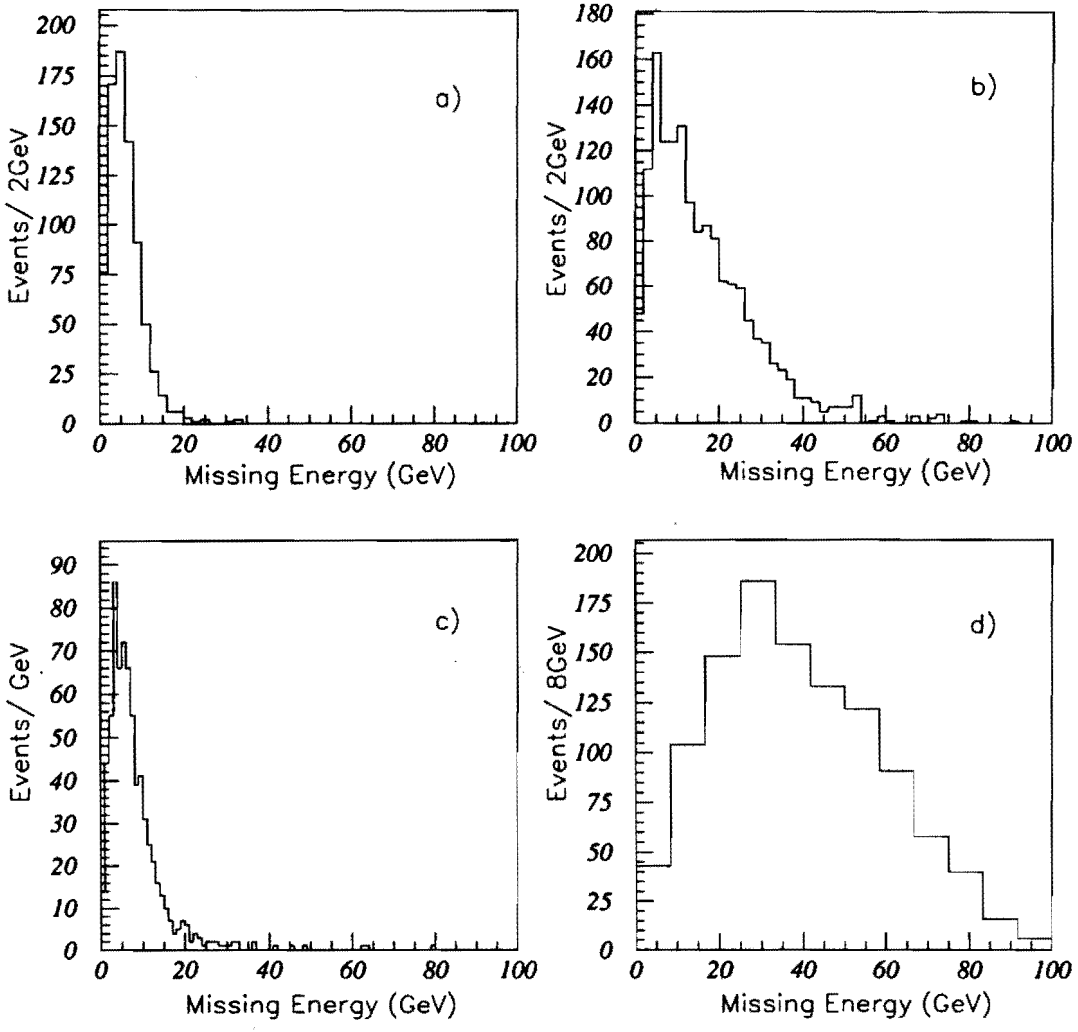

Figure 4.5: Missing transverse energy distributions of background events. a) $b\bar{b}$, b) $Z \to \tau\tau$, c) $Z \to ee$ and $Z \to \mu\mu$, d) W pair.

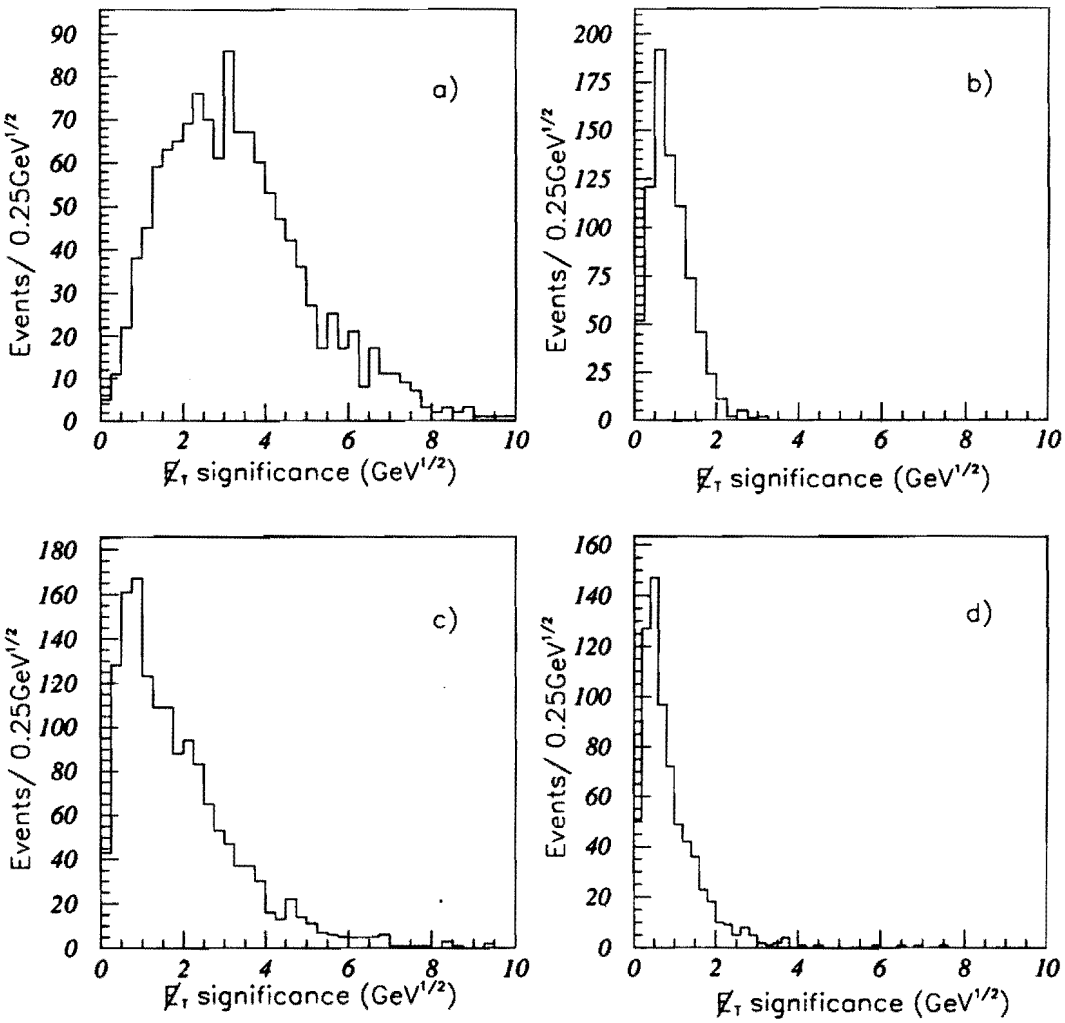

Figure 4.6: Distributions of $\not\!\!E_T$ significance for a) $t\bar{t}\rightarrow HbHb$ Monte Carlo events with $M_t = 100$ GeV/c^2 and $M_H = 80$ GeV/c^2, b) $b\bar{b}$, c) $Z \rightarrow \tau\tau$, d) $Z \rightarrow ee$ and $Z \rightarrow \mu\mu$.

events taken during the course of normal data taking are used to study the $\not\!\!E_T$ response in the detector [35]. The cut value, S > 2.4, corresponds to approximately 4 sigma.

(5) W removal: For events which have a high P_T (> 25 GeV/c) lepton with E_{iso} < 2 GeV, we require the azimuthal angle, $\Delta\phi$, between the $\not\!\!E_T$ direction and this lepton to be less than 165°. This cut reduces background from W + jet events in which the W decays leptonically and the jet is misidentified as a lepton, since the high P_T lepton and the $\not\!\!E_T$ from a real W tend to be back-to-back in the transverse plane. The distribution of $\Delta\phi$ between $\not\!\!E_T$ and the isolated high P_T lepton for $t\bar{t}\rightarrow HbHb$ Monte Carlo events is shown in Figure 4.7 (a), while the same distribution for W + jet data events is shown in Figure 4.7 (b). Also from the $Z \rightarrow \tau\tau$ background study, we find that this cut efficiently suppresses the $Z \rightarrow \tau\tau$ background as shown in Figure 4.7 (c).

(6) $\Delta\phi$ between $\not\!\!E_T$ and the closest jet ($\Delta\phi_{\nu jet}$) must be > 30°: This cut rejects events in which the mismeasurement of jets produces a large $\not\!\!E_T$. In this case the $\not\!\!E_T$ tends to point in the direction of the mismeasured jet. Figure 4.8 shows the distributions of $\Delta\phi_{\nu jet}$ vs. $\not\!\!E_T$ for $t\bar{t}\rightarrow HbHb$ Monte Carlo events in (a), and for $Z \rightarrow ee$ and $Z \rightarrow \mu\mu$ events in (b). From Figure 4.8, we can see that the cut $\Delta\phi_{\nu jet}$ > 30° is efficient in rejecting Drell-Yan background after the $\not\!\!E_T$ > 20 GeV cut.

(7) $\Delta\phi$ between $\not\!\!E_T$ and the closest lepton ($\Delta\phi_{\nu l}$) must be > 30°: This cut is primarily used to reject $Z \rightarrow \tau\tau$ events since the neutrinos and the lepton from the τ decay tend to point in the same direction. Figure 4.9 shows the distributions of $\Delta\phi_{\nu l}$ vs. $\not\!\!E_T$ for $t\bar{t}\rightarrow HbHb$ Monte Carlo events in (a), and for $Z \rightarrow ee$ and $Z \rightarrow \mu\mu$ events in (b). From Figure 4.9, we can

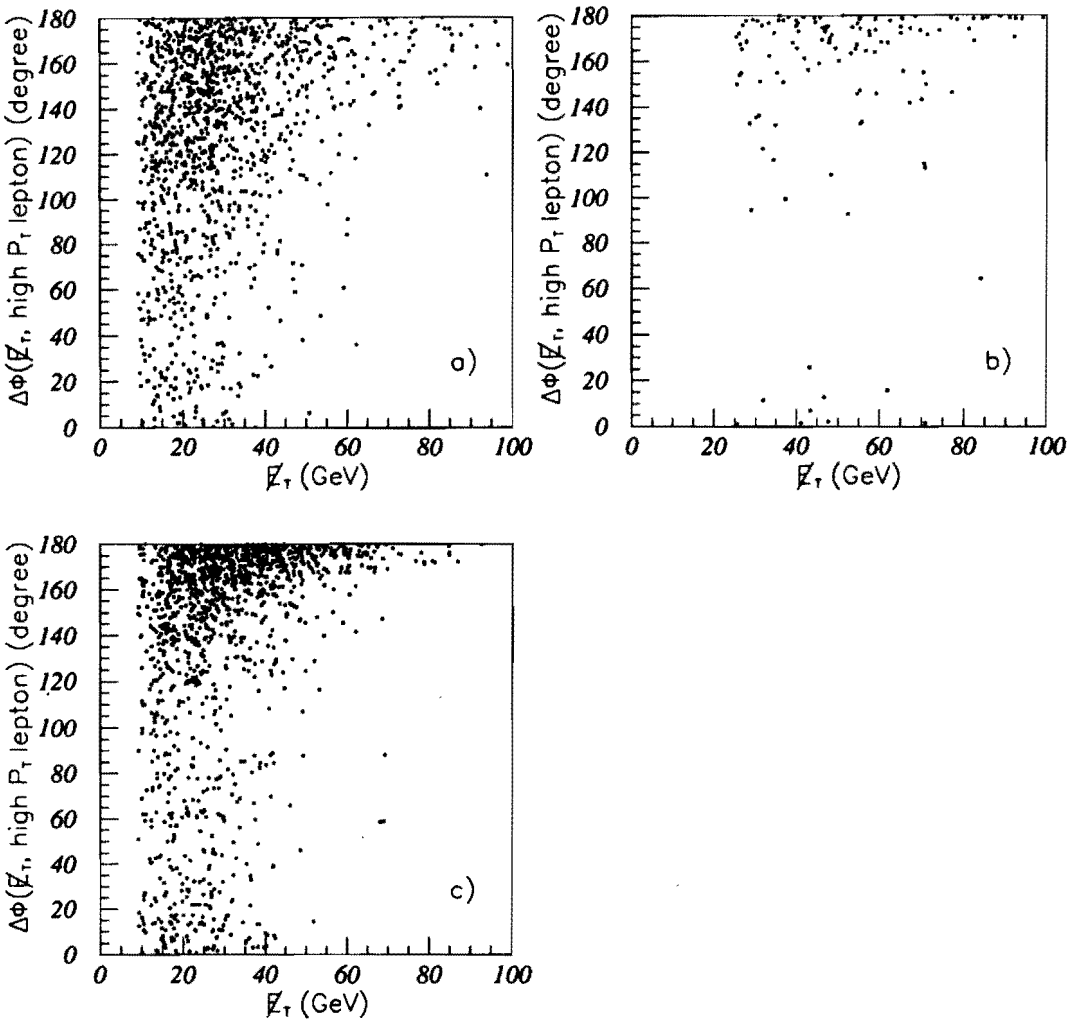

Figure 4.7: Distributions of $\Delta\phi$ between $\not\!\!E_T$ and the isolated high P_T lepton a)for $t\bar{t}\rightarrow HbHb$ Monte Carlo events with $M_t = 100$ GeV/c^2 and $M_H = 80$ GeV/c^2, (b)for W + jet data sample and (c)for $Z \rightarrow \tau\tau$ Monte Carlo sample.

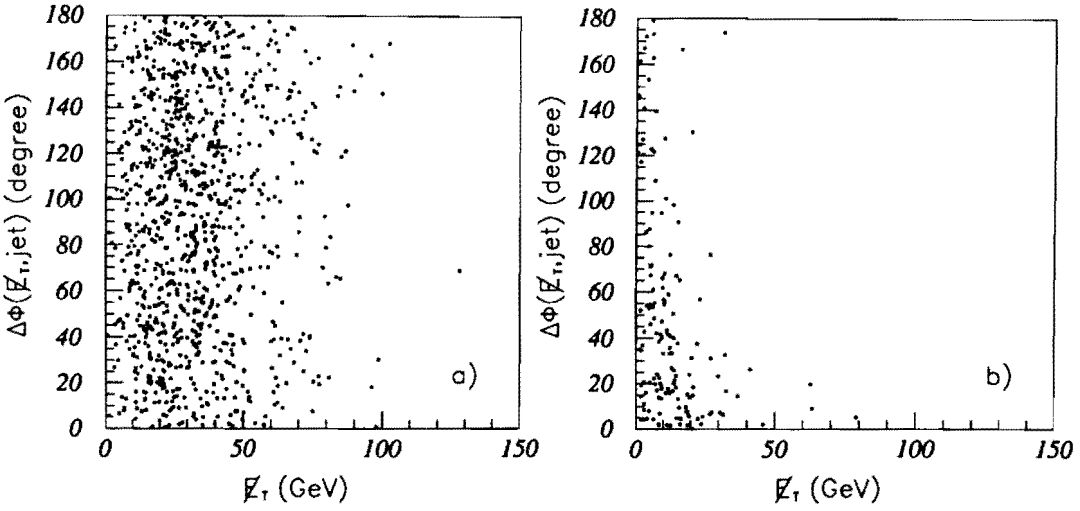

Figure 4.8: Distributions of $\Delta\phi_{\nu jet}$ vs. $\not\!\!E_T$ for $t\bar{t}\rightarrow HbHb$ Monte Carlo events in (a), and for $Z \rightarrow ee$ and $Z \rightarrow \mu\mu$ events in (b).

see that the cut $\Delta\phi_{\nu l} > 30°$ is efficient in rejecting $Z \rightarrow \tau\tau$ background after the $\not\!\!E_T > 20$ GeV cut.

4.3 Acceptance of the Signal

The number of signal events expected in the data sample can be written as

$$N_{exp} = \mathcal{L} \cdot \sigma_{t\bar{t}} \cdot BR \cdot \varepsilon_{total}$$

where $\mathcal{L}$ is the integrated luminosity, $\sigma_{t\bar{t}}$ is the top quark production cross section, ε_{total} is the total detection efficiency, and BR is the branching ratio for $t\bar{t}$ decay to ee, $\mu\mu$ or $e\mu$, and is a function of M_t, M_H and $\tan\beta$.

The total detection efficiency ε_{total} is decomposed into the following parts: i) $\varepsilon_{geom \cdot P_T}$: the geometrical acceptance of the detector and the efficiency of P_T (E_T) cuts, ii) ε_{event}: the efficiency of event topology cuts(defined in

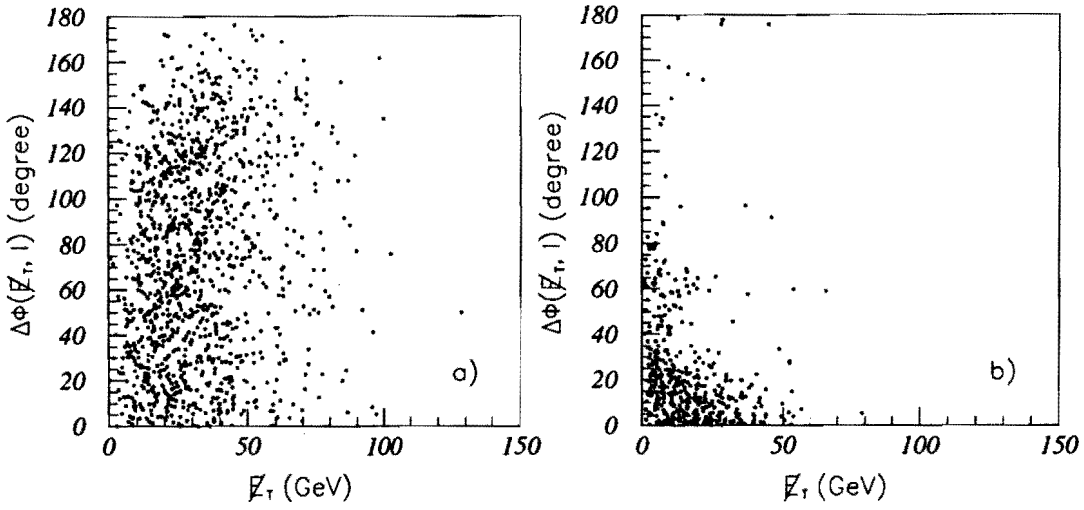

Figure 4.9: Distributions of $\Delta\phi_{\nu l}$ vs. $\not\!\!E_T$ for $t\bar{t}\rightarrow HbHb$ Monte Carlo events in (a), and for $Z \rightarrow \tau\tau$ events in (b).

section 4.2), iii) ε_{id}: the efficiencies of electron and muon identification, iv) ε_{trig}: the trigger efficiencies. Thus $\varepsilon_{total}= \varepsilon_{geom\cdot P_T}\cdot\varepsilon_{event}\cdot\varepsilon_{id}\cdot\varepsilon_{trig}$.

As discussed in Chapter 3, the lepton identification efficiencies ε_{id} are calculated by using J/ψ and Z^0 data for isolated and semi-isolated leptons separately. The trigger efficiencies ε_{trig} are also determined from data.

We calculate $\varepsilon_{geom\cdot P_T}$ and ε_{event} from the ISAJET Monte Carlo samples. Assume N_1 is the number of events passing the (9,6) P_T cut with two leptons in the detector fiducial regions and N_{total} is the total number of $t\bar{t}$ events generated. Then $BR\cdot\varepsilon_{geom\cdot P_T}= N_1/N_{total}$. Since the lepton identification efficiencies ε_{id} are calculated separately from data, the lepton identification cuts are not applied to the Monte Carlo events. The number of events passing all cuts except lepton identification cuts divided by N_1 gives ε_{event}.

We simulate three processes for each M_t and M_H combination: $t\bar{t}\rightarrow HbHb$, $t\bar{t}\rightarrow HbWb$ and $t\bar{t}\rightarrow WbWb$. We call these HH, HW, and WW events. For each

Cut	Efficiency		
	WW	HH	HW
Iso cut for boson-boson	0.842±0.058	0.849±0.027	0.820±0.027
Iso cut for boson-b	0.470±0.048	0.523±0.020	0.437±0.019
mass cut	0.845±0.046	0.883±0.022	0.884±0.035
$\not\!\!E_T > 20$ GeV	0.872±0.051	0.708±0.022	0.834±0.033
S > 2.4	0.908±0.056	0.888±0.030	0.911±0.037
W removal cut	0.779±0.055	0.825±0.031	0.745±0.029
$\Delta\phi(\not\!\!E_T$,jet) cut	0.851±0.063	0.905±0.035	0.891±0.037
$\Delta\phi(\not\!\!E_T$,l) cut	0.922±0.072	0.797±0.035	0.843±0.038
all cuts	0.263±0.019	0.227±0.010	0.229±0.010

Table 4.1: Topology cut efficiencies for signal Monte Carlo events with $M_t = 100$ GeV and $M_H = 80$ GeV.

process (HH, HW or WW), we consider two contributions. First is the boson-boson contribution which is when both leptons come from boson (Higgs or W) decays. Second is the boson-b contribution which is when one of the two leptons comes from a boson (Higgs or W) decay and the other lepton comes from a b decay.

Table 4.1 shows the breakdown of the efficiencies for each topology cut in the case of $M_t = 100$ GeV, for HH, HW events with $M_H = 80$ GeV, and for WW events. Because the isolation of leptons from the boson-boson contribution is very different from the isolation of leptons from the boson-b contribution, we list the isolation cut efficiency for the boson-boson contribution and the boson-b contribution separately.

Table 4.2 summarizes $BR{\cdot}\varepsilon_{geom{\cdot}P_T}$, ε_{event}, ε_{id}, ε_{trig} and $BR{\cdot}\varepsilon_{total}$ for $M_t = 100$ GeV and $M_H = 65$, 80 and 95 GeV. We also list in Table 4.2 the fractions of dilepton events from the boson-boson contribution, $F_{boson-boson}$,

M_{top}	100 GeV						
M_{Higgs}	-	65 GeV		80 GeV		95 GeV	
TYPE	WW	HH	HW	HH	HW	HH	HW
$BR{\cdot}\epsilon_{geom{\cdot}P_T}(\%)$	2.94±0.11	4.55±0.09	4.04±0.08	3.88±0.08	3.54±0.08	2.31±0.06	2.91±0.07
$\epsilon_{event}(\%)$	26.3±1.9	16.2±0.8	19.7±1.0	22.7±1.0	22.9±1.0	36.9±1.6	29.3±1.3
$\epsilon_{id}(\%)$	78.6±2.4	79.7±2.4	78.9±2.4	79.5±2.4	78.4±2.4	79.2±2.4	78.5±2.4
$\epsilon_{trig}(\%)$	84.0±1.6	82.2±1.6	82.6±1.6	81.6±1.6	85.6±1.6	88.1±1.7	86.7±1.7
$BR{\cdot}\epsilon_{total}(\%)$	0.51±0.03	0.49±0.03	0.52±0.03	0.57±0.03	0.55±0.03	0.59±0.03	0.58±0.03
$F_{boson-boson}(\%)$	63.8±3.8	59.4±2.4	64.9±2.2	66.2±2.2	64.9±2.2	98.4±0.6	79.5±1.8
$F_{boson-b}(\%)$	36.2±3.8	40.6±2.4	35.1±2.2	33.8±2.2	35.1±2.2	1.6±0.6	20.5±1.8

Table 4.2: The $t\bar{t}$ detection efficiencies for signal Monte Carlo events with $M_t = 100$ GeV. $F_{boson-boson}$ and $F_{boson-b}$ are the fractional contributions of dileptons from the boson-boson and the boson-b decays respectively, after the topology cuts. Only the Monte Carlo statistical uncertainty is included in the errors.

and the fractions of dilepton events from the boson-b contribution, $F_{boson-b}$. These fractions are calculated after the event topology cuts.

4.4 The Data

In the 19.3 pb^{-1} data sample, we have 9204 events which pass the inclusive electron trigger or the inclusive muon trigger path after the (9,6) P_T cut and lepton identification cuts.

In Table 4.3 we list the numbers of events which pass the topology cuts in sequence. After the isolation, invariant mass, $\not\!\!E_T$ significance and W removal cuts, we plot the azimuthal angle between the direction of $\not\!\!E_T$ and the direction of the closest lepton or jet versus the $\not\!\!E_T$ in Figure 4.4. Two candidate events are found after all the topology cuts.

One candidate event is an $e\mu$ event found also in the high P_T top dilepton search [5]. The event(R47122/E38382) contains a positron with $E_T =$ 50.6 GeV and a negative muon with $P_T = 37.3$ GeV/c and $\not\!\!E_T = 59.6$ GeV. The azimuthal angle separation between the leptons is 21 degrees. There are 3 jets,

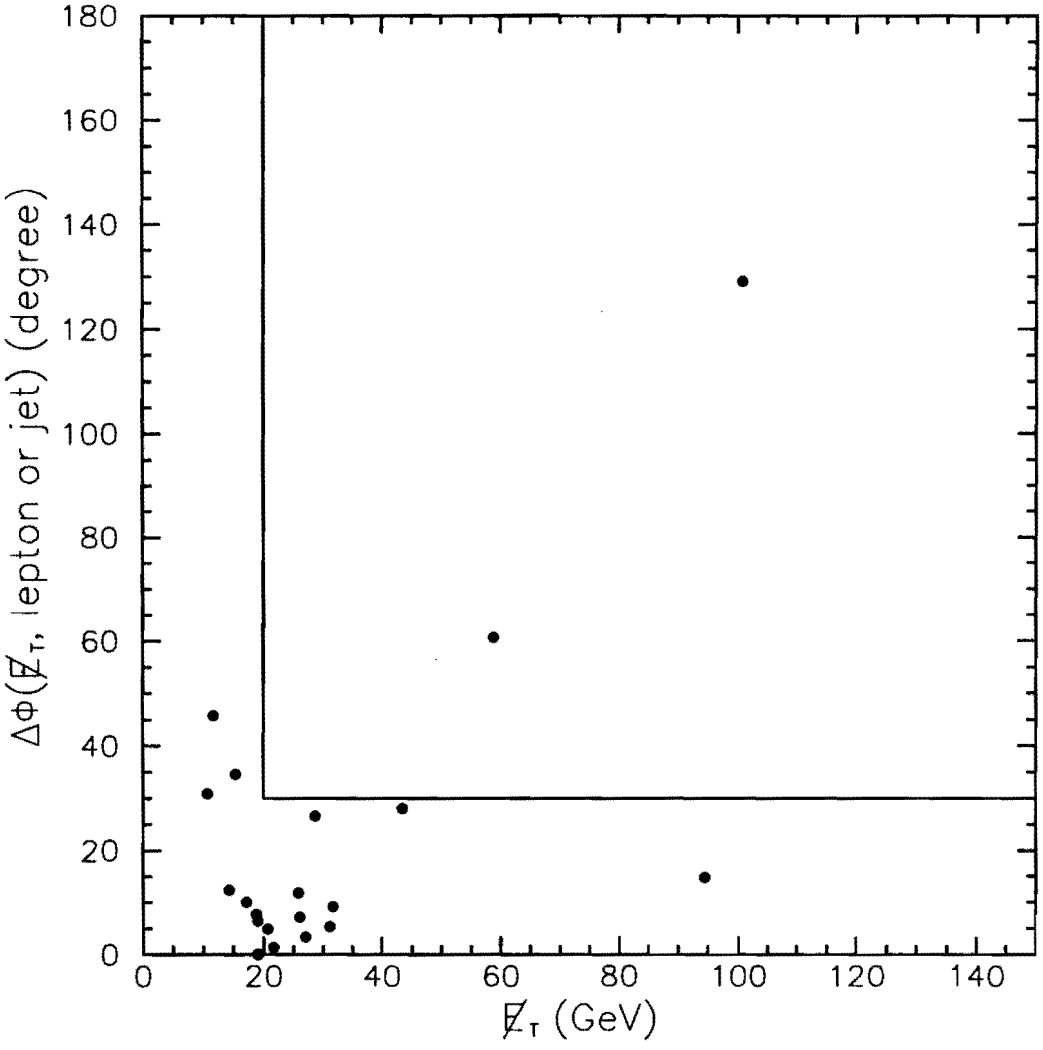

Figure 4.10: Distribution of $\Delta\phi(\not\!\!E_T$-lepton or jet) vs. $\not\!\!E_T$ after isolation, invariant mass, $\not\!\!E_T$ significance and W removal cuts for the data events.

Cuts	Events Surviving
P_T,fiducial,ID	9204
Isolation	3868
Invariant Mass	2009
$\not\!\!E_T > 20$ GeV	39
S > 2.4	27
W removal	12
$\Delta\phi(\not\!\!E_T$, l or jet) > 30°	2
All cuts	2

Table 4.3: Number of data events which pass the topology cuts.

	Run 47122 Charge	Event 38382 P_T (GeV/c)	η	ϕ (degree)
Central electron	+	50.6	0.93	25
Central muon	−	37.3	−0.74	4
Jet 1		67.0		
Jet 2		13.6		
Jet 3		10.7		
$\not\!\!E_T$		59.6		149
$\Delta\phi$ ($\not\!\!E_T$,lepton)				124
$\Delta\phi$ ($\not\!\!E_T$,jet)				68

Table 4.4: Characteristics of the $e\mu$ candidate event. Jet energy is the raw calorimeter energy deposited in a cone of 0.4.

with E_T's of 67, 14, and 11 GeV. Figures 4.11 and 4.12 show a CTC display and a calorimeter display for the $e\mu$ candidate event. The characteristics of the $e\mu$ event are summarized in Table 4.4.

The other one is an ee event with 100 GeV $\not\!\!E_T$. The azimuthal angle separation between the positron (with $E_T = 11.6$ GeV) and the electron (with $E_T = 10.7$ GeV) is 42°. There are 3 jets in this event, with E_T's of 45, 44 and

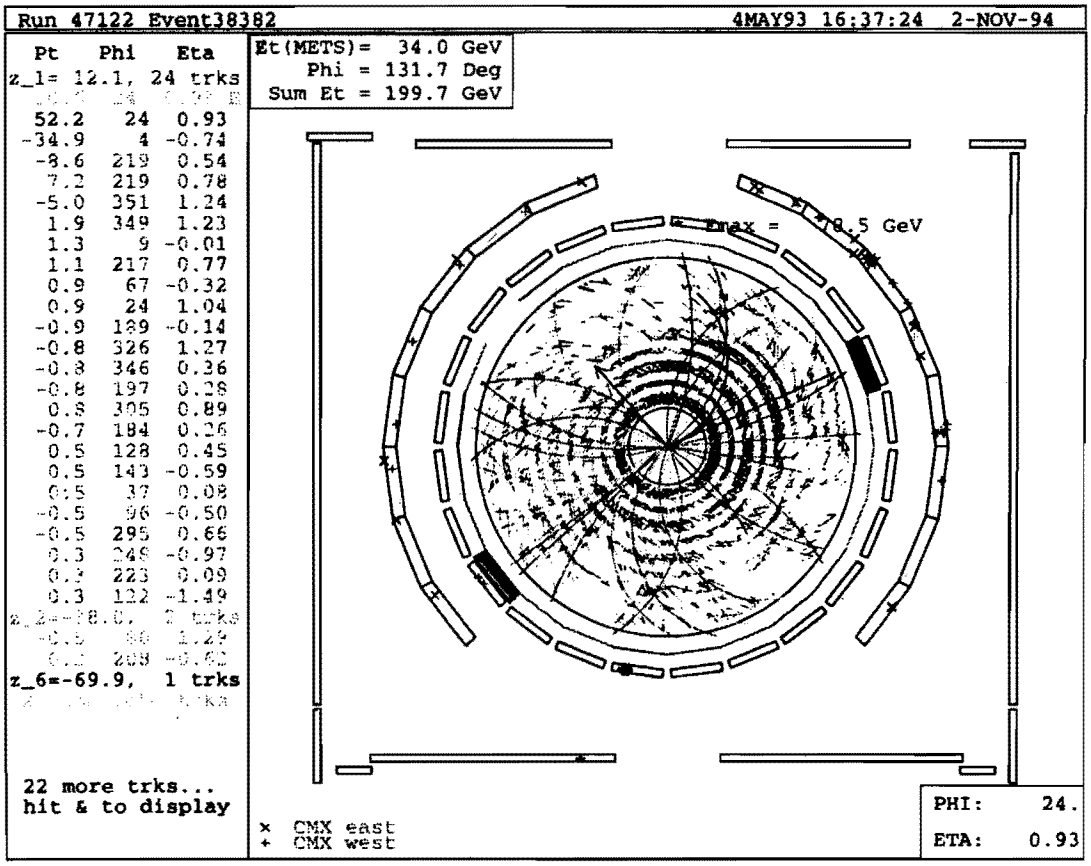

Figure 4.11: A CTC display of the $e\mu$ candidate event.

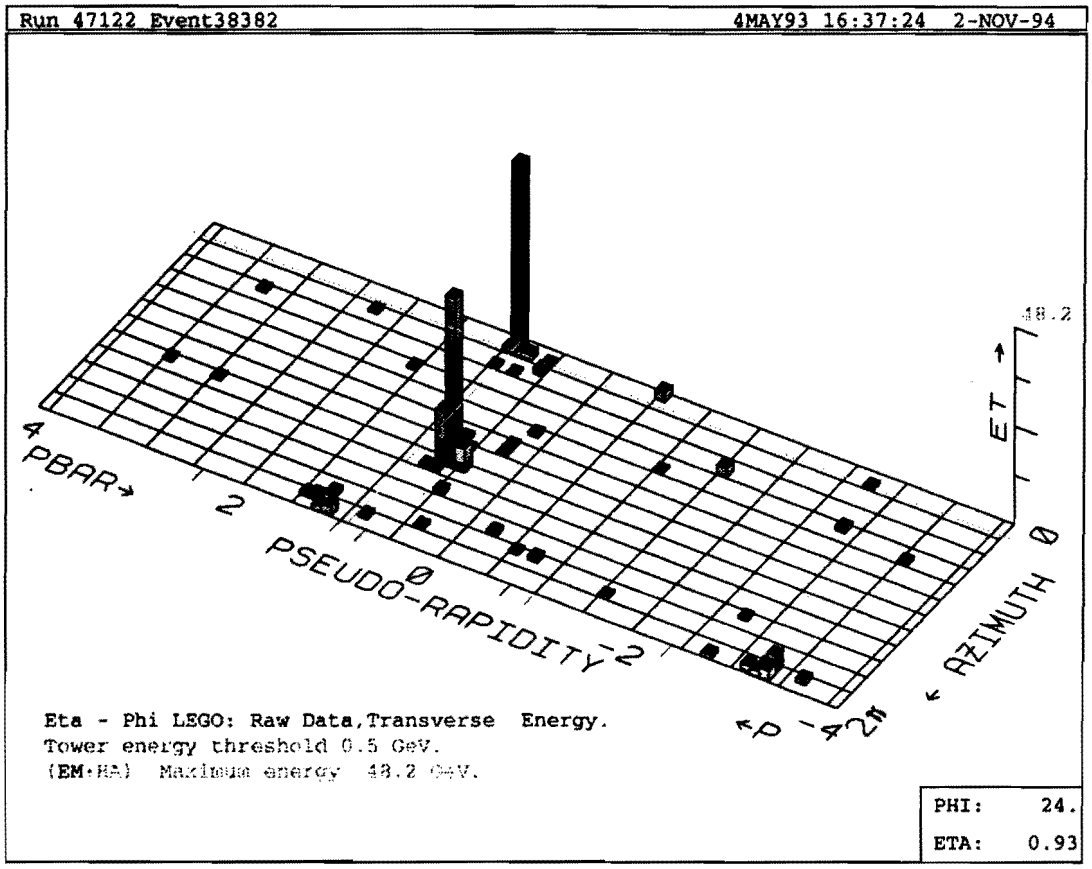

Figure 4.12: A calorimeter display of the $e\mu$ candidate event.

	Run 46518 Charge	Event 16303 P_T (GeV/c)	η	ϕ (degree)
Central electron	+	11.6	0.89	142
Central electron	−	10.7	−0.22	184
Jet 1		44.8	0.08	232
Jet 2		43.8	1.59	158
Jet 3		13.0	2.86	158
$\not\!\!E_T$		100.5		0
$\Delta\phi$ ($\not\!\!E_T$,lepton)				144
$\Delta\phi$ ($\not\!\!E_T$,jet)				128

Table 4.5: Characteristics of the ee candidate event. Jet energy is the raw calorimeter energy deposited in a cone of 0.4.

13 GeV. Figures 4.13 and 4.14 show a CTC display and a calorimetry display for the ee candidate event. The characteristics of the ee event are summarized in Table 4.5.

4.5 Background Expectation

The main backgrounds in the dilepton sample are $Z \rightarrow \tau\tau$, Drell-Yan($\gamma/Z^0 \rightarrow l^+l^-$, where $l = e$ or μ), QCD production of $b\bar{b}$ or $c\bar{c}$, and W + jet with the W decaying into $l\nu$ and the jet misidentified as a lepton. There are also contributions from diboson production (WW, WZ). In this section we discuss each background separately.

4.5.1 $Z \rightarrow \tau\tau$

We have simulated the $Z \rightarrow \tau\tau$ sample from out data sample of 1113 $\gamma/Z^0 \rightarrow ee$ events. We replace the electron with a τ that has the same P_T.

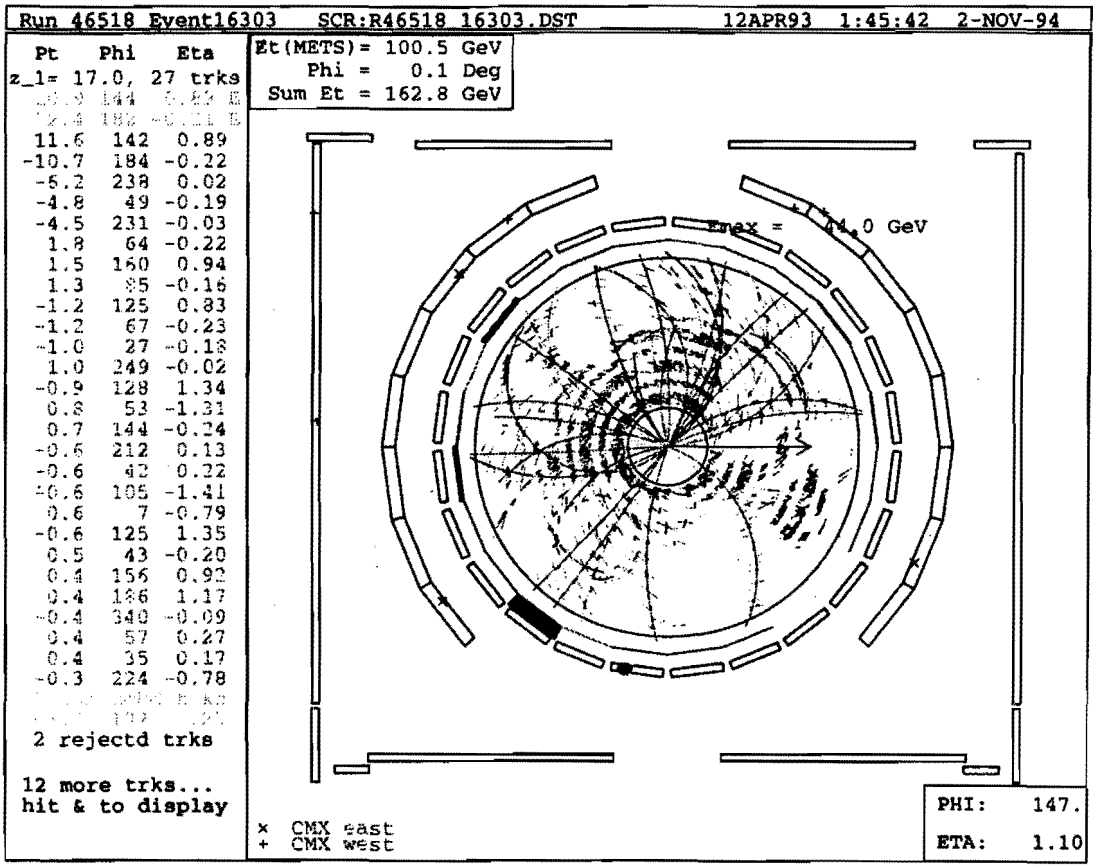

Figure 4.13: A CTC display of the *ee* candidate event.

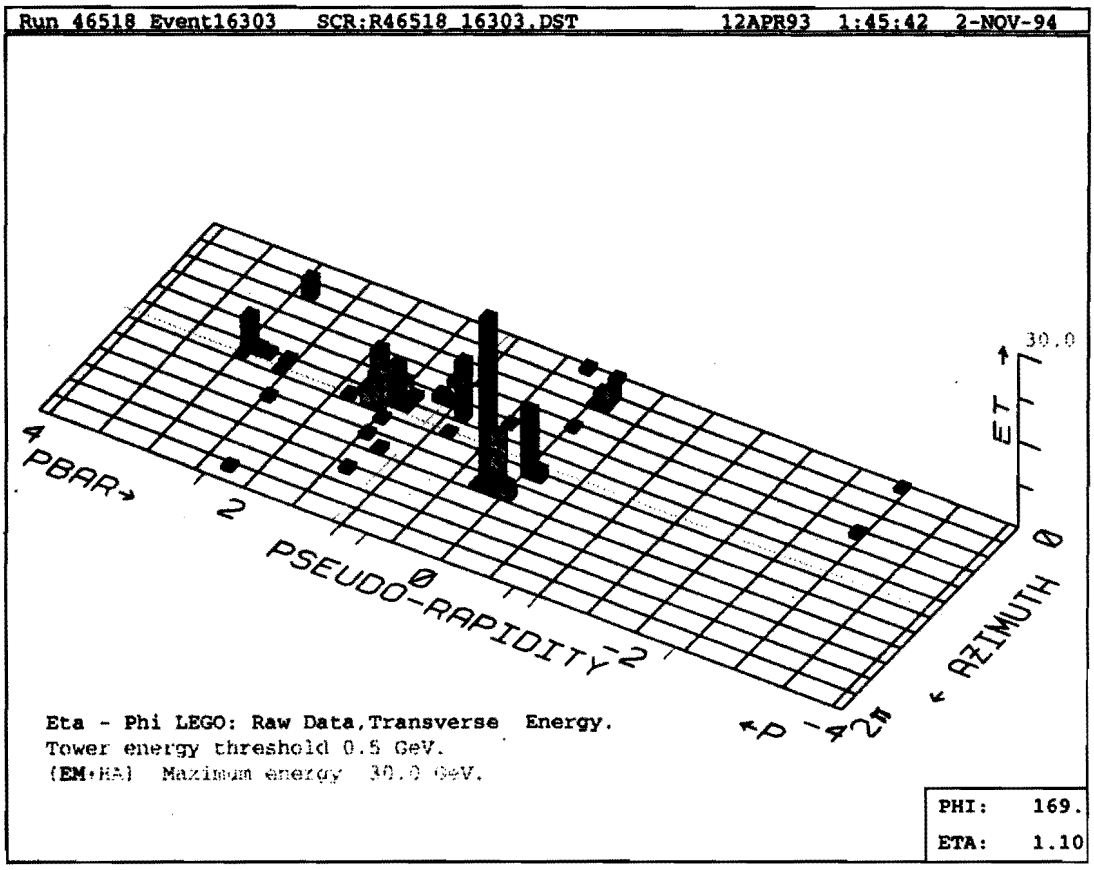

Figure 4.14: A calorimeter display of the ee candidate event.

CUT in following order	efficiency
Isolation cut	0.973±0.025
mass cut	0.944±0.026
$\not\!\!E_T > 20$ GeV	0.279±0.021
S > 2.4	0.814±0.046
W removal cut	0.350±0.033
$\Delta\phi(\not\!\!E_T$,jet) cut	0.934±0.065
$\Delta\phi(\not\!\!E_T$,l) cut	0.233±0.029
total	0.016±0.003

Table 4.6: Topology cut efficiencies for the $Z \rightarrow \tau\tau$ background.

The τ is then allowed to decay to an electron or a muon 80 times to accumulate statistics. From this sample we obtain reliable rejection factors for the topology cuts since the underlying event in the $Z \rightarrow \tau\tau$ sample remains the same as that in the $\gamma/Z^0 \rightarrow ee$ data events.

The efficiencies for event topology cuts are given in Table 4.6. We see that the W removal cut and the $\Delta\phi(\not\!\!E_T$,l) cut greatly reduce this background after the $\not\!\!E_T > 20$ GeV cut.

We also generated three samples using the ISAJET Monte Carlo, each with 30,000 events and a different value of the parameter QTW(0, 3 and 7) which controls the transverse momentum of the Z. These samples are used to get the efficiencies for the geometrical and kinematic requirement. We find that these efficiencies for different values of the parameter QTW are similar and the difference is within 3%. The efficiency for the geometrical and kinematic requirement is (7.5±0.4)%.

The lepton identification efficiency is measured to be 83% from the data and the trigger efficiency is about 85%. The $Z \rightarrow \tau\bar{\tau}$ cross section is set to the measured value for $Z \rightarrow ee$ of 209 pb [28] and the branching ratio for

$\tau\tau$ to dilepton(ee, $\mu\mu$ or $e\mu$) is $BR = (0.178\times2)^2 = 0.127$. The number of $Z \rightarrow \tau\tau \rightarrow$ dilepton events expected for 19.3 pb^{-1} luminosity is 0.43 $\pm$ 0.10. Although the uncertainty includes systematic uncertainties, it is dominated by the statistical uncertainty due to the limited number of $\gamma/Z^0 \rightarrow ee$ data events from which the $Z \rightarrow \tau\tau$ sample is made.

4.5.2 Drell-Yan

We use the observed $Z^0 \rightarrow ee$, and $Z^0 \rightarrow \mu\mu$ distributions to predict the background from the continuum. Our initial assumption is that the $P_T(\gamma/Z^0)$ distributions inside and outside the Z^0 region are similar. ISAJET predicts that there is a slight stiffening of the $P_T(\gamma,Z^0)$ with increasing mass, which could lead to an overestimate of the background.

The large $\not\!\!E_T$ in Z^0 events originates frequently from jet mismeasurement. In these cases the direction of the $\not\!\!E_T$ is along one of the jets. To obtain greater rejection against Drell-Yan events we require that the $\not\!\!E_T$ be more than 30° away from the closest jet. From Figure 4.8 (b), we can see that for events with more than 20 GeV $\not\!\!E_T$, most of them have $\Delta\phi_{\nu jet} < 30°$.

Table 4.7 lists the fractions of Z events passing various topology cuts in sequence. After all topology cuts, there are two events left (one ee and one $\mu\mu$) in the Z-region.

The scaling factor from the region inside of the Z window to outside of the Z window is obtained from the ISAJET Monte Carlo sample with only geometry and P_T cuts. The ISAJET cross section has been scaled to the Drell-Yan cross section measured in the 1988-89 data [36]. We get the scaling factors as follows:

N(12-70 GeV) : N(70-110 GeV) : N(110 GeV above) = 0.95 : 1 : 0.04,

	Cut	Number of Events	Fraction
a)	Z events	702	100%
b)	$\not\!\!E_T > 20$GeV	33	4.7%
c)	S > 2.4	18	2.6%
d)	W removal cut	9	1.3%
e)	$\Delta\phi(\not\!\!E_T$,jet) cut	4	0.6%
f)	$\Delta\phi(\not\!\!E_T$,l) cut	2	0.3%

Table 4.7: Topology cut rejections in Z events. Each line includes all previously listed cuts.

where the uncertainty is about 35% due to the cross section measurement.

The $\not\!\!E_T$ cut efficiencies are very different for Drell-Yan outside the Z mass window and inside the Z mass window. Therefore a correction factor for this efficiency is important. We study this effect by using the ISAJET Monte Carlo sample. In Figure 4.15, we plot the invariant mass and $\not\!\!E_T$ distributions for Drell-Yan events inside and outside the Z mass window. After the (9,6) dilepton P_T cut, the Drell-Yan outside the Z mass window is dominated by events with mass around 25 GeV(see Figure 4.15 (a)); there the jet activity is much lower than in high mass Drell-Yan events near the Z. We list the efficiencies of the $\not\!\!E_T$ cut (including b),c),e),f) cuts in Table 4.7) for different mass bins in Table 4.8. The correction factors we get from this ISAJET Monte Carlo are

$$\varepsilon(12\text{-}70) : \varepsilon(70\text{-}110) : \varepsilon(>110) = 0.11 : 1 : 2.4$$

where we expect small systematic uncertainties since they tend to cancel in the ratios.

When we scale the number of events from the region inside of the

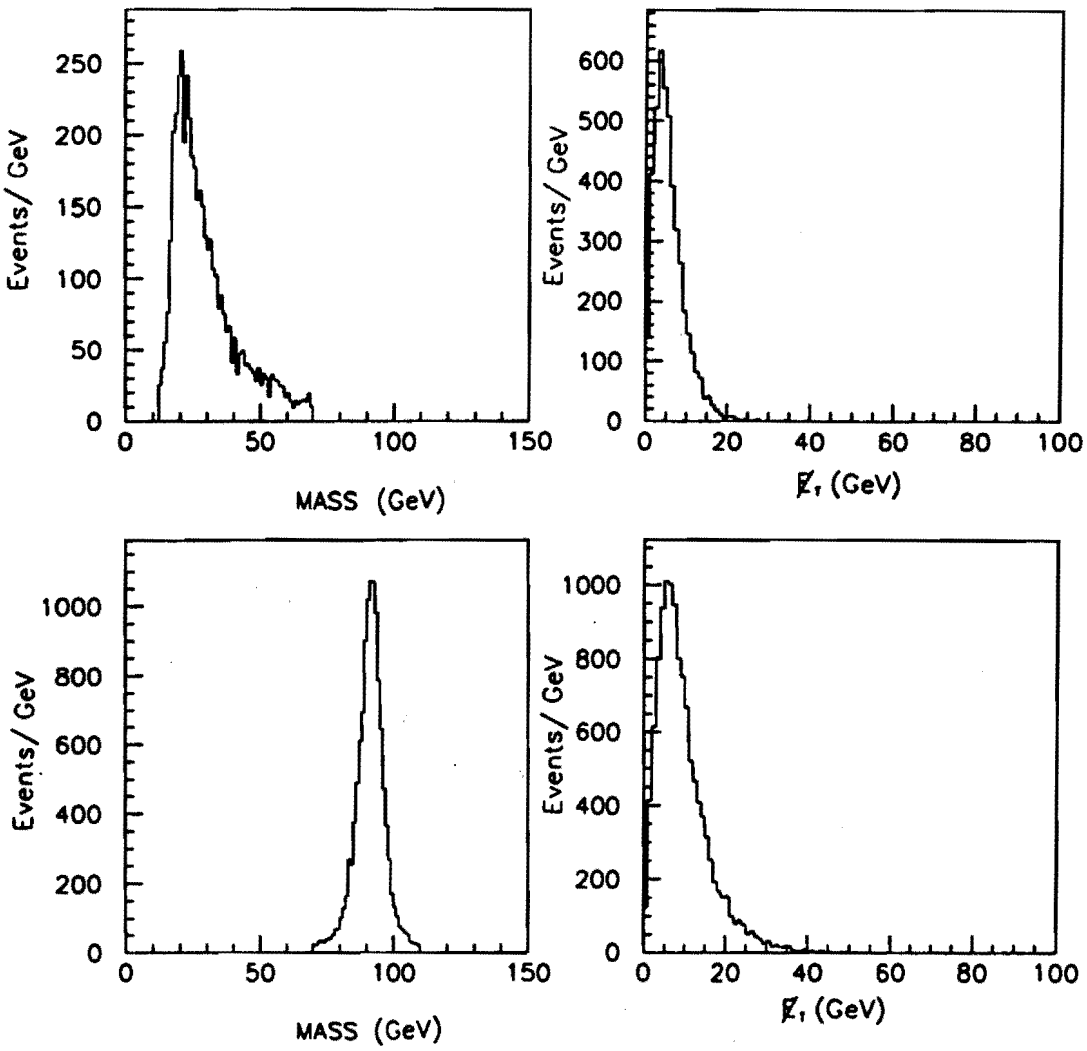

Figure 4.15: Invariant mass and $\not\!\!E_T$ distributions of the ISAJET Monte Carlo events for different Drell-Yan mass regions.
a) Invariant mass of low mass Drell-Yan(12-70 GeV)
b) $\not\!\!E_T$ of low mass Drell-Yan(12-70 GeV)
c) Invariant mass of Z for our cut(70-110 GeV)
d) $\not\!\!E_T$ of Z for our cut(70-110 GeV)

mass bin(GeV)	12–40	40–70	70–110	110 above
b),c),e),f) cuts in Table 4.7	0.0030	0.034	0.078	0.20

Table 4.8: $\not\!\!E_T$ cut efficiencies for different Drell-Yan mass bins from the ISAJET Monte Carlo.

Z window to the region outside of the Z window, we get the background expectation of 0.38 ± 0.27 events in the signal region.

4.5.3 $b\bar{b}$ or $c\bar{c}$

Heavy flavor backgrounds, mostly $b\bar{b}$, have been studied using the ISALEP [34] Monte Carlo to model the production processes, and the CLEO Monte Carlo [37] to model b-quark decay. A dilepton Monte Carlo sample is generated in which the P_T of both leptons must be more than 5 GeV/c. The events are generated using ISAJET with the internal loop turned on to speedup heavy quark production processes. With this technique, ISAJET attempts to simulate the next to leading order (NLO) $b\bar{b}$ production processes such as gluon splitting and flavor excitation, as well as the direct production of heavy flavor (b, c) quark-antiquark pairs. We keep events that have at least two b or c quarks with $P_T > 12$ GeV/c (this corresponds to keeping 90% of the events in which the daughter leptons have $P_T > 5$ GeV/c). Next, the event is passed through the CLEO Monte Carlo module, which redecays the B mesons in the event. This changes the average charged particle multiplicity and energy flow around the lepton to agree with measurements made in the CLEO experiment. After requiring two leptons in each event to have P_T greater than 5 GeV/c, we pass the events through a full detector simulation.

Cut in following order	efficiency(%)
Isolation cut	27.8±0.4
mass cut	82.0±0.5
$\not\!\!E_T > 20$ GeV	0.76±0.13
S > 2.4	57.6±8.6
W removal cut	94.7±5.1
$\Delta\phi(\not\!\!E_T$,jet) cut	61±11
$\Delta\phi(\not\!\!E_T$,l) cut	9.1±8.7
total	0.0053±0.0053

Table 4.9: Topology cut efficiencies for the $b\bar{b}$ background.

The efficiencies of the event topology cuts are listed in Table 4.9. Only 0.76% of the $b\bar{b}$ events pass the $\not\!\!E_T > 20$ GeV cut after the isolation and mass cuts have been made. As a test of the Monte Carlo modeling, we show in Figure 4.16 a comparison of the $\not\!\!E_T$ distribution of the $e\mu$ data in the region $M_{e\mu} < 5$ GeV/c^2, where b quark sequential decays dominate, with the $b\bar{b}$ Monte Carlo events.

To normalize the ISAJET predictions, the yield of the eμ data in the b quark sequential decay peak (Figure 4.3 (c)) is compared with the number of such events found in the Monte Carlo sample. By comparing 667 $e\mu$ data events (19.3 pb^{-1} integrated luminosity) and 2220 Monte Carlo events (37.5 pb^{-1} integrated luminosity with $\epsilon_{id}\cdot\epsilon_{trig} \sim 60\%$) with the (9,6) dilepton P_T selection, we obtain a normalization factor DATA/MC = 1.1±0.3. The 30% uncertainty is largely due to the uncertainty in the branching ratios of the b decay modes and the uncertainty in the identification efficiency of leptons from b quarks in the Monte Carlo. The number of background events from $b\bar{b}$ or $c\bar{c}$ sources to our analysis is estimated as 0.5 ± 0.5 events for a luminosity of 19.3 pb^{-1}.

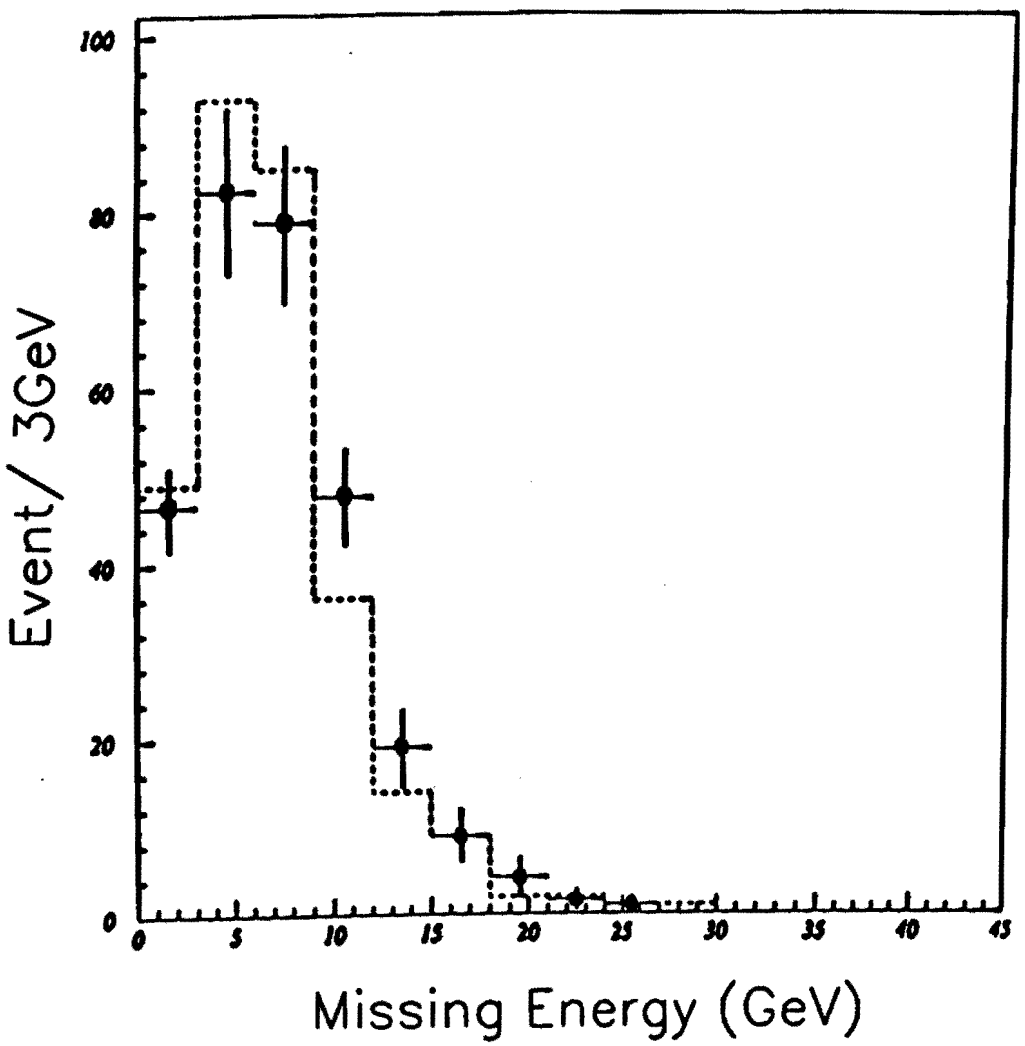

Figure 4.16: A comparison of the $\not\!\!E_T$ distributions of the $e\mu$ data (points) with the $b\bar{b}$ Monte Carlo events (histogram).

$\sigma \cdot BR$	$\epsilon_{\text{geom}\cdot P_T}$	ϵ_{event}	ϵ_{total}	Number(exp)
0.656	0.220	0.426	0.071	0.9±0.3

Table 4.10: Expectation for background from the $WW \rightarrow ll$ + X production for 19.3 pb^{-1}.

4.5.4 WW, WZ

The WW and WZ background samples are generated using the ISAJET Monte Carlo and then simulated with a full detector simulation and reconstructed. The W decay modes we use are $W \rightarrow e\nu$, $W \rightarrow \mu\nu$ and $W \rightarrow \tau\nu$ with τ decaying semileptonically. We generated 10,000 WW events which corresponds to an integrated luminosity of 9469 pb^{-1}. The cross-section for WW production is normalized to a total cross section of 9.5 pb, calculated with the structure functions HMRSB [38].

The dilepton topology in WW events is very similar to that of $t\bar{t}$ events. The summary of the cross section and cut efficiencies of the WW sample are shown in Table 4.10. For a luminosity of 19.3 pb^{-1} we expect 0.9±0.3 events from the WW background. The error is dominated by a theoretical uncertainty in the cross section of 30%. The contribution from WZ production is small and negligible.

4.5.5 W + jet

Events from the W + jet process, with the jet misidentified as a lepton (lepton misidentification), can mimic the $t\bar{t}$ signature. Backgrounds from lepton misidentification are estimated by measuring the probabilities for tracks or calorimeter energy clusters from a jet sample, collected with a 20

GeV (transverse energy) threshold jet trigger, to satisfy muon or electron identification cuts. The electron misidentification probability is about 0.7% and the muon misidentification probability is 1% for a generic jet. The lepton misidentification probabilities are then applied to the number of W + jet events in the data. The W + jet events are selected by requiring an isolated high P_T lepton ($P_T > 25$ GeV/c and $E_{iso} < 2$ GeV), large $\not\!\!E_T$ ($\not\!\!E_T > 20$ GeV). and an additional track or cluster. There are 158 events in the W + jet sample. The characteristic drop at M_W is seen in the distribution of the transverse mass formed from the $\not\!\!E_T$ and the transverse momentum of the high P_T lepton (Figure 4.17). To remove these events, we use the fact that in W events the lepton and the $\not\!\!E_T$ tend to be back-to-back in the transverse plane, as shown in the scatter plot of $\Delta\phi(\not\!\!E_T$,high P_T lepton) vs P_T of the high P_T lepton (in Figure 4.7 (b)), while the $\Delta\phi(\not\!\!E_T$,high P_T lepton) distribution of the signal is less back-to-back (shown in Figure 4.7 (a)). The W + jet background is estimated as 0.8±0.7 events. The error is mainly due to the limited statistics in the number of W + jet events which survive the event topology cuts and the systematic uncertainty in the lepton misidentification probabilities.

4.5.6 Background Summary

The background estimates are summarized in Table 4.11. In total, 3.0 ± 1.0 background events are expected in this analysis.

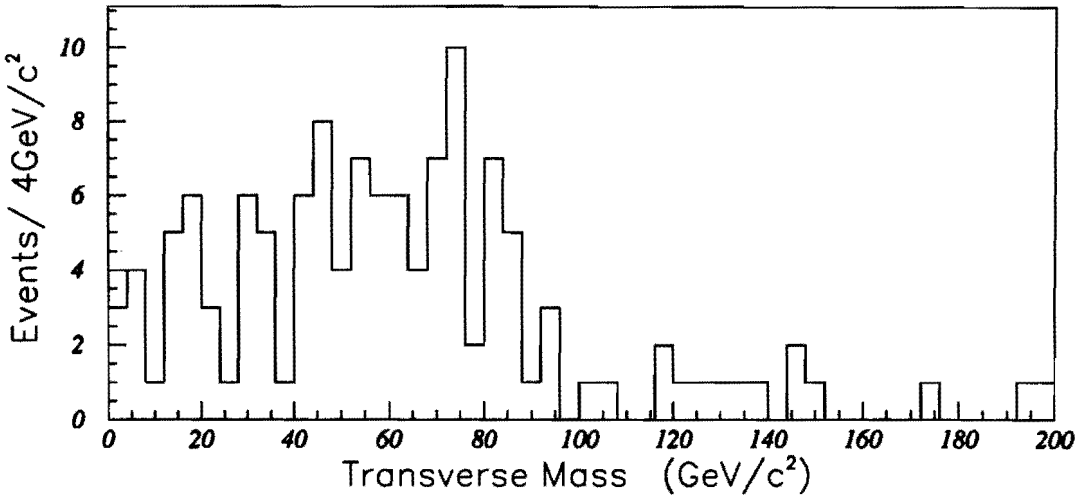

Figure 4.17: Distribution of the transverse mass formed from the $\not\!\!E_T$ and the transverse momentum of the high P_T lepton in the W + jet data sample.

Background	Events Expected
WW	0.9 ± 0.3
$Z \rightarrow \tau\tau$	0.43 ± 0.10
$b\bar{b}$	0.5 ± 0.5
Drell-Yan	0.4 ± 0.3
W + jet	0.8 ± 0.7
Total	3.0 ± 1.0

Table 4.11: Number of background events expected in 19.3 pb^{-1}

Chapter 5

The $t\bar{t}$ Production Cross Section

The $t\bar{t}$ production cross section can be written as :

$$\sigma_{t\bar{t}} = \frac{N_{obs}}{\mathcal{L} \cdot BR \cdot \epsilon_{total}} \tag{5.1}$$

where N_{obs} is the background subtracted number of observed events, $\mathcal{L}$ is the integrated luminosity of the data sample, and $BR \cdot \epsilon_{total}$ is the efficiency for observing $t\bar{t}$ events in the selected channel (dilepton channel in this analysis). In a data sample of 19.3 pb^{-1}, we observe 2 events with a background estimation of 3.0$\pm$1.0 events. The term $BR \cdot \epsilon_{total}$ for various M_t, M_H combinations are summarized in Tables 5.1, 5.2, 5.3, 5.4 and 5.5, while for each process (HH, HW or WW), 100% branching ratio of $t\bar{t}$ decay to that process is assumed for convenience of calculation.

M_{top}	110 GeV									
M_{Higgs}	-	45 GeV		65 GeV		80 GeV		95 GeV		105 GeV	
TYPE	WW	HH	HW	HH	HW	HH	HW	HH	HW	HH	HW
$BR{\cdot}\varepsilon_{total}(\%)$	0.54	0.31	0.39	0.47	0.54	0.57	0.55	0.66	0.59	0.71	0.59

Table 5.1: $BR{\cdot}\varepsilon_{total}$ expected for $M_{top} = 110$ GeV.

M_{top}	105 GeV									
M_{Higgs}	-	45 GeV		55 GeV		65 GeV		80 GeV		95 GeV	
TYPE	WW	HH	HW	HH	HW	HH	HW	HH	HW	HH	HW
$BR{\cdot}\varepsilon_{total}(\%)$	0.59	0.35	0.47	0.42	0.45	0.52	0.54	0.62	0.55	0.65	0.55

Table 5.2: $BR{\cdot}\varepsilon_{total}$ expected for $M_{top} = 105$ GeV.

M_{top}	100 GeV									
M_{Higgs}	-	45 GeV		55 GeV		65 GeV		80 GeV		95 GeV	
TYPE	WW	HH	HW	HH	HW	HH	HW	HH	HW	HH	HW
$BR{\cdot}\varepsilon_{total}(\%)$	0.51	0.31	0.44	0.43	0.50	0.49	0.52	0.57	0.55	0.59	0.58

Table 5.3: $BR{\cdot}\varepsilon_{total}$ expected for $M_{top} = 100$ GeV.

M_{top}	95 GeV									
M_{Higgs}	-	45 GeV		55 GeV		65 GeV		80 GeV		90 GeV	
TYPE	WW	HH	HW	HH	HW	HH	HW	HH	HW	HH	HW
$BR{\cdot}\varepsilon_{total}(\%)$	0.52	0.31	0.41	0.36	0.47	0.40	0.44	0.56	0.52	0.53	0.58

Table 5.4: $BR{\cdot}\varepsilon_{total}$ expected for $M_{top} = 95$ GeV.

M_{top}	90 GeV									
M_{Higgs}	-	45 GeV		55 GeV		65 GeV		80 GeV		85 GeV	
TYPE	WW	HH	HW	HH	HW	HH	HW	HH	HW	HH	HW
$BR{\cdot}\varepsilon_{total}(\%)$	0.47	0.27	0.37	0.36	0.42	0.42	0.45	0.48	0.45	0.55	0.53

Table 5.5: $BR{\cdot}\varepsilon_{total}$ expected for $M_{top} = 90$ GeV.

5.1 Systematic Uncertainties

The systematic uncertainty on the cross section measurement comes mainly from the limited knowledge of the integrated luminosity ($\mathcal{L}$) and of the total detection efficiency (ε_{total}) for the $t\bar{t}\rightarrow ll$ + X events.

5.1.1 Uncertainty in Luminosity

The integrated luminosity was measured using the beam-beam counters (Section 2.2.4). The portion of the inelastic $\bar{p}p$ cross section accepted by the beam-beam counters is about 74%. The data for the total cross section measurement were collected in short dedicated runs during the 1988-89 physics run of the Fermilab Tevatron Collider at center of mass energies of 546 and 1800 GeV. At each energy, the machine optics was specially tuned to enable detection of low four-momentum transfer elastic scattering events. The elastic scattering, diffractive scattering, and inelastic scattering rates were measured simultaneously. This way, the total cross section could be measured independent of the machine luminosity. The BBC cross section was measured to be 51.2 $\pm$ 1.7 mb. For our data sample, the total integrated luminosity is 19.3 pb^{-1} with a total uncertainty of 3.6%.

5.1.2 Uncertainty in the Total Detection Efficiency

The uncertainty in the total detection efficiency comes largely from the modeling of gluon radiation, the branching ratio of leptons from b decays, the detector simulation, identification efficiency, and limited Monte Carlo statistics.

One source of systematic uncertainty is the modeling of initial state radiation. Initial state radiation affects the motion of the $t\bar{t}$ system and hence the rapidity and transverse momentum distributions of the top quark decay products. Also, the modeling of gluon radiation affects the isolation properties of the leptons, and hence their topology cut efficiency. This effect can be studied by turning on and off gluon radiation in ISAJET, and taking half the difference in the corresponding efficiencies as an estimate of the systematic uncertainty. The uncertainty in the efficiency due to the modeling of gluon radiation is 8%. Since we have about 30% of dilepton events from the boson-b contribution, the world average branching ratio of the b decay modes which has a 30% systematic uncertainty yields a 9% total uncertainty to our dilepton acceptance. The uncertainty in the identification efficiency is 6%. Detector simulation also affects lepton identification. We take half of the difference between the result obtained from two different detector simulations as the uncertainty (5%). The Monte Carlo statistical error is about 6%.

5.1.3 Total Systematic Uncertainty

The overall uncertainties are listed in Table 5.6. These uncertainties are essentially independent of top mass or Higgs mass. The sum in quadrature of all the uncertainties is 16%.

Systematic uncertainty	
Modeling of Gluon Radiation	8%
Branching ratio of b decay	9%
Trigger Efficiency	2%
Identification Efficiency	6%
Detector simulation	5%
Integrated Luminosity	4%
Monte Carlo Statistics	6%
Total	16%

Table 5.6: The overall systematic uncertainties in $t\bar{t}$ cross section measurement.

5.2 Limits on $t\bar{t}$ Production Cross Section

We now have all the information needed for equation 5.1. Given 2 events observed and 3.0±1.0 events expected from the backgrounds, we have found no evidence for $t\bar{t}$ production in which the top decays to a charged Higgs boson. A 95% confidence level upper limit on the number of expected signal events ($N_{t\bar{t}}(95\%CL)$) is calculated using the distribution obtained by convoluting a Poisson statistical distribution with a Gaussian distribution [39] describing the total systematic uncertainty (see Appendix A). To remain independent of the uncertainties in the background estimation, the number of background events is not subtracted. This produces a conservative limit. With 16% total systematic uncertainty and no background subtraction, $N_{t\bar{t}}(95\%CL)$ = 6.68 for 2 observed events. If the background estimate had been subtracted, $N_{t\bar{t}}(95\%CL)$ would have been 4.93.

This upper limit on the number of events, the total detection efficiency as a function of M_t, M_H, and BR($H\rightarrow\tau\nu$) can be converted into an upper limit on the $t\bar{t}$ production cross section with the use of equation 5.1 as

follows:

$$\sigma_{t\bar{t}}(95\%CL) = \frac{N_{t\bar{t}}(95\%CL)}{\mathcal{L}\cdot BR\cdot\varepsilon_{total}}\ , \tag{5.2}$$

In two-Higgs-doublet models, the term $BR\cdot\varepsilon_{total}$ for a fixed tanβ can be written as:

$BR\cdot\varepsilon_{total} =$

$$BR_{t\bar{t}\to HbHb}\cdot(BR_{H\to\tau\nu})^2\cdot\varepsilon_{HH} + BR_{t\bar{t}\to HbWb}\cdot BR_{H\to\tau\nu}\cdot\varepsilon_{HW} + BR_{t\bar{t}\to WbWb}\cdot\varepsilon_{WW} \tag{5.3}$$

where ε_{HH}, ε_{HW} and ε_{WW} are the total detection efficiencies expected for the HH, HW and WW processes in the ISAJET Monte Carlo, and include the branching ratios for W and τ into leptons. In Table 5.7, we list the measured upper limits on $\sigma_{t\bar{t}}$ at 95% CL for different tanβ values. For comparison, we also list the theoretical lower limits for $\sigma_{t\bar{t}}$ [40] (one sigma below the mean theoretical $\sigma_{t\bar{t}}$) for different top masses in Table 5.7.

5.3 Limits on the Top Mass and the Charged Higgs Mass

Comparing our 95% upper limit of the $t\bar{t}$ cross section with the lower limit of the theoretical prediction for $\sigma_{t\bar{t}}$ [40], we can exclude regions of the (M_t,M_H) plane at 95% confidence level for a given $BR(t\to Hb)$ and $BR(H\to\tau\nu)$. From Table 5.7, we can derive the curve of the 95% confidence level limit in the (M_t,M_H) plane for the two-Higgs-doublet models. The limits in the (M_t,M_H) plane are shown in Figure 5.1 for two tanβ values where $BR(t\to Hb)$ is relatively high. Figure 5.2 shows the excluded region with assumptions of $BR(t\to Hb) = 1.0$ (top quark only decays to Hb) and $BR(H\to\tau\nu)$

$\tan\beta$	M_{top} (GeV)	M_{Higgs} (GeV)						$\sigma_{t\bar{t}}$(theory) (pb)
		45	55	65	80	95	105	
		Cross section limit $\sigma_{t\bar{t}}$ in pb (95% CL)						
100	110	122	95.5	81.7	69.8	62.0	61.3	52.7
	105	108	94.5	76.1	65.0	63.4		67.3
	100	122	91.3	80.9	70.0	65.9		86.3
	95	124	106	97.4	71.3			112
	90	145	109	93.5	83.0			148
15	110	76.2	69.6	66.4	65.4	64.3	64.4	52.7
	105	67.3	67.3	62.2	60.8	59.9		67.3
	100	75.8	70.0	68.3	66.2	65.2		86.3
	95	81.5	74.6	74.3	68.5			112
	90	94.0	83.8	78.9	76.3			148
5	110	67.8	65.9	65.0	64.8	64.4	64.5	52.7
	105	61.2	62.3	59.8	59.4	59.2		67.3
	100	68.0	66.5	66.1	65.5	65.2		86.3
	95	71.1	69.2	69.2	67.7			112
	90	79.2	76.5	75.2	74.6			148
2	110	76.0	70.8	68.1	66.8	65.3	64.8	52.7
	105	67.6	67.3	63.3	61.7	60.3		67.3
	100	75.0	71.0	69.5	67.4	65.8		86.3
	95	79.4	74.7	74.2	69.6			112
	90	89.9	83.5	79.9	77.0			148
1.5	110	89.6	80.9	75.9	72.4	68.5	66.2	52.7
	105	79.4	78.0	70.9	67.1	63.0		67.3
	100	88.6	81.3	77.9	72.6	67.5		86.3
	95	95.1	86.6	84.2	74.8			112
	90	110	98.6	91.1	82.8			148
1	110	163	140	124	106	87.6	73.6	52.7
	105	146	136	116	97.4	77.0		67.3
	100	166	144	128	104	77.1		86.3
	95	186	158	141	106			112
	90	232	191	160	115			148

Table 5.7: Measured upper limits on the cross section, $\sigma_{t\bar{t}}$, in pb at 95% CL for a given top mass and Higgs mass combination with several $\tan\beta$ values. The last column lists the lower limits (at one sigma) of the theoretical $\sigma_{t\bar{t}}$ for different top masses [40].

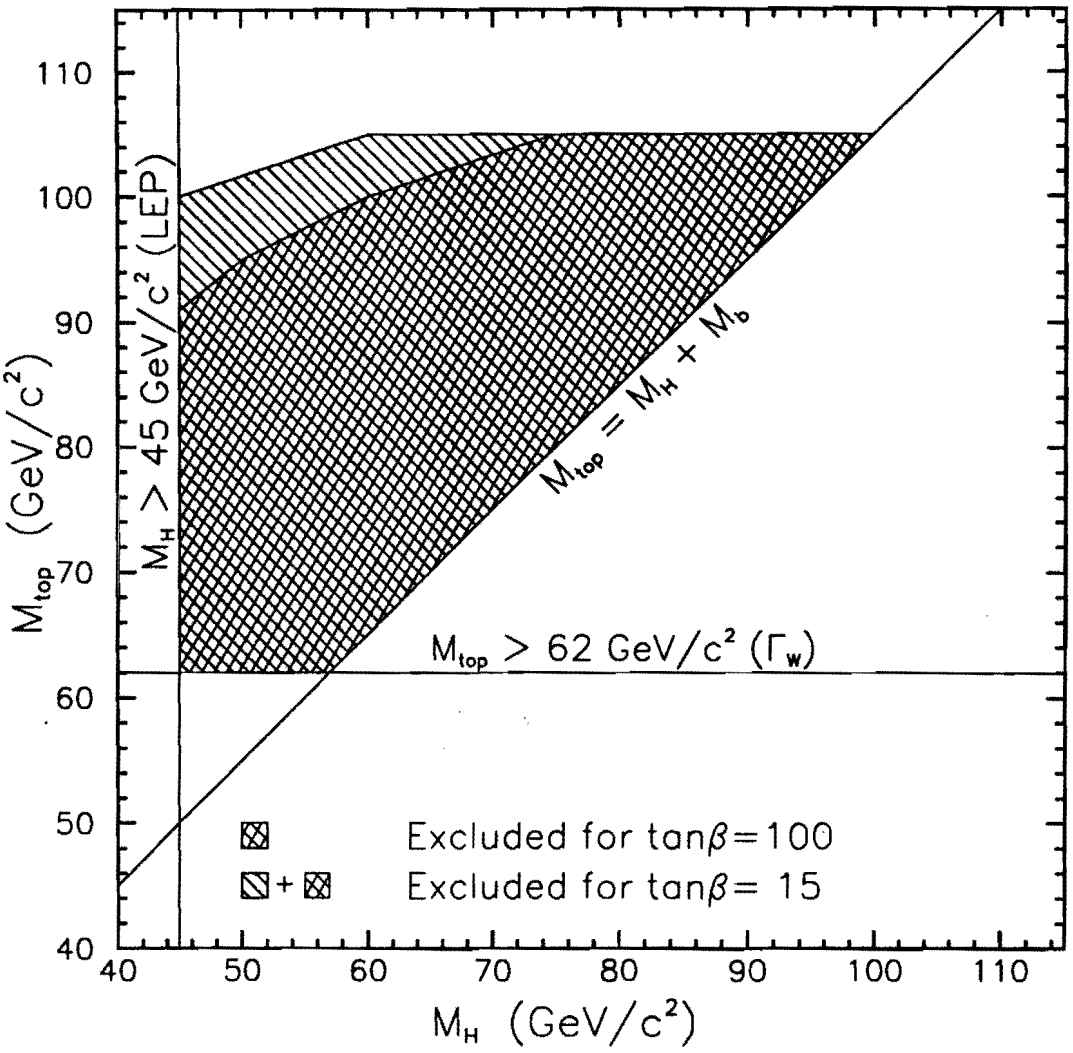

Figure 5.1: Regions of the (M_t, M_H) plane excluded at 95% CL for the two-Higgs-doublet models. Top mass below 62 GeV/c^2 is excluded from the W lifetime (W width) measurement at CDF [7]. Charged Higgs mass below 45 GeV/c^2 is excluded from direct searches in Z decays at LEP [11]. We assume $M_H < M_t - M_b$ in this search.

= 0.5, 0.75 and 1.0. For the case $M_t < M_W + M_b$, the entire (M_t,M_H) plane is excluded when the $BR(t \rightarrow Hb) = 1.0$ and $BR(H \rightarrow \tau\nu) > 75\%$.

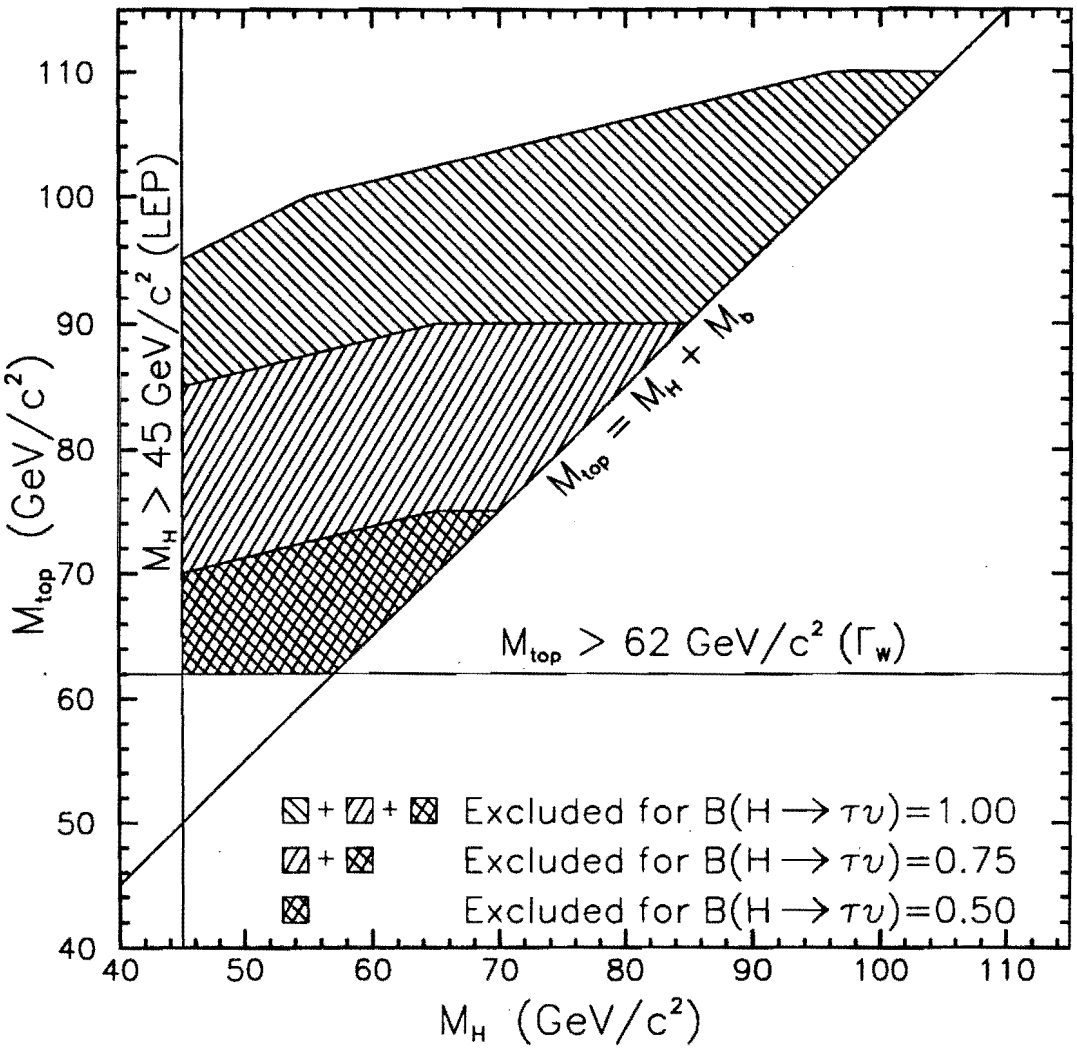

Figure 5.2: Regions of the (M_t, M_H) plane excluded at 95% CL for the branching ratio $BR(t \rightarrow Hb) = 1.0$.

Chapter 6

Conclusions and Outlook

We have searched for the decay $t \to Hb$ as well as $t \to Wb$ in the dilepton channel. No evidence for the top quark has been observed and this analysis excludes top quarks in the mass range below the W mass at the 95% confidence level for a large branching ratio of $H \to \tau\nu$ ($BR(H \to \tau\nu) > 75\%$), or for $\tan\beta > 1.5$ in two-Higgs-doublet models.

For a small branching ratio of $H \to \tau\nu$ ($BR(H \to \tau\nu) < 50\%$) or $\tan\beta < 1$ in two-Higgs-doublet models, this analysis has limited sensitivity because the dominant decay mode of the charged Higgs boson is $H \to c\bar{s}$. In this case, $t\bar{t}$ events would produce 6-jet final states, for which there is a large QCD background.

Given the negative result of this search and recent publication from CDF of evidence for top quark production with a top mass of 174 GeV/c^2 in the search of the Standard Model top decays, it is natural to ask what the prospects are for the discovery of $t \to Hb$ in the future. In fact, global fits to precision electroweak measurements from LEP also yield a favored top mass of 177^{+11+18}_{-11-19} GeV/c^2 [42]. For the top quark heavier than the W, the most

unambiguous ways to discover or to rule out the presence of a charged Higgs in top quark decays are the precise measurements of the branching ratio of the top quark decay into Wb or the ratio of the branching ratios of the top quark decays into electron (or muon) and into τ.

In a charged Higgs scenario, the branching ratios of top quark decays can be written as:

$$BR(t\rightarrow e\nu b) = BR(t\rightarrow \mu\nu b) = BR(t\rightarrow Wb) \times 1/9 \qquad (6.1)$$

and

$$BR(t\rightarrow \tau\nu b) = BR(t\rightarrow Wb) \times 1/9 + BR(t\rightarrow Hb) \times BR(H\rightarrow \tau\nu). \qquad (6.2)$$

We can see that the presence of the charged Higgs always increases the $t\rightarrow\tau\nu b$ branching ratio, compared to the branching ratio of $t\rightarrow e\nu b$ or $t\rightarrow\mu\nu b$. The effect of the charged Higgs is then to induce lepton universality violation in top quark decays by enhancing the $t\rightarrow\tau\nu b$ over the $t\rightarrow e\nu b$ and $t\rightarrow\mu\nu b$ modes. The degree of lepton universality violation induced by a charged Higgs in top quark decays can be quantified by the ratio

$$R_{\tau l}(l = e \text{ or } \mu) = \frac{BR(t\rightarrow\tau\nu b)}{BR(t\rightarrow l\nu b)} = 1 + \frac{BR(t\rightarrow Hb)BR(H\rightarrow\tau\nu)}{BR(t\rightarrow Wb)BR(W \rightarrow \tau\nu)}, \qquad (6.3)$$

where $BR(W \rightarrow \tau\nu) = BR(W\rightarrow e\nu) = BR(W \rightarrow \mu\nu) = 1/9$. In Figure 6.1 the ratio $R_{\tau l}$ is shown as a function of $\tan\beta$ for $M_H = 50$, 100 and 150 GeV/c^2 with $M_t = 174$ GeV/c^2. If a ratio $R_{\tau l}$ larger than 1 is measured, it could be evidence of a charged Higgs in top quark decays, with the charged Higgs decaying predominantly into $\tau\nu$.

To do precision measurements of the top quark branching ratios requires a large number of top quark events. Therefore, these measurements can be one of the tasks of the experiments at the Tevatron with the Main

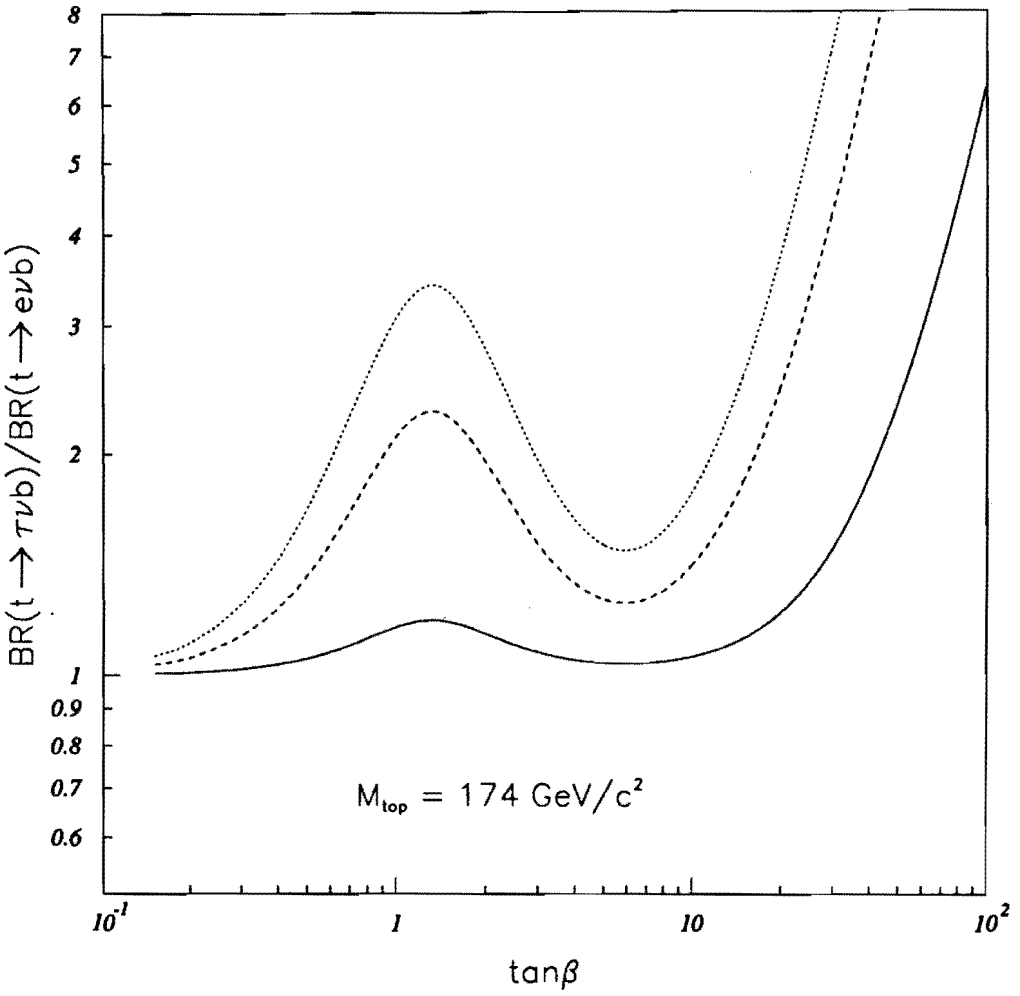

Figure 6.1: The ratio $BR(t \to \tau\nu b)/\ BR(t \to l\nu b)$ (l = e or μ) as a function of tanβ for M_H = 50 (dotted line), 100 (dashed line) and 150 (solid line) GeV/c^2 with M_t = 174 GeV/c^2.

Injector upgrade or the LHC, which may achieve integrated luminosities of 1(Tevatron)-10(LHC) fb^{-1} for a year's run time. In these experiments, the ratio $R_{\tau l}$ can be measured by comparing the number of events in the $e\mu b$ channel (high P_T $e\mu$ event with a tagged b jet), $N_{e\mu b}$, with those in the $l\tau b$ ($l = e$ or μ) channel, $N_{l\tau b}$, where τ is identified by a one prong or three prong isolated high P_T hadronic jet.

The ratio $N_{l\tau b}/N_{e\mu b}$ is directly related to the quantity $R_{\tau l}$

$$\frac{N_{l\tau b}}{N_{e\mu b}} = (\frac{\varepsilon_{W\to\tau}}{\varepsilon_{W\to l}} + \frac{\varepsilon_{H\to\tau}}{\varepsilon_{W\to l}}(R_{\tau l} - 1))BR(\tau\to hadrons). \tag{6.4}$$

Here $BR(\tau\to hadrons) = 0.64$ [39], $\varepsilon_{W\to l}$ ($l = e$ or μ) is the probability (acceptance and efficiency) of identifying the $t\to Wb\to l\nu b$ decay, and $\varepsilon_{W\to\tau}$ and $\varepsilon_{H\to\tau}$ are the probabilities (acceptance and efficiency) of identifying the $\tau\to hadrons$ decay in events in which the τ comes from the decay of $t\to Wb$ with $W\to\tau\nu$ and from the decay of $t\to Hb$ with $H\to\tau\nu$ respectively.

This method has limited sensitivity in the low $\tan\beta$ region ($\tan\beta < 0.4$) when the charged Higgs decays predominantly into $c\bar{s}$. The other way to discover or to rule out the top to a charged Higgs decay mode is to measure the branching ratio $BR(t\to Wb)$ precisely, regardless of the charged Higgs decay. This can be done by comparing the number of events in the llb channel (high P_T dilepton event with a tagged b jet), N_{llb}, with those in the lb ($l = e$ or μ) channel, N_{lb}, where the lepton P_T is required to be high enough that leptons from τ decays can be neglected.

The ratio N_{llb}/N_{lb} ($l = e$ or μ) is directly related to the branching ratio $BR(t\to Wb)$:

$$\frac{N_{llb}}{N_{lb}} = \frac{BR(t\to Wb)BR(W\to l\nu)\varepsilon_{t\to Wb\to l\nu}}{2 - BR(t\to Wb)BR(W\to l\nu)} \tag{6.5}$$

$$= \frac{2}{9}\times\frac{BR(t\to Wb)\varepsilon_{t\to Wb\to l\nu}}{2 - 2/9\cdot BR(t\to Wb)} \tag{6.6}$$

where $\varepsilon_{t\to Wb\to l\nu}$ is the total detection efficiency for a lepton from $t\to Wb\to l\nu$. Since many theoretical and experimental systematic uncertainties cancel in measuring this ratio, the branching ratio $BR(t\to Wb)$ can be measured very precisely.

The branching ratio $BR(t\to Wb)$ is shown in Figure 6.2 as a function of $\tan\beta$ for M_H = 50, 100 and 150 GeV/c^2 with M_t = 174 GeV/c^2. For M_H = 100 GeV/c^2 we can see this method has good sensitivity in the range $\tan\beta < 2$ or $\tan\beta > 20$; it has limited sensitivity in the range $2 < \tan\beta < 20$, where $BR(t\to Wb)$ is close to 100% no matter what the charge Higgs mass is. Note that this method is sensitive to the low $\tan\beta$ region. Thus it complements the previous method.

In the 1992-93 collider run, CDF observed 2 high P_T ($P_T > 20$ GeV/c) $e\mu$ events with one of them having a tagged b jet in the event. Combining the two methods discussed above and with an integrated luminosity of 10 fb^{-1} (assuming 1 year of running at luminosity of $10^{33}\text{cm}^{-2}\text{s}^{-1}$) at LHC, a large region of the M_t, M_H and $\tan\beta$ parameter space can be explored, for example the entire region of $\tan\beta$ if $M_H \leq 100$ GeV/c^2 and M_t = 174 GeV/c^2.

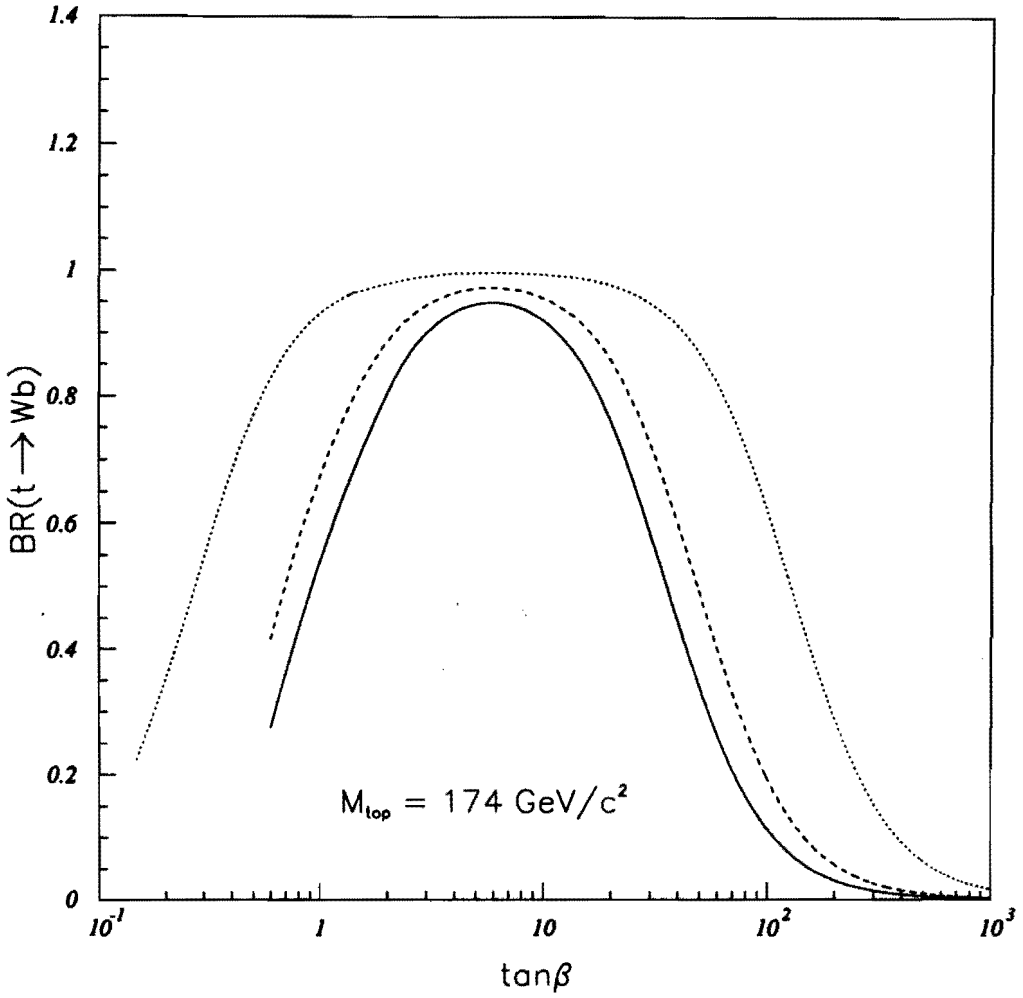

Figure 6.2: The branching ratio $BR(t \rightarrow Wb)$ as a function of $\tan\beta$ for M_H = 50 (solid line), 100 (dashed line) and 150 (dotted line) GeV/c^2 with M_t = 174 GeV/c^2.

Appendix A

Calculation of Upper Limits on Poisson Processes

In this appendix we briefly present and justify the equations we used to calculate upper limits on the $t\bar{t}$ production cross section. Our method is a slight extension of the procedure described in detail in reference [41] and summarized in the Review of Particle Properties by the Particle Data Group in reference [39]. In section A.1 we describe the calculation of upper limits in the simplest case, namely when there are no backgrounds and no systematic uncertainties. Next we consider the effect of systematic uncertainties in section A.2, and in the final section we incorporate the effect of the background subtraction A.3.

A.1 Upper Limits without Background or Systematic Uncertainties

Suppose we measure the rate of some process, and observe n_0 events. The 95% confidence level upper limit N on the Poisson parameter μ_S for this process is defined to be that value of μ_S for which it would be exactly 95% probable that a random measurement of the rate would yield greater than n_0 events. Hence this upper limit N is the solution of:

$$\mathrm{CL} = \sum_{n=n_0+1}^{\infty} \frac{e^{-N}N^n}{n!} \tag{A.1}$$

where CL is the desired confidence level. Equivalently:

$$1 - \mathrm{CL} = \sum_{n=0}^{n_0} \frac{e^{-N}N^n}{n!} \tag{A.2}$$

For $n_0 = 2$, the 95% CL upper limit N will be the mean of the Poisson distribution giving 5% as the probability for observing 0 or 1 or 2 events. This means solving for N in the equation :

$$P_N(0) + P_N(1) + P_N(2) = e^{-N} + Ne^{-N} + N^2e^{-N}/2 = 0.05\ . \tag{A.3}$$

The solution is $N = 6.30$ for $n_0 = 2$, ignoring systematic errors.

A.2 Upper Limits with Systematic Uncertainties

Systematic uncertainties are incorporated with the help of Gaussian smearing functions. Assume that the expected mean of a Poisson distribution ξ is known with a Gaussian probability distribution with mean u and standard

deviation equal to the total systematic uncertainty σ :

$$G_{u,\sigma}(\xi) = Ce^{\frac{-(\xi-u)^2}{2\sigma^2}} \tag{A.4}$$

Here, $G_{u,\sigma}(\xi)$ is the probability for the average of the underlying Poisson to be between ξ and $\xi + d\xi$. The normalization $C = C(\sigma)$ is chosen so that $\int_0^\infty G_{u,\sigma}(\xi)d\xi = 1$, that is, the Gaussian has been truncated not to allow negative numbers of events. The new distribution is then the convolution of the Poisson and the Gaussian :

$$\mathcal{P}_u(n,\sigma) = \int_0^\infty P_\xi(n)G_{u,\sigma}(\xi)d\xi \ . \tag{A.5}$$

Then the 95% CL upper limit on the number for $n_0 = 2$ is determined for a given value of σ by solving for N in the equation :

$$\mathcal{P}_N(0,\sigma) + \mathcal{P}_N(1,\sigma) + \mathcal{P}_N(2,\sigma) = 0.05 \ . \tag{A.6}$$

For a systematic uncertainty of $\sigma = 16\%$, we find the 95% CL upper limit $N = 6.68$ for $n_0 = 2$.

A.3 Upper Limits with Background and Systematic Uncertainties

When backgrounds are present, the definition of the upper limit must be modified to incorporate our knowledge of the fact that the actual number of events resulting from background, n_B, must be smaller than or equal to the observed number of events n_0. Let μ_B be the expectation value for the sum of all backgrounds. The probability for observing n_B background events, given the constraint $n_B \leq n_0$, is simply the Poisson probability renormalized to the

allowed range of n_B:

$$P'(n_B;\mu_B) = \frac{e^{-\mu_B}\mu_B^{n_B}}{n_B!} \Big/ \sum_{n=0}^{n_0} \frac{e^{-\mu_B}\mu_B^{n}}{n!} \tag{A.7}$$

On the other hand, the probability for observing n_S signal events is still:

$$P(n_S;\mu_S) = \frac{e^{-\mu_S}\mu_S^{n_S}}{n_S!} \tag{A.8}$$

Hence the probability for observing a total of $n = n_B + n_S$ events, with the constraint $n_B \leq n_0$, is given by:

$$P^{\star}(n;\mu_B,\mu_S) = \sum_{n_B=0}^{\min(n,n_0)} P'(n_B;\mu_B)\, P(n-n_B;\mu_S) \tag{A.9}$$

Note that, because of the normalization (A.7), $P^{\star}(n;\mu_B,\mu_S)$ is different from the joint probability for observing $n_B \leq n_0$ background events and $n - n_B$ signal events. On the other hand, this normalization ensures that the following relation is satisfied:

$$\sum_{n=0}^{\infty} P^{\star}(n;\mu_B,\mu_S) \;=\; 1.0 \tag{A.10}$$

The 95% confidence level upper limit N on μ_S is now defined as that value of μ_S for which it would be 95% probable that a random repeat of the same experiment would yield greater than n_0 events, given that the number of background events is restricted to be less than or equal to n_0. This upper limit N satisfies the equation:

$$1 - \mathrm{CL} \;=\; \sum_{n=0}^{n_0} P^{\star}(n;\mu_B,N) \tag{A.11}$$

$$\;=\; \sum_{n=0}^{n_0} \frac{e^{-(\mu_B+N)}(\mu_B+N)^n}{n!} \Big/ \sum_{n=0}^{n_0} \frac{e^{-\mu_B}\mu_B^{n}}{n!} \tag{A.12}$$

This formalism yields "background subtracted" upper limits. It is applicable even when the expectation value for the background is larger than the observed

number of events, since it takes background fluctuations properly into account. For $\mu_B = 0$ one recovers the usual equation without background subtraction.

Now we incorporate the systematic uncertainties in the expected signal and the background. Let σ_B be the uncertainty on the expected background μ_B, σ_S the fractional uncertainty on the expected signal μ_S, and define:

$$G(x;\mu,\sigma) = A(\mu,\sigma)\, e^{\frac{-(x-\mu)^2}{2\sigma^2}}, \tag{A.13}$$

where A is a normalization factor which satisfies:

$$A(\mu,\sigma) \int_0^\infty G(x;\mu,\sigma)\, dx \;=\; 1.0. \tag{A.14}$$

It is important to realize that this normalization condition defines A as a function of μ and σ. Upper limits are obtained by solving the following equation for N:

$$1 - \mathrm{CL} = \frac{\int_0^\infty dx\, G(x;\mu_B,\sigma_B) \int_0^\infty dy\, G(y;N,N\sigma_S) \sum_{n=0}^{n_0} \frac{e^{-(x+y)}(x+y)^n}{n!}}{\int_0^\infty dx\, G(x;\mu_B,\sigma_B) \sum_{n=0}^{n_0} \frac{e^{-x}x^n}{n!}} \tag{A.15}$$

We have assumed that uncertainties on signal and background are uncorrelated. With a background of 3.0 ± 1.0 and a systematic uncertainty of 16%, we find the 95% CL upper limit $N = 4.93$ for $n_0 = 2$.

REFERENCES

[1] S. L. Glashow, Nucl. Phys. **22**, 579 (1961); S. Weinberg, Phys. Rev. Lett. **19**, 1264 (1967); A. Salam, "Proceedings of the Eighth Nobel Symposium", edited by N. Svartholm (Almqvist and Wiksells, Stockholm, Wiley, New York, 1968), page 367.

[2] A. Bean *et al.*, Phys. Rev. D**35**, 3533 (1987).

[3] W. Bartel *et al.*, Phys. Lett. B **146**, 437 (1984).

[4] H. Albrecht *et al.*, Phys. Lett. B **192**, 245 (1987).

[5] CDF Collaboration, F. Abe *et al.*, Phys. Rev. D **50**, 2966 (1994); Phys. Rev. Lett. **73**, 224 (1994).

[6] D0 Collaboration, S. Abachi *et al.*, Phys. Rev. Lett. **72**, 2138 (1994).

[7] CDF Collaboration, F. Abe *et al.*, Phys. Rev. Lett. **73**, 220 (1994).

[8] J. Ellis, S. Kelley, and D. V. Nanopoulos, Phys. Lett. B **249**, 441 (1990); U. Amaldi, W. de Boer, and H. Furstenau, *ibid.* **260**, 447 (1991); F. Anselmo, L. Cifarelli, A. Peterman, and A. Zichichi, Nuovo Cimento **104A**, 1817 (1991).

[9] P. W. Higgs, Phys. Lett. **12**, 132 (1964); Phys. Rev. Lett. **13** 508 (1964); Phys. Rev. **145**, 1156 (1966).

[10] ALEPH Collaboration, D. Decamp *et al.*, Phys. Lett. B **246**, 306 (1990); DELPHI Collaboration, P. Abreu *et al.*, Phys. Lett. B **373**, 3 (1992); L3 Collaboration, B. Adeva *et al.*, Phys. Lett. B **283**, 454 (1992); OPAL Collaboration, M. Z. Akrawy *et al.*, Phys. Lett. B **253**, 511 (1991).

[11] ALEPH Collaboration, D. Buskulic *et al.*, Phys. Rep. **216**, 253 (1992); DELPHI Collaboration, P. Abreu *et al.*, Phys. Lett. B **241**, 449 (1990); L3 Collaboration, O. Adriani *et al.*, Phys. Lett. B **294**, 457 (1992); OPAL Collaboration, M. Z. Akrawy *et al.*, Phys. Lett. B **242**, 299 (1990).

[12] CDF Collaboration, F. Abe *et al.*, Phys. Rev. Lett. **72**, 1977 (1994).

[13] V. Barger, J.L. Hewett and R.J.N. Phillips, Phys. Rev. D **41**, 3421 (1990); M. Drees, D.P. Roy, Phys. Lett. B **269**, 155 (1991).

[14] J. Gunion *et al.*, The Higgs Hunter's Guide (Addison-Wesley, New York, 1990); S.L. Glashow and E.E. Jenkins, Phys. Lett. B **196**, 233 (1987).

[15] F. Abe *et al.*, Nucl. Instrum. Methods **A271**, 387 (1988).

[16] D. Amidei *et al.*, Fermilab preprint, FERMILAB-PUB-94/024-E (1994).

[17] F. Snider *et al.*, Nucl. Instrum. Methods, **A268**, 75 (1988). This is the reference for the previous generation of the device.

[18] F. Bedeschi *et al.*, Nucl. Instrum. Methods, **A268**, 50 (1988).

[19] F. Abe *et al.*, Phys. Rev. D**43**, 2070 (1991).

[20] L. Balka *et al.*, Nucl. Instrum. Methods, **A267**, 272 (1988).

[21] S. R. Hahn *et al.*, Nucl. Instrum. Methods, **A267**, 351 (1988).

[22] S. Bertolucci *et al.*, Nucl. Instrum. Methods, **A267**, 301 (1988).

[23] F. Abe *et al.*, Phys. Rev. Lett. **62**, 613 (1989).

[24] Y. Fukui *et al.*, Nucl. Instrum. Methods, **A267**, 280 (1988).

[25] G. Brandenburg *et al.*, Nucl. Instrum. Methods, **A267**, 257 (1988);

[26] G. Ascoli *et al.*, Nucl. Instrum. Methods, **A268**, 33 (1988); G. Ascoli *et al.*, Nucl. Instrum. Methods, **A268**, 41 (1988).

[27] F. Abe *et al.*, Nucl. Instrum. Methods, **A271**, 387 (1988).

[28] F. Abe *et al.*, Phys. Rev. D**44**, 29 (1991).

[29] F. Abe *et al.*, Fermilab Preprints Fermilab-Pub-93/232-E, Fermilab-Pub-93/233-E, Fermilab-Pub-93/234-E, submitted to Phys. Rev. D.

[30] D. Amidei *et al.*, Nucl. Instrum. Methods, **A269**, 51 (1988).

[31] Sacha K. Kopp, Ph.D. Thesis, University of Chicago.

[32] G. Ascoli *et al.*, Nucl. Instrum. Methods, **A269**, 63 (1988).

[33] T. Liss *et al.*, CDF Internal Note 2367.

[34] The ISALEP version of ISAJET was first developed by UA1. Frank Paige has made the program available to CDF.

[35] F. Abe *et al.*, Phys. Rev. D **43**, 2070 (1991).

[36] F. Abe *et al.* Phy. Rev. D **49**, 1 (1994).

[37] P. Avery, K. Read, G. Trahern, Cornell Internal Note CSN-212, March 25, 1985 (unpublished).

[38] J. Ohnemus, Phys. Rev. D **44**, 1403 (1991).

[39] Particle Data Group, J. J. Hernandez *et al.*, Phys. Lett. B **239**, 1 (1990).

[40] E. Laenen, J. Smith and W.L. Van Neerven, Phys. Lett. B **321**, 254 (1994).

[41] G. Zech, Nucl. Instrum. Methods, **A277**, 608 (1989).

[42] B. Pietrzyk for the LEP Electroweak Working Group; Laboratoire de Physique des Particules preprint LAPP-EXP-94.07.